Morphology, dynamics and plasma parameters of plumes and inter-plume regions in solar coronal holes

K. Wilhelm · L. Abbo · F. Auchère · N. Barbey · L. Feng · A.H. Gabriel · S. Giordano · S. Imada · A. Llebaria · W.H. Matthaeus · G. Poletto · N.-E. Raouafi · S.T. Suess · L. Teriaca · Y.-M. Wang

Abstract Coronal plumes, which extend from solar coronal holes (CH) into the high corona and — possibly — into the solar wind (SW), can now continuously be studied with modern telescopes and spectrometers on spacecraft, in addition to investigations from the ground, in particular, during total eclipses. Despite the large amount of data available on these prominent features and related phenomena, many questions remained unanswered as to their generation and relative contributions to the high-speed streams emanating from CHs. An understanding of the processes of plume formation and evolution requires a better knowledge of the physical conditions at the base of CHs, in plumes and in the surrounding inter-plume regions. More specifically, information is needed on the magnetic field configuration, the electron densities and temperatures, effective ion temperatures, non-thermal motions, plume cross-sections relative to the size of a CH, the plasma bulk speeds, as well as any plume signatures in the SW. In spring 2007, the authors proposed a study on "Structure and dynamics of coronal plumes and inter-plume regions in solar coronal holes" to the International Space Science Institute (ISSI) in Bern to clarify some of these aspects by considering relevant observations and the extensive literature. This review summarizes the results and conclusions of the study. Stereoscopic observations allowed us to include three-dimensional reconstructions of plumes. Multi-instrument investigations carried out during several campaigns led to progress in some areas, such as plasma densities, temperatures, plume structure and the relation to other solar phenomena, but not all questions could be answered concerning the details of plume generation process(es) and interaction with the SW.

Keywords Sun · Corona · Coronal holes · Coronal plumes · Inter-plume regions · Solar wind

Abbreviations
AAS – American Astronomical Society
APL – active region plume
AOGS – Asia Oceania Geoscience
AR – active region
BP – bright point
CDS – Coronal Diagnostic Spectrometer
CH – coronal hole
CHIANTI – Atomic Database for Spectroscopic Diagnostics of Astrophysical Plasmas
DEM – differential emission measure
EKPol – Liquid crystal polarimeter
EM – emission measure
ECH – equatorial coronal hole
EIS – EUV Imaging Spectrometer
EIT – EUV Imaging Telescope
EUV – extreme UV (10 nm to 120 nm)

EUVI – Extreme UV Imager
FIP – first-ionization potential
FIT – first-ionization time
FOV – field of view
GI – grazing-incidence
IPR – inter-plume region
ISSI – International Space Science Institute
LASCO – Large Angle and Spectrometer Coronagraph
LOS – line of sight
MDI – Michelson Doppler Imager
MHD – magnetohydrodynamic
MLSO – Mauna Loa Solar Observatory
NI – normal-incidence
PL – coronal plume (in tables and diagrams)
PCH – polar coronal hole
PBS – pressure-balanced structure
PS – pseudostreamer
QS – quiet Sun
Secchi – Sun Earth Connection Coronal and Heliospheric Investigation
SOHO – Solar and Heliospheric Observatory
SW – solar wind
SWOOPS – Solar Wind Observations Over the Poles of the Sun
SWICS – Solar Wind Ionization state and Composition Spectrometer
SUMER – Solar UV Measurements of Emitted Radiation spectrometer
SP – spectro-polarimeter
SOLIS – Synoptic Optical Long-term Investigations of the Sun
SOT – Solar Optical Telescope
STEREO – Solar Terrestrial Relations Observatory
TID – time-intensity diagram
TR – transition region
TRACE – Transition Region and Coronal Explorer
UV – ultraviolet (10 nm to 380 nm)
UVCS – UV Coronagraph Spectrometer
UCS – UV Coronal Spectrometer
VUV – vacuum UV (10 nm to 200 nm)
VHM/FGM – Vector Helium and Fluxgate Magnetometers
VSM – Vector Spectro-Magnetograph
WL – white light (380 nm to 760 nm)
WLC – WL Coronagraph
XRT – X-Ray Telescope
3D (2.5D, 2D) – three-(two and a half, two)-dimensional

———————————————

K. Wilhelm (corresponding author), L. Feng*, L. Teriaca
Max-Planck-Institut für Sonnensystemforschung
37191 Katlenburg-Lindau, Germany
e-mail: wilhelm@mps.mpg.de; fax: +49 5556 979 240; tel.: +49 5556 979 423
* also at Purple Mountain Observatory, Chinese Academy of Sciences

210008 Nanjing, China, e-mail: lfeng@pmo.ac.cn

L. Abbo, S. Giordano
INAF – Osservatorio Astronomico di Torino
via Osservatorio 20, 10025 Pino Torinese, Italy

F. Auchère, N. Barbey, A.H. Gabriel
Institut d'Astrophysique Spatiale
Université Paris XI, bâtiment 121, 91405 Orsay, France

S. Imada
Institute of Space and Astronautical Science, Japan Aerospace Exploration Agency
3-1-1 Yoshinodai, Sagamihara-shi, Kanagawa, 229-8510, Japan

A. Llebaria
Observatoire Astronomique de Marseille-Provence, Laboratoire d'Astrophysique de Marseille
Pôle de l'Étoile Site de Château-Gombert
38, rue Frédéric Joliot–Curie, 13388 Marseille Cedex 13, France

W.H. Matthaeus
Bartol Research Institute and Department of Physics and Astronomy
University of Delaware, Newark, DE 19716, USA

G. Poletto
Osservatorio Astrofisico di Arcetri
Largo Enrico Fermi 5, 50125 Firenze, Italy

N.-E. Raouafi
Johns Hopkins University, Applied Physics Laboratory
11100 Johns Hopkins Road, Laurel, MD 20723-6099, USA

S.T. Suess
National Space Science and Technology Center
320 Sparkman Drive, Huntsville, AL 35805, USA

Y.-M. Wang
Code 7672, E. O. Hulburt Center for Space Research
Naval Research Laboratory
Washington, DC 20375-5352, USA

Contents

1   Introduction

Coronal plumes, extending as bright, narrow structures from the solar chromosphere into the high corona, have long been seen as fascinating phenomenon during total eclipses (cf., e.g., van de Hulst 1950a, b), and can now be observed with telescopes and spectrometers on spacecraft without interruption. They are prominent features of the solar corona, both in visible and ultraviolet (UV)[1] radiation, and are rooted in coronal holes (CH). A spectacular image of the solar corona during an eclipse is shown in Fig. 1. Notice — in the context of our study — the plumes at the N and S poles as well as the bright coronal material in the N that would interfere with any line-of-sight (LOS) observations of the plume configuration. In order to demonstrate the relation between coronal plumes and the northern and southern polar coronal holes (PCH), the occulted disk of the Sun is filled with an extreme-ultraviolet (EUV) image taken by the EUV Imaging Telescope (EIT) (cf., Sect. 2.2.2).

Van de Hulst (1950b) confirmed Alfvén's conclusion that polar coronal plumes (rays in the old terminology, cf., Sect. 7) coincided with "open" magnetic lines of force and thus outline the general magnetic field of the Sun. PCHs are best developed during the minimum of the solar activity. Consequently, many plume and PCH studies were carried out after the launch of the Solar and Heliospheric Observatory (SOHO) under very quiet conditions of the Sun in 1996 and 1997, followed by additional observations during the recent minimum of the 11 year sunspot cycle. Plumes are also observed in non-polar CHs (Del Zanna and Bromage 1999; Del Zanna et al. 2003; Wang and Muglach 2008). Most of the past observations have, however, been related to polar plumes, and they will be the main topic of this study proposed to the International Space Science Institute (ISSI), Bern, in March 2007. It was motivated by the

---

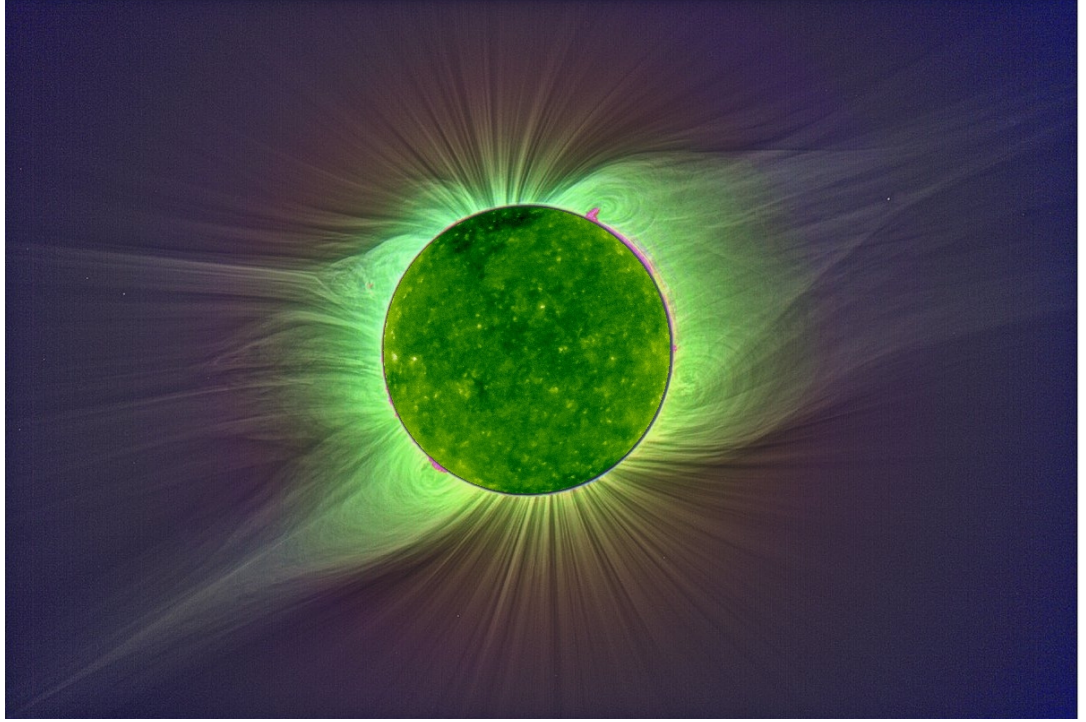[1] A list of acronyms and abbreviations is compiled in Appendix A.

Figure 1: The solar corona during the total eclipse on 1 August 2008 observed from Mongolia. The corona at solar minimum conditions has wide PCHs with reduced radiation, open magnetic field lines and many plume structures. At lower latitudes closed field-line regions dominate the corona and extend into coronal streamers (from Pasachoff et al. 2009; composite eclipse image by M. Druckmüller, P. Aniol and V. Rušin). An image in 19.5 nm of the solar disk taken from EIT/SOHO at the time of the eclipse has been inserted into the shadow of the Moon.

fact that no undisputed theoretical concept was available for the formation of plumes, and even many observational facts appeared to be in conflict with each other. In particular, the three-dimensional (3D) structure of plumes and their dynamical properties, along with those of the inter-plume regions (IPR) had been under discussion.

We, the members of the study team on "Structure and dynamics of coronal plumes and inter-plume regions" reviewed, without any claim to be exhaustive, the wealth of observational data available on coronal plumes and their environment.[2] This, together with the analyses carried out in the past, allowed us to answer a number of questions formulated in the proposal phase of the study. These questions will be repeated in the appropriate sections, and we will restrict the discussion to these specific topics as a general review on coronal plumes taking all aspects into account will appear in Living Reviews (Poletto, to be submitted). We can also refer the reader to earlier plume studies, e.g., by Saito (1965a), Newkirk and Harvey (1968), Ahmad

---

[2]Taking advantage of the prevailing solar minimum conditions at the beginning of the proposed study, some additional plume observations had also been suggested and were carried out in 2007 and 2008. The analysis of these data sets is not yet completed, but some campaign information and results are included in this report.

and Withbroe (1977), Del Zanna et al. (1997), DeForest et al. (1997) and Koutschmy and Bocchialini (1998). Reference can also be made to reviews on the extended corona of the Sun (Kohl et al. 2006) and to solar UV spectroscopy (Wilhelm et al. 2004, 2007). The interest in coronal plumes led to two special sessions in the past, namely, "Solar jets and coronal plumes", Guadeloupe, 23 – 26 February 1998 (ESA SP-421, 1998, T-D Guyenne, ed.) and "Solar polar plumes" at the 2nd Asia Oceania Geoscience (AOGS) Conference, Singapore, 20 – 24 June 2005.

It might be appropriate to mention from the outset that not all questions could be answered conclusively. Future investigations utilizing multi-instrument, high-resolution observations will be needed to complete the task.

2   Instrumentation

The study of coronal plumes and IPRs in CHs of the Sun requires many observational facts obtained with the help of ground-based and space instruments. It is beyond the scope of this review to provide detailed descriptions of these devices, but short characterizations of some of the instruments mentioned and the cooperation in observational campaigns might be useful for appreciating the corresponding investigations.

2.1   Ground-based systems

The main advantage of ground-based observations is related to the large telescope apertures available permitting high spatial and temporal resolutions, including polarization measurements. However, detailed plume investigations can only be conducted in the optical window of the terrestrial atmosphere and, in general, during total solar eclipse periods with temporary campaign installations.[3] Exceptions are, for instance, the white-light (WL) plume observations with the Mk III K-coronameter of the Mauna Loa Solar Observatory (MLSO) (DeForest et al. 2001a), and the determination of plume lifetimes between 10 h and 20 h with the help of the Fe X 637.4 nm ($T_F = 0.98$ MK) line[4] during the solar minimum 1954 (Waldmeier 1955).

The Synoptic Optical Long-term Investigations of the Sun (SOLIS) project (Keller et al. 2003) employs a 50 cm aperture Ritchey–Chrétien telescope and a vector spectro-magnetograph (VSM) for investigations of solar magnetic fields. It is designed to help understand the origin of the solar cycle (complementing helioseismic studies) through the study of different aspects of the Sun's magnetic activity related to the cycle at different scales (dynamo, turbulent magnetic fields, irradiance changes, differential rotation). One of the main goals is to develop methods and techniques for solar activity forecast (e.g., flares, coronal mass ejections). VSM provides vector magnetic fields and the LOS field using spectral lines characterized by their Zeeman-induced polarization, in addition to a chromospheric line that serves as a proxy for coronal structures ensuring observational continuity at different heights in the solar atmosphere. The LOS magnetograms obtained from chromospheric lines benefit from the canopy

---

[3]The chances that the totality path of an eclipse crosses a site of a very large permanent telescope are low, however on 11 July 1991 an eclipse could be observed with the 3.6 m Canada-France-Hawai Telescope on Mauna Kea (see, e.g., November and Koutchmy 1996).

[4]The formation temperatures, T_F, of ionic emission lines (cf., Sect. 5.2.1) are given in parentheses.

structure of the field yielding strong signals everywhere on the solar disk, in particular close to the limb.

2.2 Space systems

The restrictions on mass and size in the case of space instrumentation are to a large extent compensated by the wide energy ranges accessible both for photons and charged particles combined with the flexibility in selecting the spacecraft position during the observations.

2.2.1 Ulysses

Launched in October 1990, Ulysses travelled outwards to Jupiter, where it used a gravitational assist to turn the orbit away from the ecliptic plane. The final orbit has an 80.4° inclination, 1.34 ua perihelion, 5.4 ua aphelion, and a period of 6.2 years. Three polar passes were completed, two of them near sunspot minimum, before the mission was terminated in June 2009. The spacecraft carried a complete compliment of fields and particles instruments. For plume studies, the relevant instruments are the Solar Wind Observations Over the Poles of the Sun (SWOOPS) (Bame et al. 1992), a thermal ion and electron spectrometer with energy ranges for electrons from 0.81 eV to 862 keV and ions from 255 eV/Z to 34.4 keV/Z, the Solar Wind Ionization state and Composition Spectrometer (SWICS) (Gloeckler et al. 1992), and the Vector Helium and Fluxgate Magnetometers (VHM/FGM) (Balogh et al. 1992).

SWOOPS returned the temperatures, densities and vector speeds of protons (H$^+$, p), α particles (He^{2+}) and electrons. Speed changes of a few kilometres per second over a few seconds could be resolved. SWICS recorded the speed and density of He^{2+} and the densities, ionization states and speeds of several minor ions of the elements C, O, Ne, Mg, Si and Fe. The data rate of Ulysses was limited by the transmitter power available and the distance from the Earth so that expected SWICS plume signatures are at the level of detectability. VH-FGM measured the vector magnetic field at a far higher cadence than SWOOPS.

2.2.2 Remote-sensing instrumentation

Some of the relevant instrument characteristics are listed in Table 1 in order to present a compact and coherent overview of the following missions and their operational periods:
– Spartan was a satellite system launched and retrieved by the Space Shuttle on four occasions. It carried the Ultraviolet Coronal Spectrometer (UCS), an externally and internally occulted coronagraph with a dual spectrograph as well as the White Light Coronagraph (WLC) (Kohl et al. 1995; Guhathakurta and Fisher 1995), a coronagraph with polarimeter for polarized brightness, pB, measurements (cf., Sect. 5.1).
– SOHO was launched on 2 December 1995 and injected into a halo orbit around the Sun-Earth Lagrange point L1 (≈ 0.01 ua sunward of the Earth) on 14 February 1996 (see Domingo et al. 1995 and references therein). The following instruments are of importance in our context: (1) The Coronal Diagnostic Spectrometer (CDS) with normal- and grazing-incidence (NI/GI) spectrometers in the EUV wavelength range. (2) EIT, a full-disk solar imager for observations in the emission lines Fe IX 17.1 nm (0.71 MK), (Fe X 17.5 nm); Fe XII 19.5 nm (1.38 MK); Fe XV 28.4 nm (2.08 MK); He II 30.4 nm (81 000 K). (3) The Large Angle and

Table 1: Some characteristics of space-borne remote sensing instrumentation

Mission (Time) Instrument	Wavelength ranges[a], λ/nm	Resolutions: spectral, $\lambda/\Delta\lambda$	angular	FOV
Spartan 201 (1993 to 1998)				
UCL	103.2, 103.8, 121.6, 124.2	≈ 5000	$\geq 30'' \times 150''$	$4' \times 5'$ corona
WLC	480, pB	≈ 10	$22.5''$	1.25 $R_\odot$ to 6 $R_\odot$
SOHO (1995 to —)				
CDS (NI, GI)	$15\ldots80$	1000 to 10 000	$\approx 3''$ ($2''$ slit width)	Slit, disk, low corona
EIT	17.1, 19.5, 28.4, 30.4	Filter bands: $12\ldots20$	$2.6'' \times 2.6''$ pixel	$45' \times 45'$
LASCO (C1, C2, C3)	WL, 530.3	C1: ≈ 8000 Filter bands	$5.6''$, $11.4''$, $56''$ pixels	1.1 $R_\odot$ to 30 $R_\odot$
MDI	WL, 676.78	70 000	$2''$ pixel $0.6''$ pixel	$34' \times 34'$ $11' \times 11'$
SUMER	$78\ldots161$, WL ($46.5\ldots80.5$)	20 000 (40 000)	$0.3''$, $1''$, $4''$ slit widths	Slits, disk, low corona
UVCS	$103.2\ldots124.2$, WL ($49.9\ldots62.5$)	5000 (7000)	$7''$ pixel	$40' \times 141'$ corona
TRACE (1998 to 2010)	WL, 17.1, 19.5, 28.4, 121.6, 155, 160, 170	Filter bands	$0.5''$ pixel	$8.5' \times 8.5'$ disk, low corona
Hinode (2006 to —)				
SOT	$380\ldots657$ $380\ldots657$	Narrow bands Broad bands	$0.08''$ pixel $0.053''$ pixel	$328'' \times 164''$ $218'' \times 109''$
SP	$630.08\ldots630.32$	30 000	$0.16''$ pixel	$320'' \times 151''$
EIS	$17\ldots21$ $25\ldots29$	$\approx 10\,000$ $\approx 14\,000$	$1''$ pixel	$590'' \times 512''$ disk, low corona
XRT	$0.2\ldots20$, 430.5	Filter bands	$1''$ pixel	$2048'' \times 2048''$
STEREO (2006 to —)				
EUVI	17.1, 19.5, 28.4, 30.4	Filter bands: 12, 12, 14, 10	$1.59''$ pixel	$0\ldots1.7\ R_\odot$

[a] ranges in the second-order of diffraction in parentheses

Spectrometer Coronagraph (LASCO), a triple coronagraph (C1, C2, C3) in the visible wavelength regime with nested FOVs out to heliocentric distances $R = 30\ R_\odot$ (1 $R_\odot$ = 696 Mm, the radius of the Sun[5]). C1 observed with a Fabry–Perot interferometer, among other lines, Fe XIV 530.3 nm (1.82 MK). C2 and C3 had a set of wideband filters. Most of images were obtained with the orange filter of C2: (540 to 640) nm, and the clear filter of C3: (400 to 850) nm; both used a set of three polarizers (–60°, 0°, 60°) on specific sequences. (4) The Michelson Doppler Imager (MDI) observes solar oscillations and LOS magnetic fields in the Ni I 678.8 nm line with a tunable interferometer. (5) The Solar Ultraviolet Measurements of Emitted Radiation spectrometer (SUMER) measures radiation in the vacuum-ultraviolet (VUV) wavelength range with slit lengths of $120''$ and $300''$ and spatial rasters. (6) The

[5]1 $R_\odot$ is seen from Earth under an angle of $961'' \pm 15''$, depending on the season. The angle is $\approx 10''$ larger from SOHO. A distance of ≈ 720 km in the solar photosphere corresponds to $1''$.
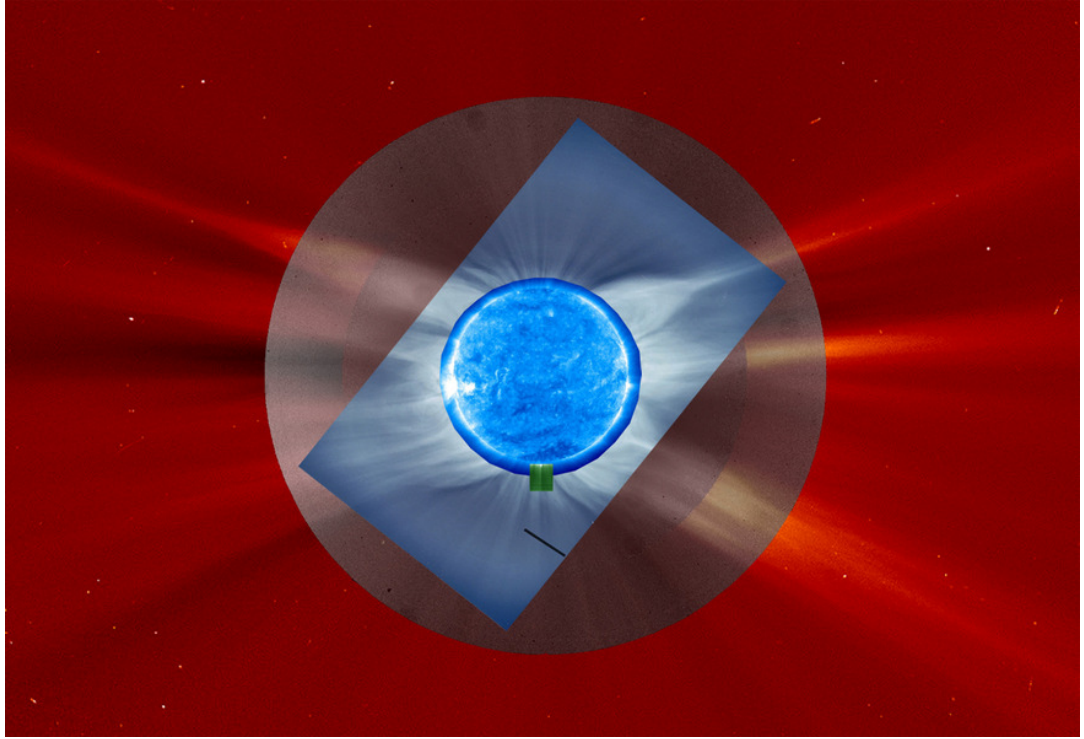
Figure 2: Composite image of the corona during the eclipse of 29 March 2006 built up from SOHO data (outer frame from LASCO, green rectangle near south pole from SUMER), polarized radiation from the EKPol experiment (circular portion from Abbo et al. 2008) and WL ground-based observations (rectangular portion from Koutchmy et al. 2006; obs.: J. Mouette). The solar disk in the 17.1 nm band of EIT has been inserted into the shadow of the Moon. The black solid line represents the operational UVCS slit during the eclipse.

Ultraviolet Coronagraph Spectrometer (UVCS) spectrometers are fed by three occulted telescopes for observations of the extended solar corona.
– The Transition Region and Coronal Explorer (TRACE), was launched by a Pegasus vehicle into a Sun-synchronous Earth orbit on 2 April 1998. The spacecraft carried a 30 cm Cassegrain telescope. A typical temporal resolution was 5 s (Handy et al. 1999).
– Hinode was launched on 22 September 2006 (Kosugi et al. 2007). The three instruments on board are: (1) The Solar Optical Telescope (SOT), a 50 cm diffraction-limited Gregorian telescope (Suematsu et al. 2008) feeding narrow-band and broad-band filter imagers and a spectro-polarimeter (SP). Polarization spectra of the Fe I 630.15 nm and 630.20 nm lines are obtained for high-precision Stokes polarimetry and measurements of the three components of the magnetic field in the photosphere (Tsuneta et al. 2008a). (2) The EUV Imaging Spectrometer (EIS), a NI stigmatic spectrometer fed by a multi-layer telescope (Culhane et al. 2007), observes prominent emission lines, e.g., Fe VIII 18.52 nm (0.44 MK), Fe XII, Fe XIII 20.2 nm (1.58 MK) and Fe XXIV 19.20 nm (17.0 MK), with four slit or slot widths from $1''$ to $266''$. (3) The X-Ray Telescope (XRT), a 30 cm aperture GI telescope with analysis filters, provides nine X-ray wavelength bands with different lower cut-off energies (Golup et

al. 2007).

– The Solar Terrestrial Relations Observatory (STEREO), was launched in October 2006 near a minimum of solar activity. Two identical spacecraft (STEREO A and B) are drifting apart along the Earth's orbit and observe the Sun almost simultaneously with the Extreme Ultraviolet Imager (EUVI) telescopes (Wuelser et al. 2004) of the instrument package Sun Earth Connection Coronal and Heliospheric Investigation (Secchi) (Howard et al. 2008). For plume observations, long exposure times and low compression rates are applied to increase the signal-to-noise ratio.

2.3 Eclipse and other campaigns

In particular during total eclipse periods, but also at other times, special plume observing campaigns have been organized involving many instruments on the ground and in space. Examples are:

2.3.1 Eclipse campaign 2006

Total solar eclipses offer great opportunities to observe the faint solar corona, especially in its inner portions, which are not easily accessible by coronagraphic telescopes, owing to the instrumentally scattered light. This background is significantly reduced during an eclipse.

During the total eclipse of 29 March 2006, the greatest eclipse point was at Waw an Namous, Lybia, in the Sahara Desert at 10:11:18 UTC with a duration of 4 min 7 s. An Italian scientific expedition was organized to reach this site and measure the linearly polarized radiation of the corona, with the help of the EKPol experiment, a liquid crystal K-corona imaging polarimeter (Zangrilli et al. 2006). These and other ground-based observations during the eclipse were coordinated with those of the space instruments EIT, CDS, LASCO, SUMER and UVCS. The composite image in Fig. 2 shows some of the data obtained and the position of the operational UVCS slit during the eclipse. The polar angle of the slit centre was 147° at a heliocentric distance of 1.63 $R_\odot$. UVCS observed plume and IPR structures during the time interval from 06:16 to 18:40 UTC in the O VI 103.2 nm, 103.8 nm doublet (0.3 MK), and — immediately before the eclipse — in the H I 121.6 nm Ly α line.

2.3.2 Multi-instrument campaign 2008

Based on the experience gained during further cooperative efforts in 2007, the southern PCH was the target of a multi-instrument campaign from 22 June to 3 July 2008. The purpose of the observations was to get morphological information on plumes as well as on the physical parameters of the plume and IPR plasmas. We summarize the campaign characteristics here and present preliminary results from XRT in Sects. 5.2.1 and 6.3. SUMER recorded spectra over 8 h time intervals covering the TRACE and Hinode observing times on a daily basis (with a gap on 26 June). Included in the spectra are the H I Ly α and 102.6 nm Ly β lines, as well as lines from O VI 103.2 nm, 103.8 nm, N V 123.9 nm (0.18 MK), Si VIII (144.0, 144.6) nm (0.81 MK), Ne VIII 77.0 nm (0.62 MK), Mg IX (70.6, 75.0) nm (0.95 MK), Mg X 62.5 nm (1.12 MK) and Fe XII. UVCS took data from $R = 1.8$ $R_\odot$ to 3 $R_\odot$. Ly α radiances and spectral profiles have been obtained. TRACE images in the 17.1 nm and 160 nm channels

have been acquired daily, at times when Hinode was taking data and also at extra times, including a 20 h continuous observation run on 1 July. Hinode data are available with gaps on 23, 27, 30 June and 3 July. A typical observing sequence lasted 2 h to 4 h. XRT images have been acquired with three filters (namely, Al_poly, Al_mesh and C_poly) in a FOV of $526.6'' \times 526.6''$ and a cadence of 35 s. EIS performed calibration-related studies over most of this campaign, but, in addition, observed the He II 25.6 nm (87 000 K), Mg VI 27.0 nm (0.44 MK), Mg VII 27.7 nm (0.63 MK), Si VII 27.5 nm (0.59 MK) lines, and emissions from a number of Fe ions with ionization stages from 10+ to 16+.

3   Morphology of plumes in coronal holes

Coronal plumes are obviously 3D structures in solar CHs, and the following questions have to be answered: – Can the fore- and background problems caused by closed magnetic field regions around CHs be solved? – Can *standard* magnetic field configurations for CHs, plumes and IPRs be determined? – Does the plume assembly expand super-radially? – What is the cross-section of plumes, and, in general, their 3D structure? – Do SOHO and STEREO instruments observe single plumes or bright features as combinations of structures along the LOS ? – What are the prospects of tomographic methods, and how could they evolve in the STEREO era? – What is the ratio of the total plume area to the IPR in CHs at the base of the corona? – Is the apparent plume width of ≈ 30 Mm in the low corona an agreed value? – Can plumes be describe as fractal structures? – How can the rotation speed of coronal plumes be evaluated?

3.1   Magnetic field configuration

Coronal plumes are rooted in solar CHs, and consequently the magnetic field configuration of CHs is of major importance. CHs have first been identified as dark regions of the corona by Waldmeier (1951, 1957) and later as sources of the fast solar wind (SW) streams by Krieger et al. (1973). CHs are characterized by open magnetic field lines of the majority magnetic flux (cf., Bohlin 1977; Bohlin and Sheeley 1978) interacting with chromospheric network loops (cf., Wang and Sheeley 1995; Wang et al. 1997). The loop heights in CHs are, in general, smaller than in quiet-Sun (QS) regions (Wilhelm 2000; Tian et al. 2008)—about half as high as in QS regions (Wiegelmann and Solanki 2004). Despite this different magnetic loop configuration, CHs and QS regions are difficult to distinguish in most of the chromospheric and transition-region (TR) lines (Huber et al. 1974).

The difficulty in measuring magnetic fields in polar regions with ground-based instruments stems from the noise in the magnetograms caused by a strong radiance gradient and the foreshortening effect near the solar limb. Moreover, most of the observations in polar regions yield the LOS component of the magnetic field. Full Stokes polarimetry without seeing concerns can now be carried out with SOT. Tsuneta et al. (2008b) studied the magnetic landscape of the S polar region of the Sun shown in Fig. 3. Many patchy magnetic flux concentrations with field strengths of more than 0.1 T (1 kG) were found at heliographic latitudes between $-70°$ and $-90°$. The correction of the foreshortening effect can be noticed on the left-hand side of the figure. In general, the strong vertical magnetic fields have the same polarity, consistent with the global polarity of the polar region. A comparative study of
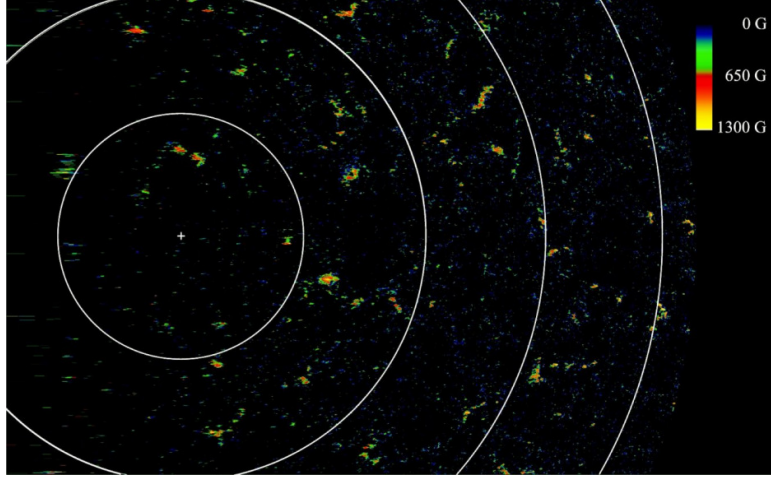
Figure 3: S polar view of the magnetic field observed between 12:02:19 and 14:55:48 UTC on 16 March 2007. Heliospheric latitudes are shown for $-85°$, $-80°$, $-75°$ and $-70°$. The FOV is about $327''$ (E–W; shown in the vertical direction) by $473''$ (N–S along the LOS). (from Tsuneta et al. 2008b, reproduced by permission of the American Astronomical Society, AAS).
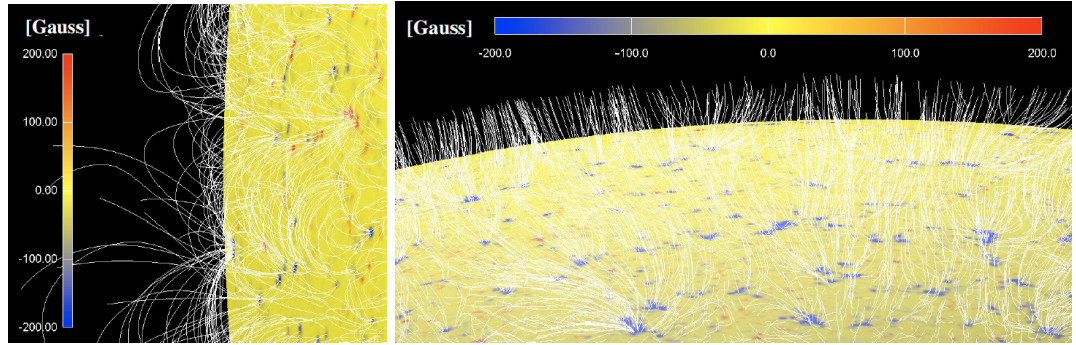

Figure 4: Magnetic field structures extrapolated from SOT/SP observations in 2007. A fraction of a PCH (280 Mm × 140 Mm) on 16 March is shown in the right panel with many open field lines extrapolated to a height of ≈ 20 Mm. The left side depicts an equatorial region (160 Mm × 140 Mm) with many closed field lines extrapolated to a height of ≈ 70 Mm on 28 November (from Ito et al. 2010, reproduced by permission of the AAS).

the magnetic-field structures in CHs and equatorial QS regions by Ito et al. (2010) confirmed that the positive and negative vertical magnetic fluxes in equatorial regions are balanced, whereas the field is dominated by a single polarity in CHs. Potential field extrapolations in Fig. 4 show in an impressive way that most of the field lines in QS regions are closed and the majority of the magnetic field lines from the flux concentrations in CHs are open fanning out with height. Such funnel-type geometries extending from strong unipolar flux concentrations have been derived in many studies using magnetic-field extrapolations from photospheric observations into the corona (cf., Gabriel 1976; Dowdy et al. 1986; Suess 1998; Tu et al. 2005; Wiegelmann et al. 2005). Although these funnels are mainly considered as source regions of the fast SW, they can also describe coronal plumes. In fact, one funnel analysed by Tu et al. at $x = 50''$ and $y = 175''$ does not show any outflow speed (cf., Sect. 4.3). This feature had earlier been identified as a plume (Wilhelm et al. 2000). We will expand the discussion on the presence of outflows in plumes and IPRs in Sect. 4.3.

"Rosettes" in the magnetic field structure related to flux concentrations have been described by Beckers (1963). A connection between plumes and rosettes was suggested by Newkirk and Harvey (1968), who estimated that ≈ 10 plumes would be present at each polar cap at a time — only about 1/30 of the number of rosettes. The filling factor of plumes in CHs is ≈ 0.1 according to Ahmad and Withbroe (1977), however, even smaller factors must be expected from results discussed in the next section. Axford and McKenzie (1992, 1996) argued that small-scale reconnection events — so-called microflares; in analogy to the nanoflare concept (Parker 1988) — in the chromospheric network (with field strengths of 20 mT and more) would produce waves, shocks, energetic particles and hot plasma jets that should suffice to create the fast SW on open field-line structures (McKenzie et al. 1995).

From WL observations, plumes appear to expand super-radially together with the CHs with altitude (Saito 1965a; Ahmad and Withbroe 1977; Munro and Jackson 1977; Fisher and Guhathakurta 1995; Koutchmy and Bocchialini 1998). DeForest et al. (1997) found from SOHO observations that plumes rapidly expand (super-radially with a half-cone angle of 45°) in their lowest height range $h = R - 1 \, R_\odot < 30$ Mm to diameters of 20 Mm to 30 Mm, and more slowly above; the linear expansion ratios of plumes seen in the plane of the sky were 1, 3 and 6 at heights of $h = (0.05, 4, 14) \, R_\odot$, respectively, and 1, 3 and 3 for the background CH. The expansion factor of a plume is also a weak function of the footpoint location in the CH (cf., Goldstein et al. 1996; DeForest et al. 2001b). The CH expansion factor, $f(R)$, for a flux tube with cross-section A is often defined (cf., e.g., Kopp and Holzer 1976) as $A(R)/A(R_\odot) = (R/R_\odot)^2 \, f(R)$, where $f(R_\odot) = 1$ and $f(R)$ depends upon the parameters f_{max}, R_1 as well as σ (f_{max} is the net non-radial divergence, R_1 the distance of the most rapid expansion and σ the range over which it occurs). In this framework, the CH expansion published by Cranmer et al. (1999) can be parametrized by the values 6.5, 1.5 $R_\odot$ and 0.6 $R_\odot$ of the above parameters, whereas the expansion of DeForest et al. (2001b) can be fitted reasonably well by the values 5.65, 1.53 $R_\odot$ and 0.65 $R_\odot$ — after noticing that the quantity $\sqrt{f(R)}$ is shown in their Fig. 8. The conclusion was reached that a radial expansion claimed by some authors (cf., e.g., Woo and Habbal 2000) is inconsistent with observations in PCHs. The plumes subtend a solar latitude angle of 2° to 2.5° near the limb, which is in agreement with eclipse observations (Newkirk and Harvey 1968). Observations during four eclipse periods showed an average width of 31 Mm (corresponding to 2.6°) at $h = 0.05 \, R_\odot$ (Hiei et al. 2000). The fraction of plumes wider than 4° or narrower than 2° was ≈ 20 %, each.

As mentioned in Sect. 1, the best observing conditions of coronal plumes exist near the minimum of the activity cycle when the PCHs have their maximum extension from the poles to $\pm 60°$ solar latitudes (Wang and Sheeley 1990; Banaszkiewicz et al. 1998). In this phase, it is unlikely that neighbouring streamers significantly contaminate the PCH observations.[6] The southern CH in Fig. 1 shows an example of such an optimal condition. It is obvious from this figure that the plumes diverge super-radially with altitude in the PCHs. Plumes near the limb appear to converge to points on the solar rotation axis more than half the way between the centre of the Sun and the poles (Saito 1965a; Marsch et al. 1997; Boursier and Llebaria 2008). The super-radial expansion could also be confirmed in the 3D reconstructions using EUVI data in 2007 (Feng et al. 2009). An example of such a reconstruction is shown in Fig. 5. In addition to the divergence of the plume assembly, the cross-sectional area of

---

[6]The LOS geometry from the Earth will also be influenced by the tilt angle of the solar rotation axes of 7.25° with respect to the ecliptic plane.
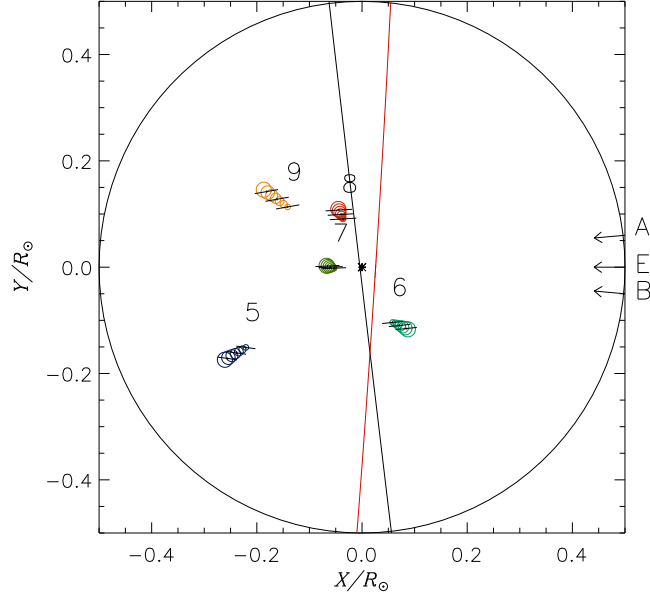
Figure 5: Projections onto the solar equatorial plane of reconstructed plumes observed in the northern CH on 1 June 2007 by EUVI. The LOS directions from the Earth (E) and STEREO A and B are marked together with the corresponding limb projections from A (black) and B (red) (after Feng et al. 2009). The numbers 5 to 9 refer to the plumes identified in Fig. 7.

the plumes expands as well (cf., Casalbuoni et al. 1999; and the discussion in the previous paragraph). According to model calculations, most of this expansion occurs at the base below ≈ 35 Mm, where the plumes grow in diameter from ≈ 3 Mm by nearly a factor of ten. In the regime of low β (the ratio of the plasma pressure to the magnetic pressure) up to at least $5\ R_\odot$, the geometric spreading factors in plumes and IPRs vary together (Suess et al. 1998; Suess 2000).

In the photosphere, the footpoints of plumes — more specific *beam plumes* as defined in the next section — lie near unipolar flux concentrations, and in the corona the plumes follow, as mentioned before, magnetic field lines, although Lamy et al. (1997) and Zhukov et al. (2001) detected twisted and helicoidal shapes in LASCO-C2 images, and a "doublet" fine structure was seen in eclipse images (cf., Koutchmy and Bocchialini 1998). Observations with many SOHO instruments and MLSO Mk III allowed DeForest et al. (1997, 2001a) to trace plumes to $R = 15\ R_\odot$, where the brightness observed by LASCO-C3 decreased significantly, although the brightest structures could be identified out to 30 $R_\odot$.

The boundaries of CHs rotate more rigidly than the underlying photospheric plasma (Timothy et al. 1975; Wang et al. 1996), and hence apparently do the ensemble of plumes within the CH boundaries (Llebaria et al. 1998). This does not necessarily imply that individual plumes rotate rigidly, only that closed loops must be continually converted into open field lines and vice versa at the CH boundaries, presumably via interchange reconnection (Crooker et al. 2002; Wang and Sheeley 2004). For the boot-shaped CH in August 1996, Zhao et al. (1999) give a nearly rigid rotation rate of 13.25º/d. Smaller CHs during more active periods of the Sun do, however, show differential rotation (cf., Wang et al. 1996; Wang 2009). In these CHs at lower solar latitudes, coronal plumes have also been observed with properties similar to those in polar regions (Wang and Muglach 2008).

14

The distribution of magnetic flux concentrations in CH has been studied with chromospheric magnetograms from SOLIS/VSM (Raouafi et al. 2007a). The monthly averaged distribution of polar flux elements as a function of latitude (normalized to the surface area) The distribution is relatively flat up to ≈ 75° and drops to higher latitudes. The CH boundary varied between ≈ 60° and 70° with time and longitude. Larger flux elements fall off more sharply than smaller ones. If they would be required for the generation of prominent plumes, this result is consistent with the forward modeling by Raouafi et al. (2007b) demonstrating that plumes near the poles do not yield the O VI profiles observed by UVCS (cf., Sect. 4.3), and also with Saito's (1965a) observations that plumes are rooted preferably in a ring at latitudes between 70° and 80°.

3.2 Plume geometry and dimensions

Some aspects of the plume dimensions have already been mentioned in relation to the magnetic field configuration in the previous section. It is not directly possible to determine the 3D geometry of the plume structures from 2D observations integrated along the LOS, and thus not all plumes might be of cylindrical shape with diameters of ≈ 30 Mm in the low corona. It has been suggested by Gabriel et al. (2003) that "curtain" plumes would only become visible when the curtain will be aligned with the LOS. These features would be a second type of plumes as there can be no doubt that near-cylindrical plumes do exist, for instance, those related to bright points (BPs) (cf. Sect. 6.2). The main argument for non-cylindrical plume structures stems from EIT images in the 17.1 nm band, such as those in Fig. 6, giving the impression that most of the plumes in the CH are located on the far side of the Sun. The same effect is evident in EUVI images as can be seen from Fig. 7. Since there is no reason for such an asymmetry, the increase of the LOS length through a curtain plume above the limb was thought to create the effect. A separation into two types of plumes could also be made by considering the relative brightness profiles of individual plumes versus heliocentric distance. Similar curtain- or sheet-like plumes had been identified by Wang and Sheeley (1995) extending over several network cells.

Electron density measurements, discussed in detail in Sect. 5.1, provide strong evidence that the CH plasma consists of two distinct density regimes. If identified with plume and IPR plasmas, the plumes occupy a maximum of ≈ 10 % of the length of the LOS through the CH (Wilhelm 2006). These findings are inconsistent with a conterminous curtain plume, but might be compatible with microplumes aligned in a certain fashion. Such a scenario has been proposed by Gabriel et al. (2009). Simulations produce realistic images of plume assemblies under the assumption that the footpoints of microplumes are aligned along lanes of the chromospheric network. This population of plumes is therefore called "network plumes" in contrast to "beam plumes" that are, in general, related to BPs at some stage of their life (cf., Sect. 4.1). However, it is quite possible that beam plumes are also composed of microplumes in a more compact arrangement. Such an option might shed some light on the findings of Newkirk and Harvey (1968) that a *typical* plume with cylindrical symmetry has a core (electron) density of ≈ $10^8 \, \mathrm{cm}^{-3}$ and a radial density profile dependent on the distance from the plume axis. The apparent density profile could, however, also be attributed to a varying LOS length through the plume cross-section with more or less constant density. Loops and plumes composed of multiple strands below the resolution of present-day coronal imagers are considered by DeForest (2007).
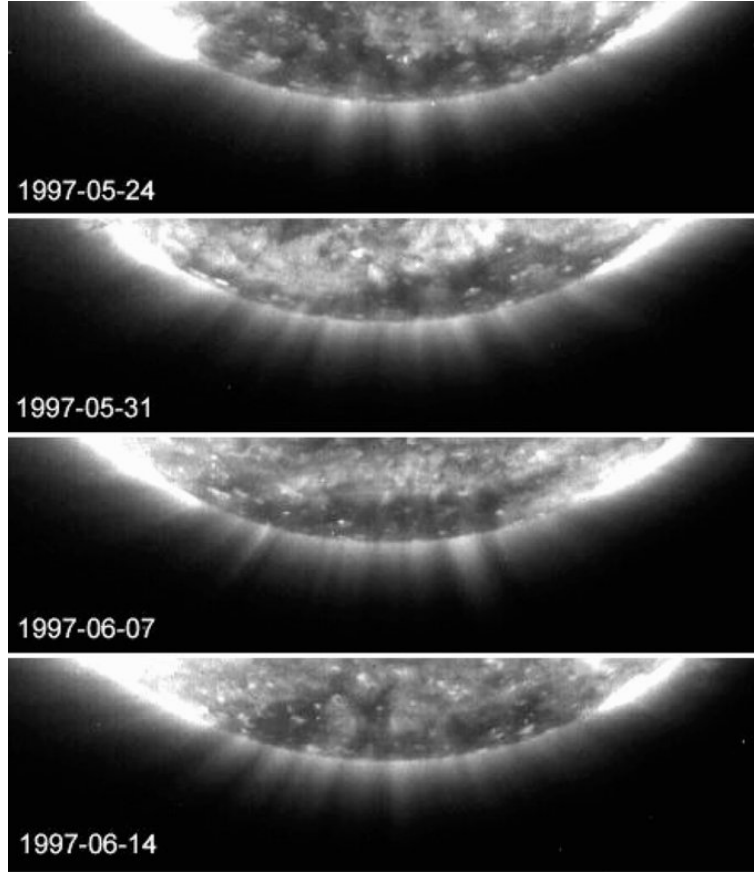
Figure 6: Four EIT images of the southern PCH in the 17.1 nm wavelength band, recorded at 7 d intervals corresponding to about a quarter solar rotation (from Gabriel et al. 2009).

One method of disentangling the LOS integration in the optically thin coronal plasma is rotational tomography (Frazin 2000) using image sequences taken by LASCO and EIT. In traditional rotational tomography, two major assumptions are made. First it is assumed that the solar rotation rate is the same at all latitudes and altitudes. Second, it is assumed that the coronal structures are stable over the acquisition time, i.e., about two weeks. Both assumptions induce artifacts in the reconstructed emissions, and modern tomographic inversion codes aim at avoiding these problems. Barbey et al. (2008) have addressed the effect of temporal variation in the case of polar plumes. They have proposed a reformulation of the inversion problem in order to obtain both the 3D structure of plumes and their temporal evolution. Results by DeForest et al. (2001b) suggest that even though plumes seem to be short-lived, their magnetic skeleton may be stable, at least in some cases, for several days. Based on this observation, the code developed by Barbey et al. (2008) assumes that temporal evolution occurs only in a limited number of volume regions. In the reconstructed volumes, one can identify both tube-like structures similar to the intuitive idea of plumes, but also more elongated features and a structuration in cells.

WL plumes could continuously be observed with LASCO-C2 in the polar areas during the periods of low solar activity (for instance in the years 1996 to 1998 and 2007 to 2010). Examples are shown in Fig. 8. Note that in the FOV of LASCO-C2 the plumes diverge more or
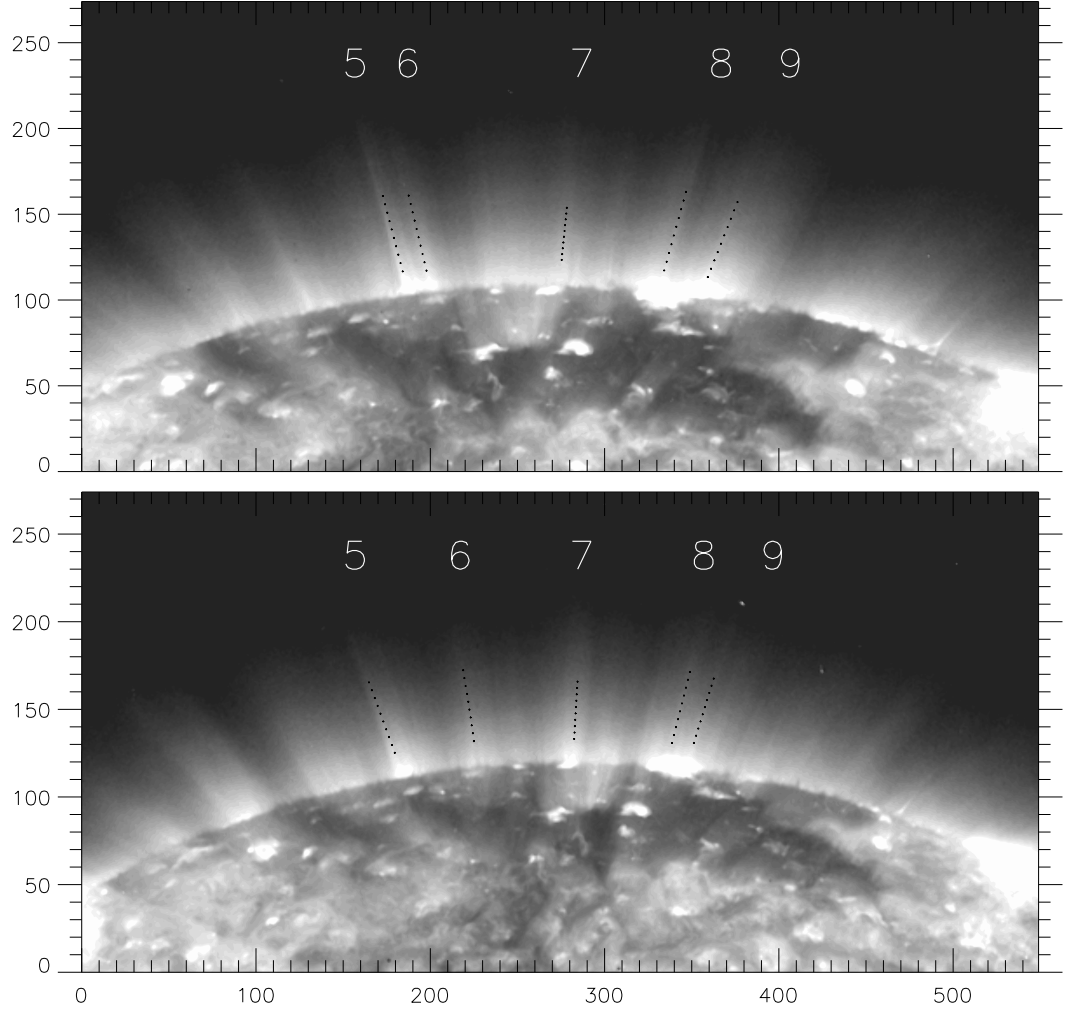
Figure 7: EUVI images in the 17.1 nm band of the northern CH on 1 June 2007 seen from STEREO A (top panel) and B (bottom panel). Strong (beam) plumes are marked by dark dotted lines (after Feng et al. 2009). The LOS geometries and the reconstructions of the plumes labelled 5 to 9 are shown in Fig. 2. The scales of the axes are in pixels with a size of $1.59''$.

less radially from a point on the polar axis not very far from the pole (Llebaria et al. 2001), whereas closer to the Sun the plume geometry looks totally different (cf., Fig. 1). Due to the intrinsic differences between VUV and WL photo-emission mechanisms (cf., Sect. 5.2.1) as well as temporal variations, it is difficult to demonstrate the continuity of plumes in the different wavelength regimes. The correlation between both types of plumes was studied by comparing EUV and WL sinograms derived from a large set of EIT, LASCO-C1 and C2 images (DeForest et al. 2001b). Sinograms are 2D images which display the evolution with time of an evolving profile (frequently resulting from a projection). The correlation between sinograms obtained in different wavelengths and radial distances required an angular correc-

tion to compensate for the super-radial expansion. The resulting correlation coefficient was significant and established a direct link between EUV and WL plumes. This demonstration based on the co-evolution of both features is more robust than image-to-image comparisons of local details. The CH expansion factor deduced is 2.25 at $R = 3\ R_\odot$ in good agreement with other determinations (DeForest et al. 1997; Cranmer et al. 1999).

With LASCO-C2 it was possible to restitute simultaneously images of the polarized K-corona and the unpolarized F-corona from polarization measurements (Llebaria et al. 2010). In circular profiles of the K-corona centred on the divergence point, plumes and IPRs appear as random oscillations with a relative amplitude of ≈ 1 %. From a spectral analysis of such oscillations, Llebaria et al. (2002a) concluded that the angular size distribution is fractal, and thus the concept of a characteristic angular size is inapplicable to images of WL plumes. A superposition of multiple strands of different sizes leads to a smooth variation undulating the background. The low level of high-frequency oscillations relative to the background is indicative of a large number of tiny plumes along the LOS. Support for this concept has been obtained by a forward modeling approach (Boursier and Llebaria 2005; cf., Sect. 8.3). Since the observed plumes are projections of 3D structures, the fractal 2D structure provides a strong clue for assuming a fractal structure also for the physical plumes, i.e., the 3D electron density distribution over the CH domain is probably fractal. Its dimension must be $D = 2.9$ over the CH, in order to obtain a fractal dimension of $D = 1.5$ in the transverse profile of WL plumes. The high fractal dimension required by the density distribution of plumes looks surprising, but is understandable because of the strong integration effect along the LOS. The
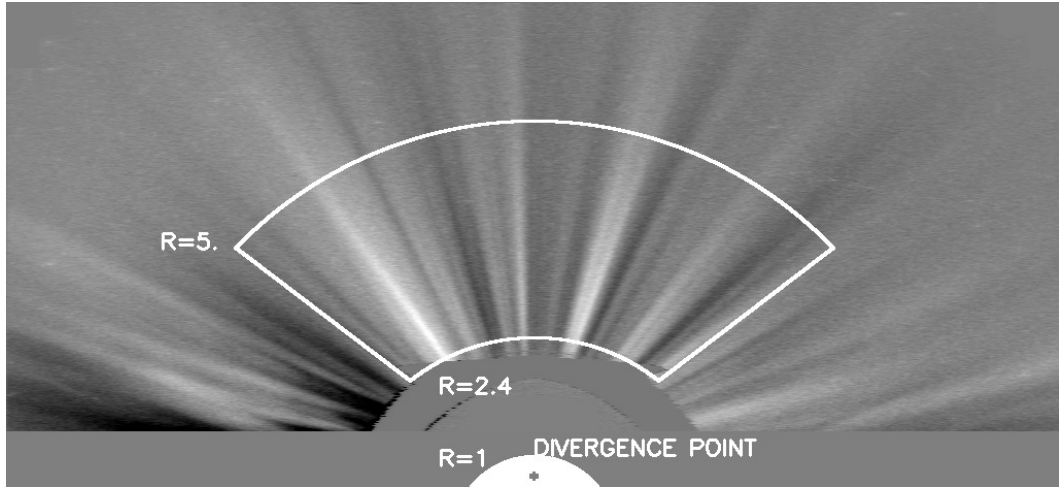
Figure 8: A processed image of plumes and IPRs at time, t_0, 21:31 UTC on 23 March 1997, i.e., 47 h into the 66 h sequence taken with LASCO-C2 from 21 to 24 March 1997. The F-corona, the stray light and the K-continuum are removed from this image. It is not corrected for vignetting in order to keep a uniform visual contrast. Notice the thin IPRs relative to the broad plumes. The intense ray at $\approx -50°$ is a high-latitude streamer crossing the FOV, in which the TID integration is performed along radial directions centred on the divergence point ($R_{\mathrm{div}} = 0.843\ R_\odot$) from 2.4 $R_\odot$ to 5 $R_\odot$ in the angular range between $\delta = -60°$ and $+60°$. This yields the integrated radiance, $L_{\mathrm{I}}(\delta, t_0)$, as function of angle at time t_0.

Figure 9: A TID, $L_I(\delta, t)$, of 21 to 24 March 1997. Horizontal axis: $\delta = -60°$ to $60°$. Vertical axis: time, t, with 66 h full scale (cf., Fig. 11 for labelled coordinate axes). Each horizontal line shows, at a specific time, the radially integrated radiance of the FOV indicated in Fig. 8. The global fluffy aspect is characteristic of frac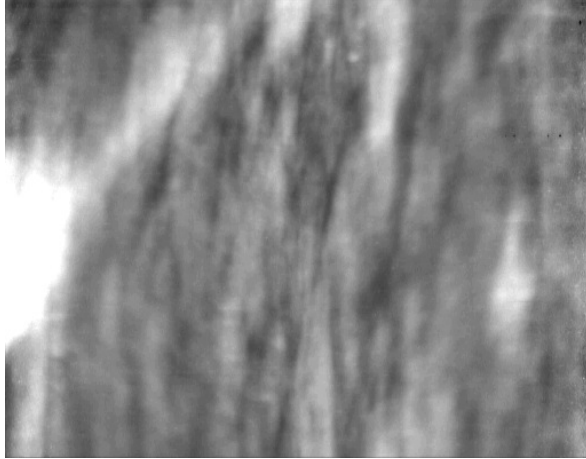tal images. IPRs (in dark) are sharper than bright plumes. On the left side, a streamer crosses the FOV. The overall texture shows an inclination of $7°$ caused by the polar tilt angle relative to the plane of the sky at that time (from Llebaria et al. 2002a).

implication that CHs have a fibrous structure might indicate that the beam plumes mentioned earlier should indeed not be thought of as compact entities.

In order to analyse the spatio-temporal evolution of WL plumes, special sequences of LASCO-C2 images were obtained in 1997, 2007 and 2010. These sequences employed a high cadence (one image every 9.9 min) and high signal-to-noise ratios (through an overexposure by a factor of four). This increased the visibility of changes in structural details. A time intensity diagram (TID) has been constructed in Fig. 9, using a variant of the sinogram technique (Lamy et al. 1997), by compiling 402 images taken with LASCO-C2 in March 1997. It shows that not only the spatial distribution is of a fractal type, but also the temporal evolution (Llebaria et al. 2002b). Plume trajectories could be tracked for many hours (see also Fig. 11) and statistics obtained on duration and intermittence along the trajectories as well as on the distribution of projected speeds of plume propagation into the corona. The apparent speeds peaked at 300 $\mathrm{km\,s^{-1}}$ with a median value of ≈ 400 $\mathrm{km\,s^{-1}}$. The speeds are deduced by fitting straight lines to the local profiles of brightness in Fig. 10. The high variability of the estimates seem to indicate real outflows, rather than wave phenomena, for which the propagation speed would be constraint by the local plasma conditions.

The first derivatives of the TID are also very informative. The derivative in the angular direction facilitates the detection of plume trajectories and determines the relative position of each one on the CHs "plane" as shown in the left panel of Fig. 11. The derivative relative to time enhances the onset and extinction of plumes, but also unambiguously reveals in the right panel the appearance of jets with angular widths of less than $2°$ at 3.5 $R_\odot$ and lifetimes of ≈ 200 min (for more details on *jets* see Sect. 6.3).

4 Dynamics

The importance of wave phenomena for the generation and support of plumes is unclear and their life cycle is rather elusive as is the relation to the fast SW streams. In this context,
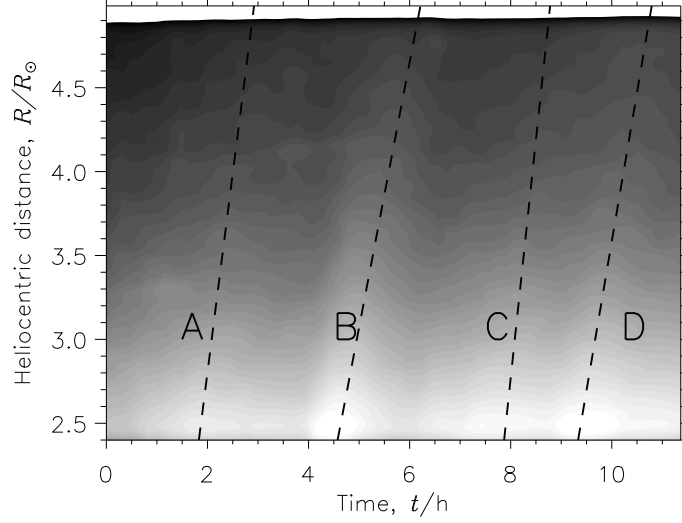
Figure 10: Brightness profiles along the trajectory of the plume which starts at a colatitude of 11.7° at 52.7 h in time, dimming at 11.5°, 64.2 h. The graph displays the logarithmic brightness in heliocentric distance from 2.4 $R_\odot$ to 5 $R_\odot$ versus time. In this example, the persistence was 11.5 h. The ejection speeds of the events A and C were ≈ 450 km s^{-1}, higher than the mean speeds of ≈ 300 km s^{-1} for B and D.
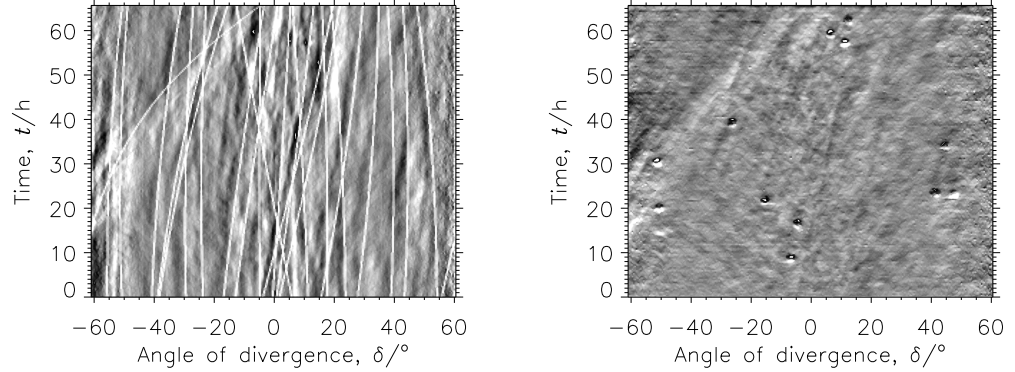
Figure 11: (Left panel) The TID derivative in the angular direction, $\partial L_{\mathrm{I}}(\delta, t)/\partial\delta$, with plume structures superimposed as black lines. (Right panel) The temporal derivative, $\partial L_{\mathrm{I}}(\delta, t)/\partial t$, indicating some jets as circular areas centred around each jet have been emphasized by a factor of two. A total of 12 jets were detected in the 66 h interval (from Llebaria et al. 2002b).

the following questions have been considered and are discussed in this section. – Are the characteristics of plumes changing within their life cycle? – Do plumes show a tendency of recurrence? – Is there wave activity that is characteristic of plumes and IPRs and how are

they related to heating processes and the SW acceleration? – It is established that the fast SW streams emanate from CHs: what are the outflow speeds in plumes and IPRs? – Are plumes or IPRs the main contributors to the fast SW streams?

4.1 Life cycle of plumes

DeForest et al. (1997) observed temporal changes of plumes on time scales of less than 10 min as brightenings of small filamentary structures of $\approx 5''$ width with relative radiance variations of ≈ 10 % and outward propagation speeds of 300 $\mathrm{km\,s^{-1}}$ to 500 $\mathrm{km\,s^{-1}}$. On the other hand, the shapes of the plumes on spatial scales of $\approx 30''$ (also typical for the network super-granulation, cf., Sect. 6.1) appeared to be nearly constant for hours to days (cf., Waldmeier 1955). Sinogram analyses of EIT and LASCO image sequences obtained in December 1996 indicated plume lifetimes from 0.5 d to 2 d (and longer for beam plumes, cf., Sect. 3.2) with a pronounced recurrence tendency for weeks at the same locations (Lamy et al. 1997; DeForest et al. 2001b). A certain magnetic flux tube therefore is only occasionally filled with high-density plume plasma. Plumes are episodic in nature, and are both transient and persistent.

The question of how long plumes last is difficult to answer, because plumes and IPRs cannot easily be separated in images over long time intervals. The transverse profile is characterized by a continuous succession of local minima and maxima. The apparent structure of plume profiles led Llebaria et al. (2002b) to the definition of an multi-resolution analysis. It deploys the initial profile in a set of diagrams with spatial scales of increasing size, and will thus progressively smooth the profiles. It turns out that there is a strong correlation between the size level and the time duration as can be seen in Fig. 12. However, because plumes are intermittent phenomena, these results are to some degree dependent on the choice of the activity threshold.

The formation of a plume above a BP has been observed in the 17.1 nm band of EIT followed by the disappearance of the BP before the plume faded away within ≈ 28 h in May 1997 (Wang 1998). The chromospheric evaporation time scale of ≈ 6 h appears to control the formation of the plume and the radiative cooling time of ≈ 4 h its decay. Del Zanna et al. (2003) observed diffuse plumes without BPs at their base and a near isothermal temperature of ≈ 0.8 MK. The authors suggest that the plumes with BPs might represent an early stage of plume evolution; and Newkirk and Harvey (1968) speculated that the most long-lived flux concentrations might underlie plumes. It must, therefore, be concluded that the magnetic configuration of a plume is relatively stable, but that the processes generating the actual plume plasma operate only intermittently.

Raouafi et al. (2008) studied the relationship between polar coronal jets and plumes (see also Sect. 6.3). Multiple occurrences of short-lived, jet-like event were found at the base of long-lived plumes, suggesting that these brightenings might be the result of magnetic reconnection of continuously emerging flux and could contribute significantly to the length of the life cycle of these plumes.
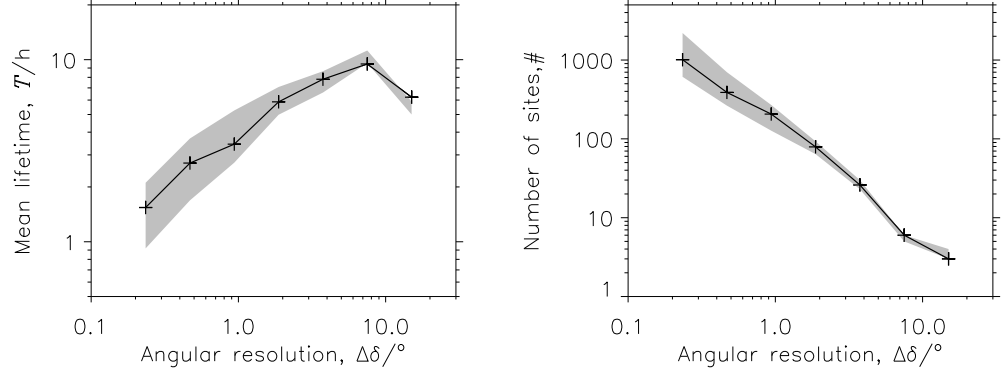
Figure 12: (Left panel) The distribution of the mean lifetime of WL plumes as function of the spatial resolution. (Right panel) Number of plumes identified in the TID of 66 h at the corresponding resolution. Grey areas shows the variability depending on the minimal gap (between 30 and 50 pixels) chosen to dissociate two successive plumes. The steep increase of the number of plumes with resolution speaks for a (fractal-like) fine structure of WL plumes (from Llebaria et al. 2004).

4.2 Waves and turbulence in plumes and inter-plume regions

Waves (usually Alfvén waves) are a very promising mechanism for transporting the energy from the solar surface into the corona, where they are partially reflected back down towards the Sun and dissipated by turbulent processes (see, e.g., Velli 1993; Matthaeus et al. 1999; Cranmer et al. 2007). A description of the concept of wave and turbulence-driven SW models can be found in Cranmer (2009) together with a list of recent reviews on in situ and remote sensing observations of waves. On the specific topic of observation of waves in plumes, we can refer to Banerjee et al. (2009b).

The detection of waves in the outer solar atmosphere is made possible by analysing the effects these waves have on the plasma. The presence or signature of compressional waves may be seen in the form of variations or oscillations in line radiance, due to change in plasma density, and also in the LOS velocities, due to plasma motions (when they have a significant component directed towards the observer). On the other hand, transverse waves give rise to only LOS effects when they propagate substantially over the plane of sky. Moreover, the latter give no radiance signature in the theoretical limit of incompressible Alfvén waves. Temporally and spatially resolved motions result in shifts of the observed profiles, whereas unresolved motions result in broadening of the spectral lines. These effects can, in principle, be measured from observations of spectral lines profiles, but the unresolved motions give rise to an ambiguity in separating thermal and turbulence effects, which plagues interpretation of some observations.

Quasi-periodic brightness variations in plumes have been observed with EIT by DeForest et al. (1997). On 7 March 1996, wave trains in several plumes were propagating outwards with periods between 10 min and 15 min and speeds between 75 $\mathrm{km\,s^{-1}}$ and 150 $\mathrm{km\,s^{-1}}$ in the height range from $h = 0.01\ R_\odot$ to 0.2 $R_\odot$. They have been identified as compressional waves (Ofman et al. 1997, 1999; DeForest and Gurman 1998). Plume oscillations with periods of 10 min to 25 min have also been detected in the O v 62.9 nm (0.24 MK) line by CDS

(Banerjee et al. 2000b), and with ≈ 10 min period in the WL channel of UVCS between h = 0.9 $R_\odot$ to 1.1 $R_\odot$. Their group velocity was ≈ 200 km s^{-1} (Ofman et al. 2000a). Ofman et al. (1999, 2000b) developed a visco-resistive 2.5D magnetohydrodynamic (MHD) model of plumes with propagating slow magnetosonic waves, and studied the effects of wave trapping in high density plumes, non-radial plume expansion, and solar wind outflow in plumes. The authors suggest that compressional waves are propagating upwards from the Sun, and more specifically, identified the oscillation as slow magneto-sonic waves in plumes with diameters of ≈ 30 Mm. On the other hand, these time scales are commensurate with the slow photospheric motions thought to drive Alfvénic (incompressible) fluctuations that propagate upwards and are implicated in heating at coronal altitudes (see, e.g., Dmitruk et al. 2002; Verdini et al. 2010). Consequently, it is not out of the question that plume formation and dynamics is in some way related to this broader issue. Very long-period activity (≈ 170 min) in a PCH has been reported by Popescu et al. (2005). In a review article, Ofman (2005) concluded that the energy flux in slow-mode waves is too small for all of the coronal heating and that other modes must be considered in addition.

Above BP groups, torsional Alfvénic perturbations have been detected through non-thermal broadenings of the H α line profile (Jess et al. 2009). The authors conclude that the energy flux of these waves is sufficient to heat the corona. Indirect evidence for Alfvén waves has been found in CHs by Banerjee et al. (1998, 2009a) as well as by Dolla and Solomon (2008) from measurements of line broadenings in spectra obtained with very long exposure times. The propagation and dissipation of Alfvén waves in plumes were discussed by Ofman and Davila (1995) using a 2.5D MHD model. The injection of Alfvén waves and the formation of a jet was recently studied by Pinto et al. (2010) using such a model.

Recently, Gupta et al. (2010) detected the presence of propagating waves in an IPR with a 15 min to 20 min periodicity — obtained from a wavelet analysis — and a propagation speed increasing from (130 ± 14) km s^{-1} just above the limb to (330 ± 140) km s^{-1} around $160''$ above the limb. The distant-time map of the Fe XII radiance over nearly 2 h is shown in the upper panel of Fig. 13. Although the waves are best seen in radiance, significant power at those periodicities is also detected in both Doppler width and shift. In the adjacent plume region (lower panel), propagating radiance disturbances also appear to be present (no spectral profiles are available) with the same range of periodicity, but with propagation speeds in the range of (135 ± 18) km s^{-1} to (165 ± 43) km s^{-1}. The plume observations might, however, be affected by the IPRs along the LOS, because of the low electron temperature in plumes, the high formation temperature of the Fe XII line (cf., Figs. 18 and 19) and the more favourable conditions for such emissions in IPRs. Based on the acceleration to supersonic speeds and the signature in Doppler width and shift, the authors suggest that in IPRs the waves are likely either Alfvénic or fast magneto-acoustic, whereas they are slow magneto-acoustic in plumes.

An important feature of turbulence models (Dmitruk et al. 2001) is the non-linear pumping of non-propagating "zero frequency" structures. These would appear in observations as strong transverse gradients. When present these "quasi-2D" fluctuations can catalyse a powerful cascade perpendicular to the large-scale magnetic field that may drive strong turbulent heating at fine transverse scales (e.g., Verdini et al. 2010). For this reason in considering turbulence models, it is essential to examine fluctuations that may not be described by any linear wave mode (see, e.g., Dmitruk and Matthaeus 2009). It is possible that plumes, with their characteristic transverse structure, may participate in these low-frequency dynamical couplings, and thus could play a direct rôle in coronal turbulence.
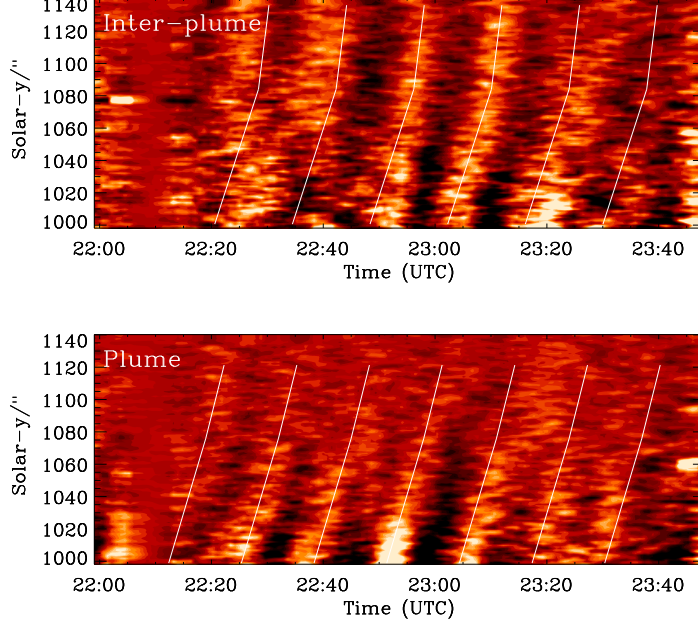
Figure 13: Maps of radiance along the slot (solar-y) versus time obtained by EIS in Fe XII on 13 November 2007 by averaging over $5''$ in the solar-x direction at the selected position. The maps were smoothed over ≈ 3 min and the background trend has been subtracted from each solar-y pixel along time. The height range shown covers the near off-limb and far off-limb regions of the PCH in an IPR (top panel) and a plume (bottom panel). The slanted lines represent the disturbances propagating outward with increasing speed. It can be seen that in some places the white lines do not coincide with the enhanced lanes but are nevertheless parallel to them. This suggests that even if the periodicity changes within a certain range, the propagation speeds are fairly uniform (after Gupta et al. 2010).

4.3 Outflows in plumes, inter-plume regions and coronal holes

Coronal plumes together with other dynamic structures in the solar atmosphere, such as spicules, macrospicules and chromospheric jets, are potential sources of the SW. The contribution of plumes to the fast SW has been disputed in the literature. Some studies indicate that plumes are a plausible source of the fast SW streams (Gabriel et al. 2003, 2005), and may even contribute one half of the fast SW. Other investigations led to different results (e.g., Wang 1994; Habbal et al. 1995; Wilhelm et al. 1998; Hassler et al. 1999; Giordano et al. 2000a, b; Teriaca et al. 2003).

Doppler dimming techniques — developed by Rompolt (1967) for moving prominences using the H α line — applied to the corona (cf., Kohl and Withbroe 1982; Noci et al. 1987) have supplied most of the outflow speeds summarized in Table 2 using UVCS and SUMER observations of the O VI 103.2 nm, 103.8 nm lines. In this and the following tables, typical results obtained for the relevant quantities (outflow speed, u_{out}; electron density, n_{e}; electron temperature, T_{e}; Doppler velocity, $V_{1/\mathrm{e}}$) by various researchers using different methods are

Table 2: Typical outflow speeds in CHs, plumes and IPRs at some representative heights

Height[a] $h/R_\odot$	Outflow speed, $u_{\mathrm{out}}/(\mathrm{km\,s^{-1}})$ CH[b]	PL	IPR	Method	Date, period	Reference
0.6	45^{+55}_{-20}	36^{+25}_{-20}		WL	12 Apr 1993	Habbal
1.2	130^{+50}_{-60}	70^{+70}_{-10}		Spartan and		et al. 1995
2.2	220	130		Mauna Loa		
0.5		≈ 50		O VI 103.2 nm,	Nov 1996	Corti
1.0		110		103.8 nm ratio		et al. 1997
0.5	11^{+38}_{-11}			Model[c]	Nov 1996/	Cranmer
1.0	179^{+78}_{-76} (150^{+49}_{-55})			B1: O^{5+}	Apr 1997	et al. 1999
2.0	402^{+44}_{-68} (219^{+30}_{-23})			(A1: H^0)[d]		
0.50	45 ± 10			O VI 103.2 nm,	21 May 1996	Antonucci
2.10	360 ± 40			103.8 nm ratio	SOHO roll	et al. 2000
0.72		0 to 65	105 to 150	O VI ratio[e]	Apr 1996	Giordano et al. 2000b
0.05			67^{+16}_{-14}	O VI ratio	26 Feb 1998 eclipse	Patsourakos and Vial 2000
0.4	62 ± 5 (60 ± 5)			Semi-empirical	Aug 1996	Zangrilli
1.0	234 ± 20 (154 ± 5)			models:		et al. 2002
1.5	370^{+60}_{-90} (232 ± 30)			O^{5+} (H^0)[d]		
0.05		≈ 90[f]	23	O VI ratio	21 May 1996	Gabriel
0.20		≈ 80	30			et al. 2003
0.36		≈ 85	48			
0.10		static	< 25	O VI ratio[e]	3 Jun 1996	Teriaca
0.50		or	49 ± 28			et al. 2003
0.75		slow	84 ± 21			
1.00		outflow	164 ± 38			
2.1	359 to 500			O VI ratio u_{out}, n_{e}	21 May 1996	Antonucci et al. 2004
0.05		60	30	O VI ratio	21 May 1996	Gabriel
0.60		78	83			et al. 2005
1.00		115	150			
1.40		130 ± 20	180 ± 20			
0.92		124 ± 5		O VI ratio	29 Mar 2006	Abbo
1.07			208^{+41}_{-27}		eclipse	et al. 2008

[a] above the photosphere
[b] not separated into plume (PL) and IPR
[c] parallel motions in thermal equilibrium with electrons
[d] hydrogen speeds in parentheses
[e] depends on isotropy assumptions
[f] with a plume filling factor of $F = 0.5$

compiled in order to provide an overview. Many numbers are taken from diagrams in the referenced papers and are consequently given in rounded values. If uncertainty margins are available in the original articles in appropriate formats (either in tables or diagrams), they are quoted in the tables with the qualification that their significance varies for different sources. Our aim is to present a large number of observations and identify any systematic behaviour.
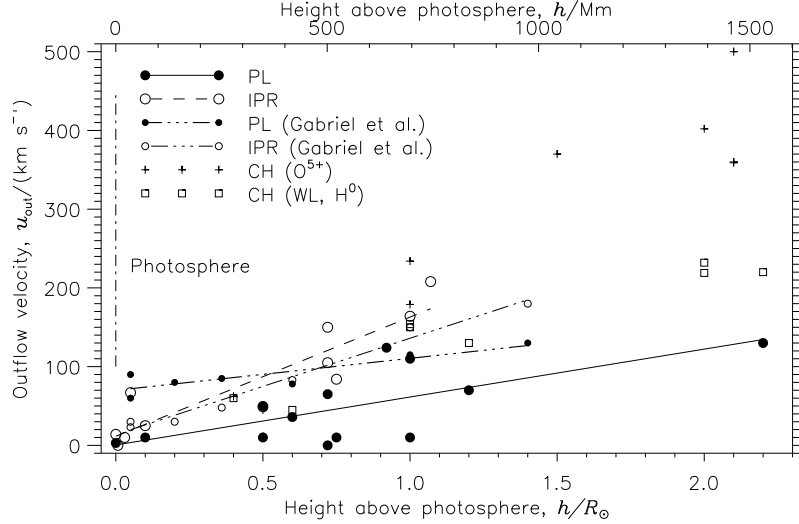
Figure 14: Plasma outflow velocities in plumes, IPRs and CHs from data in Table 2 and references cited in the text. The values obtained by Gabriel et al. (2003, 2005) are plotted with smaller symbols compared to those of other authors. Separate linear fits are shown for four groups of data in different line styles. The speeds of O^{5+} in CHs are consistently higher than those of H^0.

Since we are comparing solar features over a period of more than one solar cycle the variations are, in all likelihood, in many cases larger than any measurement uncertainties. Nevertheless it should be pointed out that the stability of the CH conditions during the activity minima is remarkable.

From Table 2 and Fig. 14, it is clear that the outflow speed in IPRs increases rapidly in the low corona to high values of $u_{out} \approx 200$ km s^{-1} within a distance of 1 $R_\odot$. The cases for which only undifferentiated CH outflow speeds have been published seem to be related more to IPRs than to plumes. Below $h \approx 0.5$ $R_\odot$, faster and slower outflow speeds in plumes than in IPRs have been deduced in different investigations. These conflicting findings were one of the motivations for this study and, consequently, they have to be addressed in some detail. Casalbuoni et al. (1999) concluded in a study of pressure-balanced structures (PBS) that the temperature difference between plumes and IPR has a decisive effect on the outflow speed. Since there is strong evidence that plumes are cooler than IPRs both in the electron temperature, T_e, and the effective ion temperature, T_{eff}, above $h \approx 0.03$ $R_\odot$ (cf., Table 4 and Sect. 5.2.2), it follows that plumes must be slower. However, it has also been shown that a plume cannot be maintained if it is cooler than the IPR at all heights. An additional heat input at the base of a plume is required for a significant density enhancement (Del Zanna et al. 1997). Such a scenario is consistent with the association of BPs and plumes (cf., Sect. 6.2) and the plume model of Wang (1994) (cf., Sect. 8). In this context, it must be noted that the electron density height profile assumed in the evaluation of the outflow speeds plays an important rôle and that very different densities had been assumed in various studies. Moreover, we point out that the ion temperature in the direction perpendicular to the LOS has to be known for a determination of the outflow speed with the help of the Dopper dimming technique. Although there is strong evidence for temperature anisotropies of heavy ions in IPRs and, possibly, in plumes (Cranmer et al. 1999; Giordano et al. 2000b; Teriaca et al. 2003), different assumptions on the degree of anisotropy led to different results.

At very low altitudes ($h \leq 0.03$ $R_\odot$), LOS Doppler velocities of ≈ 10 km s^{-1} (corresponding

to radial speeds of ≈ 14 km s^{-1} at the observation site) in the Ne VIII 77.0 nm line are only seen in darker regions of a CH. A relatively strong plume that could be identified on the disk showed a speed of less than ≈ 3 km s^{-1} (cf., Sect. 3.1; Hassler et al. 1999; Xia et al. 2003). Rather high radiance values in the TR line Si II 153.3 nm (27 000 K) near the plume footpoint had been found in the same data set, indicating enhanced heating at the base of the plume. Tu et al. (2005) found no outflow of C^{3+} ions at a height of 5 Mm, but a LOS velocity of ≈ 10 km s^{-1} in funnels of the same CH at 20 Mm (for Ne^{7+}). However, no significant outflow could be detected in a magnetic plume structure (cf., Sect. 3.1). It thus appears as if, indeed, the IPRs have larger outflow speeds along a height profile and, together with the small filling factor of plumes in CHs, provide the main contribution to the fast SW streams as suggested by Wang (1994). The funnels harbouring the outflows seen in Ne VIII are most likely rooted in flux concentrations described by Tsuneta et al. (2008b). The picture of expanding coronal funnels is supported by the findings of Tian et al. (2010) that increasingly larger patches of blue-shifted line profiles (outflows) are observed in hotter spectral lines with EIS in the on-disk part of a PCH.

Raouafi et al. (2007b) studied the plasma dynamics (outflow speed and turbulence) inside coronal polar plumes and compared line profiles (mainly of O VI) observed by UVCS at the minimum between solar cycles 22 and 23 with model calculations. Maxwellian velocity distributions with different widths are assumed for both plumes and IPRs, and different combinations of the outflow velocities, u_{out}, and most-probable speeds, $V_{1/e}$ (cf., Sect. 5.2.2) are considered. The observed profiles are reproduced best by low outflow speeds close to the Sun in plumes that increased with height to reach IPR values above $h \approx 3$ $R_{\odot}$. The most-probable speeds in plumes and IPRs assumed are included in Table 5.

In equatorial coronal holes (ECH), with characteristics very similar to PCHs, outflows along open field lines can be detected in spectral lines with formation temperatures above 0.1 MK (cf., Sect. 5.2.1). An average outflow speed of $u_{\mathrm{out}} \approx 5$ km s^{-1} was measured for Ne^{7+} ions and of ≈ 10 km s^{-1} for Mg^{8+} (Wilhelm et al. 2002a; Xia et al. 2004; Wiegelmann et al. 2005). Woo (2007) summarized outflow observations as filamentary structures on open field lines within the so-called closed corona.

On balance, there seems to be some evidence that IPR outflow speeds become significantly greater than outflows in plumes at increasing altitude in the lower corona. In this context, Sheeley et al. (1997) made an interesting remark on the direction of time that can always be identified in coronal streamers, but not in polar coronal plumes—implying that the outflow signatures in plumes are less pronounced.

5 Plasma conditions in coronal holes

The knowledge of the plasma conditions in plumes and their environment in CHs is critical for an understanding of the plume physics. We asked questions as follows: – Can *standard* height profiles of the electron density in plumes and IPRs be defined considering that the measurements obtained with various methods agree remarkably well within the general variability of solar features? – Specifically, what is the plume/IPR density ratio and its potential variation with height? – What are the plume and IPR electron and ion temperatures as a function of height? – Is there a significant anisotropy of the ion temperatures in plumes and IPRs? – What can be said about the elemental abundance in plumes and IPRs, and, specifically,
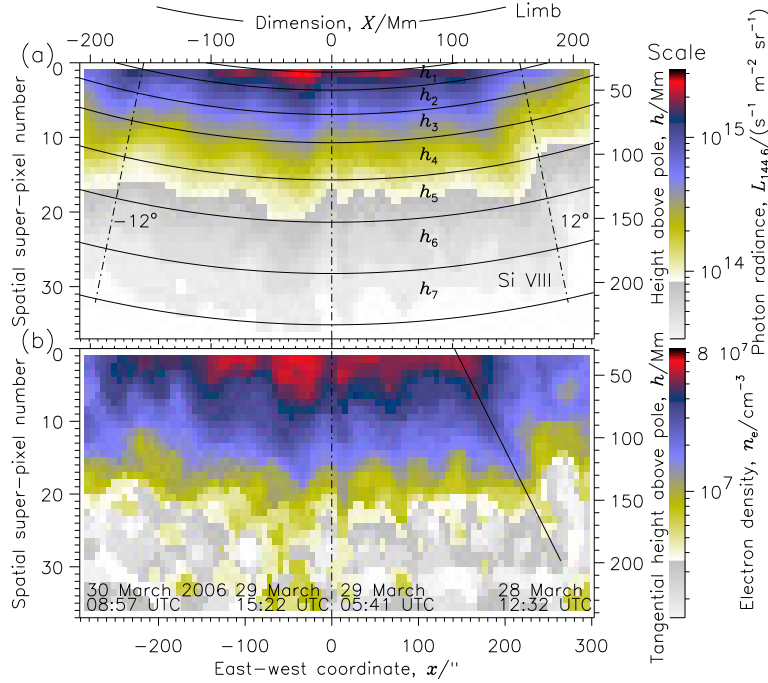
Figure 15: (a) Radiance of the Si VIII 144.6 nm line in the southern CH before and after the total eclipse on 29 March 2006. During the actual eclipse, the scan was interrupted in favour of high-cadence O VI observations, an example of which is shown in Fig. 26. The concentric height ranges, h_1 to h_7, outline the data selection in Fig. 16b. Radius vectors at $\pm 12°$ are indicated. (b) Electron density determined from the LOS Si VIII line ratio $L_{144.6}/L_{144.0}$. The projection of a plume near $x = 200''$ is shown for a comparison with the radius vector in panel (a).

about the first-ionization potential (FIP) effect? – What is the expected FIP and ionization state signature of plumes in the SW, given a hypothesis for their source? – Is it agreed that there are different plasma regimes present along the LOS in CH observations — plumes and IPRs?

A brief discussion of the resulting plasma pressures is included in Sect. 6.4.

5.1 Electron densities in plumes and inter-plume regions

Above the solar limb, coronal plumes seen in WL appear brighter than the surrounding medium which led many authors to the conclusion that they are denser than the background corona (called here IPR) (van de Hulst 1950b; Saito 1965a; Koutchmy 1977; Ahmad and Withbroe 1977; Fisher and Guhathakurta 1995). The density measurements in WL utilize the fact that Thomson scattering of electrons produces polarized light, whereas the much stronger F-coronal radiance from dust particles is unpolarized. The polarized brightness

$$pB = \sqrt{Q^2 + U^2} \quad , \tag{1}$$

with Q and U the relevant Stokes parameters, then has to be related to the electron density along the LOS taking into account the dependence of pB upon the distance from the plane of the sky (cf., Koutchmy and Bocchialini 1998).

VUV observations rely on atomic data for a determination of the electron density from line-ratio measurements. In the polar corona the nitrogen-like ion Si^{7+} and its magnetic dipole transitions $2s^2 2p^3\, ^4S_{3/2} - 2s^2 2p^3\, ^2D_{3/2}$ and $2s^2 2p^3\, ^4S_{3/2} - 2s^2 2p^3\, ^2D_{5/2}$ with the corresponding

emission lines Si VIII 144.6 nm and 144.0 nm provide a convenient means of deducing n_e through the radiance ratio $R_{Si} = L_{144.6}/L_{144.0}$. It is density sensitive, because de-excitation of the $D_{5/2}$ level occurs not only radiatively, but also collisionally (see Laming et al. 1997; Doschek et al. 1997 for a conversion procedure). Compared with this procedure, the electron densities determined from R_{Si} with the help of the CHIANTI atomic data base yield slightly higher values (Banerjee et al. 1998). Warren and Hassler (1999) discussed, in addition, other density-sensitive line ratios, and derived CH densities that are in good agreement with the Si VIII values. In an ECH, Del Zanna and Bromage (1999) measured coronal electron densities of $n_e \approx 3 \times 10^8$ cm^{-2} (approximately a factor of two lower than in the adjoining QS regions). A selection of typical electron density measurements, obtained with the help of spacecraft and eclipse observations, is compiled in Table 3 for some representative heliocentric distances.

For an isothermal plasma, optically thin for a certain emission line, the LOS-integrated electron density (along the z direction) can be deduced from $\int n_e^2 \, dz$, the emission measure (EM) (see, e.g., Raymond and Doyle 1981), which in turn can be obtained from radiance observation, if the electron temperature and the element abundance are known (cf. Sects. 5.2.1 and 5.3). It is important to note that the Thomson scattering depends linearly on the electron density, whereas the emission process is a function of n_e^2. So that WL observations yield the mean value of the electron density, $\langle n_e \rangle$, whereas spectroscopic line ratios yield $\sqrt{\langle n_e^2 \rangle}$. These will not be the same where there are inhomogeneities in the plasma, and there is some evidence for this. Such inhomegeneities could have different scales, for example beam plumes and IPRs, network plumes, or even much finer structures due to turbulence.

A radiance map of the southern low corona in the Si VIII 144.6 nm line during the eclipse campaign 2006 is shown in Fig. 15a together with the electron densities in panel (b), derived from the $L_{144.6}/L_{144.0}$ photon radiance ratio observed in 96 raster steps of the SUMER slit from W to E. The height resolution is limited by the count statistics to a super-pixel of eight detector pixels. Several plume signatures with enhanced density can be identified. The line-ratio method — as applied here so far — obviously suffers from LOS effects if there are density (and temperature) variations along the integration path, complications discussed by Habbal et al. (1993). The polarization brightness, on the other hand, depends more on the conditions near the plane of the sky (Munro and Jackson 1977; Koutchmy and Bocchialini 1998), so that plumes and IPRs can probably be separated more effectively. From an analysis of the polarized K-corona measurements obtained with the EKPol polarimeter, electron density profiles have been derived in plume and IPR structures for the total eclipse on 29 March 2006 (Abbo et al. 2008; see Table 3 for representative values).

In an attempt to improve the separation of plume and IPR plasma regimes with the help of line-ratio observations, the radiances $L_{144.6}$ and $L_{144.0}$ measured with SUMER on 29 March 2006 are plotted in Fig. 16(a) and (b) averaged over certain height intervals per W-E step. In the upper panel, linear fits are calculated from data points obtained along tangential height ranges following a procedure developed earlier for 2005 observations (Wilhelm 2006). In the lower panel, the same measurements are organized according to concentric height ranges defined in Fig. 15. The highest range, h_7, has been omitted, because the data were too noisy. In both plots, the extrapolations of the linear fits do not pass through the origins of the diagrams as indicated for the lowest heights, h_1 and h_2 in panel (a). The only explanation for this behaviour appears to be that more than one density regime is encountered at most of the LOS directions. Under the assumption that the lowest radiances observed for each height range — encircled in panel (b) — represent pure IPR plasma (or at least the best estimate

Table 3: Typical electron densities in plumes and IPRs at some heliocentric distances

Distance[a] $R/R_\odot$	Density, $n_{\mathrm{e}}/(10^7\ \mathrm{cm}^{-3})$ PL	IPR[b]	Method	Date, period	Reference
1.20	20	4	WL isophots	1900 eclipse	van de Hulst 1950b
1.18	10	2.8	Eclipse,	1962 eclipse	Saito 1965a, b
1.33	4	1.1	WL radiance		
1.67	1	≈ 0.2			
1.10	$\approx 10^{\mathrm{c}}$	0^{d}	Eclipses, WL radiance	1962, 1963, 1965	Newkirk and Harvey 1968
2.00		0.052	WL	Jul	Munro and
2.50		0.013	coronagraph	1973	Jackson 1977
5.00		0.0013	Skylab[e]		
1.60	$0.21_{\pm0.07}$	$0.08_{\pm0.03}$	Spartan	11/12 Apr	Fisher and
2.00	$0.05_{\pm0.008}$	$0.02_{\pm0.003}$	201-01	1993	Guhathakurta
4.00	$0.003_{\pm0.0005}$	$0.001_{\pm0.0002}$	WLC (pB)		1995
1.5	$0.32^{+0.09}_{-0.08}$		O VI 103.2 nm,	Nov 1996	Corti
2.0	0.042		103.8 nm		et al. 1997
2.3	0.017		(EM)		
1.02		$8.0_{\pm0.5}$	Si VIII 144 nm,	4 Nov 1996	Doscek et al.
1.10		$3.0_{\pm0.5}$	144.6 nm		1997
1.30		$0.4^{+0.4}_{-0.3}$	line ratio		
1.10	$7_{\pm1}$	1.0	Eclipses (WL)		Koutchmy and
1.50	$0.2_{\pm0.06}$	0.1	star calibr.		Bocchialini 1998
1.03	$13_{\pm3}$	$8_{\pm4}$	Si VIII	Nov 1996/	Wilhelm
1.08	$6_{\pm2}$	$5_{\pm2}$	line ratio	Jan 1997	et al. 1998
1.30	$2.0_{\pm0.5}$	$0.73_{\pm0.3}$			
1.03		11	Si VIII	May, Nov,	Banerjee
1.26		1.6	line ratio	Dec 1996	et al. 1998
1.05	5.0	3.0	Si VIII	3 Sep 1997	Wilhelm and
1.10	3.4	1.7	line ratio	SOHO roll	Bodmer 1998
1.05		15	SUMER	Nov/Dec	Doyle
1.30		1.5	(Si VIII)	1996	et al. 1999
2.00		0.02	UVCS (WL)	1996/1997	
8.00		0.0004	LASCO (WL)	1996	
1.00	20^{+5}_{-4}	$11_{\pm4}$	Si IX 34.2 nm,	Aug/Sep	Fludra et al.
1.10	$8_{\pm2}$		35.0 nm ratio[f]	1996	1999
1.00	45^{+55}_{-20}	$16_{\pm6}$	Si IX[g]	25 Oct 1996	Young et al.
1.10	40^{+140}_{-40}	7^{+3}_{-2}	line ratio		1999
1.015	$22_{\pm4}$		Ne VII line ratio	27 Aug 1996	Warren and Hassler 1999

Continued on next page

---

[a] values at the base of the corona are indicated by $R = 1\ R_\odot$
[b] below $R < 1.05\ R_\odot$ some plume projections seem to merge and could hide IPRs
[c] density at centre of cylindrical plume
[d] no electrons outside plumes assumed
[e] CH values not separated into PL and IPR
[f] Pl values from spatial averages with IPR contributions
[g] CDS observations of very strong plume with jet characteristics; Si IX (1.15 MK)

Table 3: continued

Distance $R/R_\odot$	Density, $n_\mathrm{e}/(10^7\ \mathrm{cm}^{-3})$ PL	IPR	Method	Date, period	Reference
1.102	13.2	2.87	Eclipse	26 Feb 1998	Lites et al. 1999
1.60	0.342	0.0883	(WL)		
2.20		0.0159			
1.03	20 to 50		Eclipses	1994 to 1998	Hiei et al. 2000
1.20	1 to 7		(WL)		
1.05	5.2	1.9	Si VIII ratio	3 Sep 1997	Dwivedi et al. 2000
1.05	6.4	3.0	Mg VIII ratio[g]	SOHO roll	
1.4		3.09 ± 0.1	O VI 103.2 nm,	Aug 1996	Zangrilli
2.0		0.40 ± 0.03	103.8 nm,		et al. 2002[e]
2.5		$0.14^{+0.04}_{-0.03}$	H I Ly α		
1.00	120 ± 20	50 ± 20	Line ratios	Oct 1997	Del Zanna et al. 2003
1.00	≈ 10	≈ 5		Aug 1996	
1.70		0.08 ± 0.03	O VI 103.2 nm,	21 May 1996	Antonucci
3.10		0.003 ± 0.001	103.8 nm		et al. 2004[e]
1.07	6.9	1.3	Si VIII	24 May 2005	Wilhelm 2006
1.11	4.1	1.1	line ratio		
1.19	3.4	0.78			
1.03		13^{+3}_{-2}	Si VIII	3 Nov 1996	Landi 2008
1.12		2.8 ± 0.3	line ratio		
1.2	1.5 ± 0.3	1.3 ± 0.3	EKPol	29 Mar 2006	Abbo et al. 2008
1.5	0.19 ± 0.04	0.18 ± 0.04	polarimeter	eclipse	
2.0	0.022 ± 0.004	0.021 ± 0.004	pB		
1.03	22	19	Fe XII 18.7 nm,	10 Oct 2007	Banerjee et al. 2009a
1.15	16	8.7	19.5 nm ratio		
1.06 (h_1)	4.5 (4.5)	0.68 (2.34)	Si VIII ratio[h,i]	28/29 Mar	this work
1.14 (h_4)	2.7 (3.5)	0.52 (1.09)	tangential	2006	
1.24 (h_6)	1.3 (2.3)	0.13 (0.17)	(concentric)		
1.04 (h_1)	8.0 (5.1)	1.1 (3.9)	Si VIII ratio[j]	7/8 Apr	this work
1.13 (h_4)	4.4 (6.0)	0.52 (1.2)	tan. (con.)	2007	

[e] see previous page

[g] Mg VIII (0.79 MK)

[h] Ratios: $\rho_\mathrm{PL}^{\tan}(h_1, h_4, h_6) = (5.93, 4.05, 2.43)$; $\rho_\mathrm{IPR}^{\tan}(h_1, h_4, h_6) = (1.77, 1.50, 1.00)$;
$\rho_\mathrm{PL}^{\mathrm{con}}(h_1, h_4, h_6) = (4.54, 3.46, 2.31)$; $\rho_\mathrm{IPR}^{\mathrm{con}}(h_1, h_4, h_6) = (2.34, 1.09, 1.69)$

[i] margins of correlation coefficients ($3\,\sigma$) given in Fig. 16

[j] Ratios: $\rho_\mathrm{PL}^{\tan}(h_1, h_4) = (8.90, 5.79)$; $\rho_\mathrm{IPR}^{\tan}(h_1, h_4) = (2.18, 1.56)$;
$\rho_\mathrm{PL}^{\mathrm{con}}(h_1, h_4) = (6.50, 7.30)$; $\rho_\mathrm{IPR}^{\mathrm{con}}(h_1, h_4) = (5.24, 2.41)$

we can get), the ratio of these radiances then provides the density of the IPR plasma.[7] The highly significant regression lines allow us to conclude that there must be (at a given height) another plasma with a rather well-defined higher density as determined from the slopes. A varying amount of this "plume" plasma is sampled at different LOS positions. The variations caused by the reduced IPR contribution are not significant, in particular, as the longest path

---

[7]This method has some similarities with the radial background subtraction employed by DeForest and Gurman (1998).
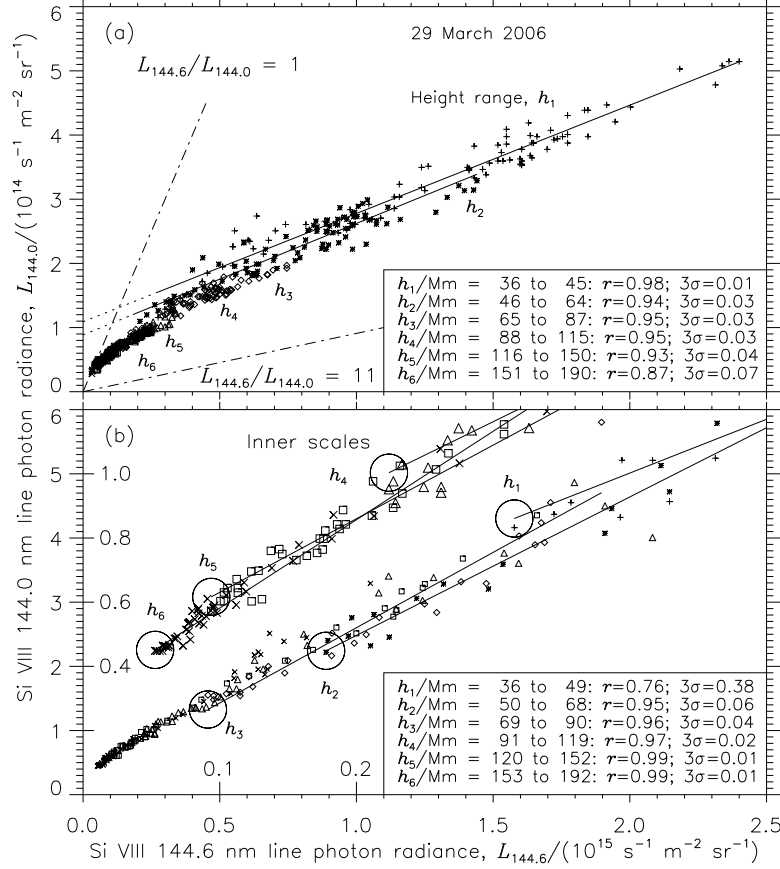
Figure 16: Radiance of the Si VIII 144.0 nm line as a function of the 144.6 nm radiance (a) in tangential height ranges and (b) in concentric rings (see Fig. 15). The correlation coefficients, r, the confidence levels and the height ranges, h_1 to h_6, are given. Some of the linear fits are shown. To highlight the crowded low-radiance portion of the diagram, it is repeated in (b) increased by a factor of five in both axes and with larger symbols. The line labelled $L_{144.6}/L_{144.0} = 1$ shows the asymptotic value of the ratio reached at $n_e \approx 1 \times 10^6$ cm^{-3}, whereas $L_{144.6}/L_{144.0} = 11$ corresponds to an electron density of $n_e = 1 \times 10^8$ cm^{-3}.

length through plume material is small relative to that of the low-density plasma (cf., Sect. 3).

The observations taken in April 2007 led to diagrams very similar to those shown in Fig. 16, and some of the 2007 results are included in Table 3. Considering that atomic physics data could have higher uncertainties than the measurements, the actual line ratios, $\rho = L(144.6 \text{ nm})/L(144.0 \text{ nm})$, observed in 2006 and 2007 are given in table footnotes for a future re-evaluation should new conversion functions become available.

Electron densities range up to about 10^9 cm^{-3} in plumes (Young et al. 1999; Del Zanna et al. 2003), with little decrease over the first 70 Mm in height. The IPR density at the base of the corona is $\approx 10^8$ cm^{-3} and falls sharply with height. This can be seen from Fig. 17, where the data are plotted versus heliocentric distance. Results for $R = 1\ R_\odot$ have been omitted, because they are probably not directly related to the plume densities, but to the base heating or an associated BP.[8] The data are plotted together with an empirical fit to the electron densities

$$n_e = \left[\frac{1 \times 10^8}{(R/R_\odot)^8} + \frac{2.5 \times 10^3}{(R/R_\odot)^4} + \frac{2.9 \times 10^5}{(R/R_\odot)^2} \right] \text{cm}^{-3} \quad , \tag{2}$$

[8] An example of such a situation can be found in Fig. 3 of Banerjee et al. (2009a).

32

derived by Doyle et al. (1999) for IPR conditions. Also shown are hydrostatic density curves adjusted to the plume and IPR data points by selecting appropriate base densities, $n_{e,0} = n_e(R_\odot)$, and hydrostatic temperatures, T_S:

$$n_e^{PL,IPR}(R) = n_{e,0}^{PL,IPR} \exp \left[\frac{G_N \, M_\odot \, m_p \, \mu}{k_B \, T_S^{PL,IPR}} \left(\frac{1}{R} - \frac{1}{R_\odot} \right) \right] \quad , \tag{3}$$

where G_N is the gravitational constant, $M_\odot$ the mass of the Sun, m_p the proton mass, k_B the Boltzmann constant and $\mu = 0.56$ for a fractional helium abundance of $n_\alpha/n_p = 5\%$ (cf., Bame et al. 1977). However, with the high outflow speeds that have been observed in IPRs, the hydrostatic model does, in all likelihood, not provide a viable option for that case.

Considering that the various data points and the fits have been obtained with the help of different methods and observations of many plumes and IPRs spread over several years in two sunspot minimum periods, it must be concluded that the excellent agreement can only be explained, if CH conditions in general are remarkably stable. It therefore appears to be reasonable to assume standard plume and IPR densities close to the graphs in Fig. 17 and examine, in particular, the density ratio between these plasma regimes. If we take the power-law fits at face value, we find a plume-IPR density ratio of three below $R = 2 \, R_\odot$ with $n_e \propto (R_\odot/R)^8$ both in plumes and IPRs. Above $R = 3 \, R_\odot$, it is $n_e^{PL} \propto (R_\odot/R)^3$, whereas the IPR density n_e^{IPR} is proportional to $(R_\odot/R)^2$. In the low corona, the densities of plumes and IPRs thus decline at the same rate. Higher up, the plume densities seem to decrease faster than those of IPRs and the density ratio becomes smaller. This ratio is four to seven in the low corona from WL eclipse observations, but, in general, the value is near two if obtained from LOS line-ratio studies, such as that in Fig. 15. This discrepancy could be resolved by the above consideration of density variations along the LOS caused by two plasma regimes in Fig. 16, leading to density ratios in agreement with WL observations.

5.2 Plasma temperatures and non-thermal motions

5.2.1 Electron temperature

Early electron-temperature determinations of CH plasmas have been summarized by Habbal et al. (1993). Data obtained in wavelength ranges from X-rays to WL as well as charge-state measurements have been considered together with relevant evaluation methods. The conclusion was that large uncertainties have to be accepted and that T_e increases in CHs between $h > 0$ and $h = 0.6 \, R_\odot$ from 0.8 MK to ≈ 1.3 MK with some indication of higher temperatures on the disk.

Typical temperatures found in CHs, IPRs and plumes (using methods described below) during the last two decades are summarized in Table 4 and Fig. 18. It appears as if the temperature increase with height in CHs is mainly related to IPRs, but is not typical for plumes. The electron temperature in the solar corona can be measured using several different methods, most of them depend, at this stage, on the observations of electromagnetic radiation from atoms and ions: Under the assumption of ionization equilibrium, the ionic fractions of the various species in a plasma as a function of the electron temperature can be determined (cf., e.g., Mazzotta et al. 1998). The excitation and de-activation processes of the species also depend on the electron temperature. For allowed transitions, spontaneous photon emission,
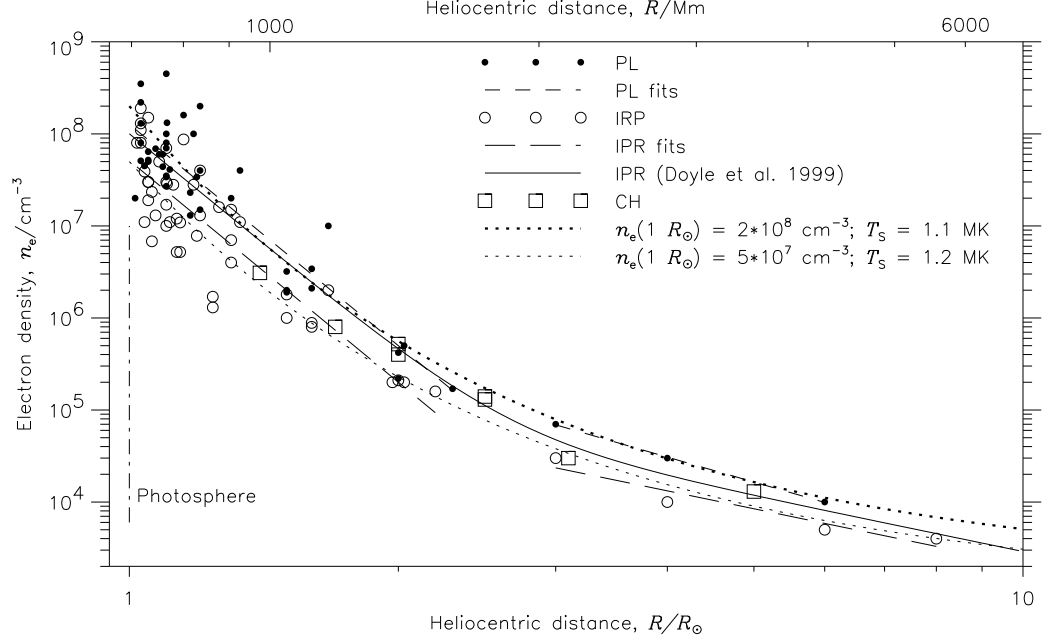
Figure 17: Electron density measurements inside plumes and IPRs plotted from data in Table 3, except for the values at $R = 1\ R_\odot$. Undifferentiated CH values are also shown. The short and long dashed lines show power-law fits to the values smaller and greater than $R = 2.5\ R_\odot$ for plumes and IPRs, respectively. The solid curve is the density profile according to Eq. 2. Density profiles of plumes and IPRs under hydrostatic conditions are shown as dotted lines. The initial conditions have been adjusted to produce best visual fits to the profiles.

in general, is the dominant de-activation process. It is controlled by the contribution function

$$G_{jg}(T_e) = \frac{n_g}{n_X}\ \frac{1}{\sqrt{T_e}}\ \exp\left(\frac{-\Delta\epsilon_{gj}}{k_B\,T_e}\right) \quad , \tag{4}$$

where n_g/n_X is the ionic fraction of the element X, if most of the ions are in the ground state and $\Delta\epsilon_{gj}$ the energy difference between the states g and j (cf., Pottasch 1963; Gabriel and Jordan 1973; Mariska 1992; Wilhelm et al. 2004).

The ionic fractions and contribution functions of some ions and their emission lines of importance in this context are plotted in Fig. 19. Most of the contribution functions have a pronounced maximum at an electron temperature that is called the formation temperature, T_F, of a spectral line. The N polar region of the Sun is shown in Fig. 20 as four monochromatic images simultaneously obtained in a raster scan with SUMER. In the C I image (shown without background subtraction) the chromospheric network is prominent. It can also be seen in the O V image together with many short, irregular spikes of spicule and macrospicule activity. Only the Mg X image exhibits coronal plumes. The knowledge of T_F of the spectral lines allows us to conclude that plumes are hotter than 0.24 MK and cooler than 1.38 MK. Note in this context that the plume structures seen in EIT 19.5 nm images are not related
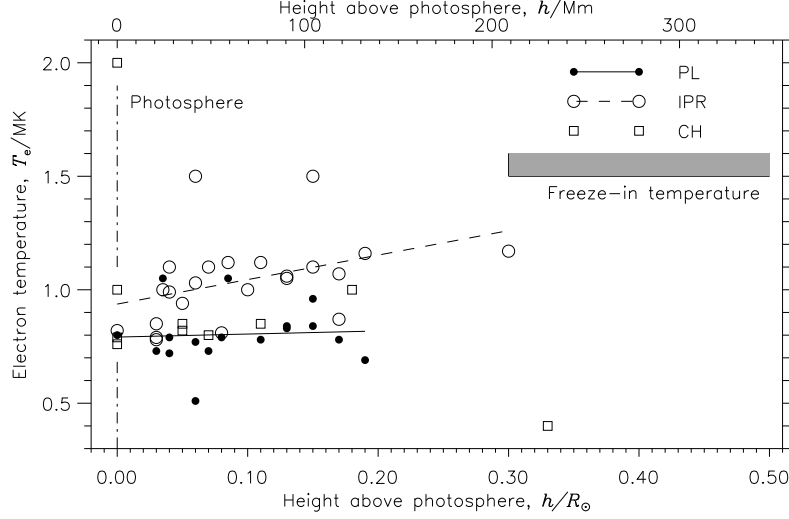
34

Figure 18: The electron temperatures summarized in Table 4 from line-ratio and DEM studies are displayed together with the temperature range consistent with charge-state measurements in the fast SW. The CH temperature of 2 MK at $h = 0$ is probably related to a BP. A linear fit of the plume data is plotted as solid line and that for the IPR values as dashed line.
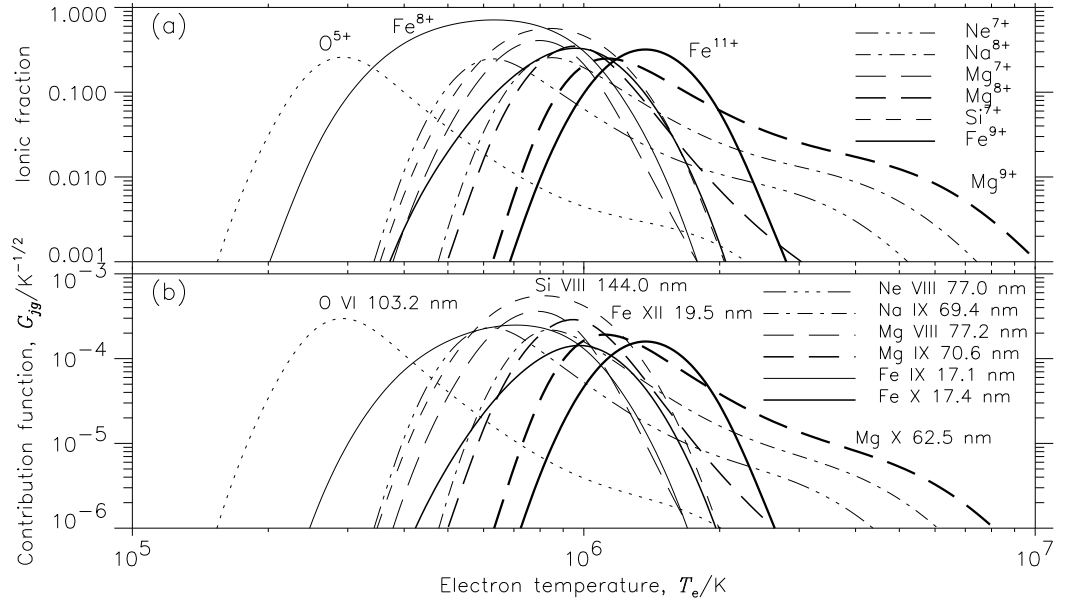

Figure 19: (a) Ionic fractions of some ions (treated in this review) in a plasma in ionization equilibrium as a function of the electron temperature (data from Mazzotta et al. 1998); (b) contribution functions (see Eq. 4) of spectral lines from these ions in optically thin plasmas. Note the long tails to high temperatures of the lithium-like ions O^{5+}, Ne^{7+}, Na^{8+} and Mg^{9+}.

to Fe XII emission, but are the result of two Fe VIII lines at 19.47 nm and 19.6 nm and other cooler iron lines (cf., Del Zanna and Bromage 1999; Del Zanna et al. 2003). By observing two or more spectral lines with different contribution functions and formation temperatures, more

Table 4: Typical electron temperatures in CHs, plumes and IPRs at some heights

Height, $h/R_\odot$	Temperature, T_e/MK			Method	Date	Reference
	CH[a]	PL	IPR[b]			
0.05	0.85			Mg X,	13 Dec 1973	Habbal
				Ne VII[c]		et al. 1993
0.00	1.00			DEM	25 Feb 1996	Mason
				(on disk)		et al. 1997
0.07	$0.8^{+0.07}_{-0.1}$			O VI 17.3 nm,	21 May 1996	David
0.18	$1.0^{+0.3}_{-0.2}$			103.2 nm	SOHO roll	et al. 1998
0.33	$0.4^{+0.6}_{-0.3}$			line ratio		
0.03		0.73	0.78	Mg IX	24 Jan 1997	Wilhelm
0.08		0.79	0.81	(70.6,75.0) nm	15 Nov 1996	et al. 1998
0.17		0.78	0.87	line ratio		
0.03			0.85	Si VIII/Si VII	Jul/Dec	Doschek
0.05			0.94	line ratio	1996	et al. 1998
0.00	0.76		≈ 0.82	Mg IX 36.8 nm	Aug/	Fludra
0.05	$0.82_{\pm0.2}$			Mg X 62.5 nm	Sep 1996	et al. 1999
0.11	0.85			line ratio		
0.00	2.00			BP at base,	25 Oct 1996	Young
0.035		$1.05_{\pm0.05}$	1.00	discretized		et al. 1999
0.085		$1.05_{\pm0.05}$	1.12	DEM		
0.00		$0.80_{\pm0.05}$		DEM	23 Aug 1996	Del Zanna and
				(on disk)		Bromage 1999
0.00	0.79			DEM	10/11 Oct	Del Zanna
				(on disk)	1997	et al. 2003
0.07		0.73	1.10	Mg IX	24 May 2005	Wilhelm
0.11		0.78	1.12	70.6 nm,		2006
0.19		0.69	1.17	75.0 nm		
0.03			$0.79^{+0.1}_{-0.08}$	EM	3 Nov 1996	Landi
0.10			$1.00^{+0.1}_{-0.09}$	DEM		2008
0.17			$1.07^{+0.13}_{-0.1}$			
0.3			1.16	Mg IX ratio	1996/1997	Del Zanna
						et al. 2008
0.06 (h_1)		0.77 (0.51)	1.50 (1.03)	Mg IX ratio	28/29 Mar	this work
0.15 (h_4)		0.96 (0.84)	1.50 (1.10)	tan. (con.)[d,e]	2006	
0.04 (h_1)		0.79 (0.72)	1.10 (0.99)	Mg IX ratio[f]	7/8 Apr	this work
0.13 (h_4)		0.84 (0.83)	1.06 (1.05)	tan. (con.)	2007	

[a] possibly affected by plume plasma

[b] below $h < 0.05\ R_\odot$ some plume projections seem to merge and could hide IPRs

[c] Ne VII (0.51 MK)

[d] Ratios: tangential – $\rho^{\mathrm{tan}}_{\mathrm{PL}}(h_1, h_4) = (6.52,\ 5.67)$; $\rho^{\mathrm{tan}}_{\mathrm{IPR}}(h_1, h_4) = (4.53,\ 4.54)$;
concentric – $\rho^{\mathrm{con}}_{\mathrm{PL}}(h_1, h_4) = (9.04,\ 6.14)$; $\rho^{\mathrm{con}}_{\mathrm{IPR}}(h_1, h_4) = (5.45,\ 5.16)$

[e] margins of correlation coefficients (3σ) given in Fig. 21

[f] Ratios: $\rho^{\mathrm{tan}}_{\mathrm{PL}}(h_1, h_4) = (6.61,\ 6.15)$; $\rho^{\mathrm{tan}}_{\mathrm{IPR}}(h_1, h_4) = (5.15,\ 5.29)$;
$\rho^{\mathrm{con}}_{\mathrm{PL}}(h_1, h_4) = (6.99,\ 6.38)$; $\rho^{\mathrm{con}}_{\mathrm{IPR}}(h_1, h_4) = (5.60,\ 5.33)$
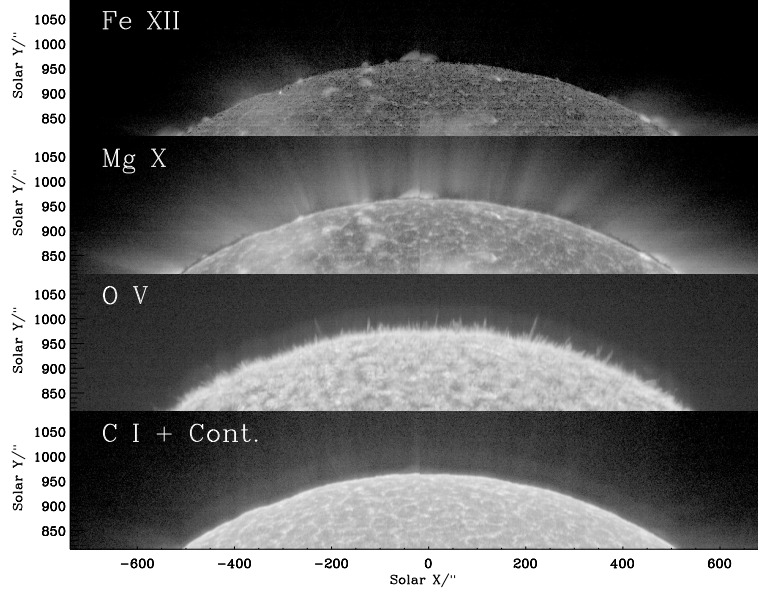
Figure 20: N polar region observed on 31 August / 1 September 1996 in four spectral lines: C I ($T_\mathrm{F} \leq 30\,000$ K; showing the chromospheric network in the bottom panel), O V with network, spicules and macrospicules at the limb, no plumes, Mg X showing CH, BPs and plumes, Fe XII with CH and BPs and no plumes. See Feldman et al. (2003) for further monochromatic CH images.

information on the electron temperature can be gained. A radiance ratio of the EIT bands 19.5 nm (Fe XII) and 17.1 nm (Fe IX, Fe X), for instance, clearly shows a CH temperature near 1 MK (Moses et al. 1997; Wilhelm et al. 2002b).

One of the methods to check whether the condition of thermal equilibrium is fulfilled is to compare the effective ion temperatures (cf., Sect. 5.2.2) with the electron temperature estimated from ionization equilibrium assumptions and to separate the ion thermal velocity (cf., Sect. 5.2.3) from the observed line width by using two emission lines of different atomic species (e.g., Seely et al. 1997; Imada et al. 2009).

Without strong temperature gradients along the LOS, an EM analysis utilizing many lines and their contribution functions provides a reliable electron temperature determination (cf., e.g., Landi 2008). If there are temperature gradients, a differential emission measure (DEM) procedure, where only the maxima of the contribution functions are considered, leads to an electron temperature estimate (cf., e.g., Del Zanna et al. 2003).

Finally, line-ratio investigations have to be mentioned (Flower and Nussbaumer 1975). The radiance ratio of two lines (preferably) from the same ion is temperature dependent, if the excitation energies are very different, e.g., O VI 17.3 nm, 103.2 nm, or, if one line is excited from a metastable level, e.g., in Mg^{8+}. CH temperature measurements using the O VI ratio have been reported by David et al. (1998), and plume as well as IPR results from the Mg IX ratio have been obtained by Wilhelm et al. (1998). In observing temperature-sensitive line ratios, complications similar to those for density-sensitive pairs arise (see Sect. 5.1), if the electron temperature along the LOS is not uniform. A plot of the radiances of the Mg IX 70.6 nm, 75.0 nm lines in Fig. 21 therefore exhibits the same characteristic features of the regression lines with a positive offset on the ordinate. The diagram allows us to estimate the
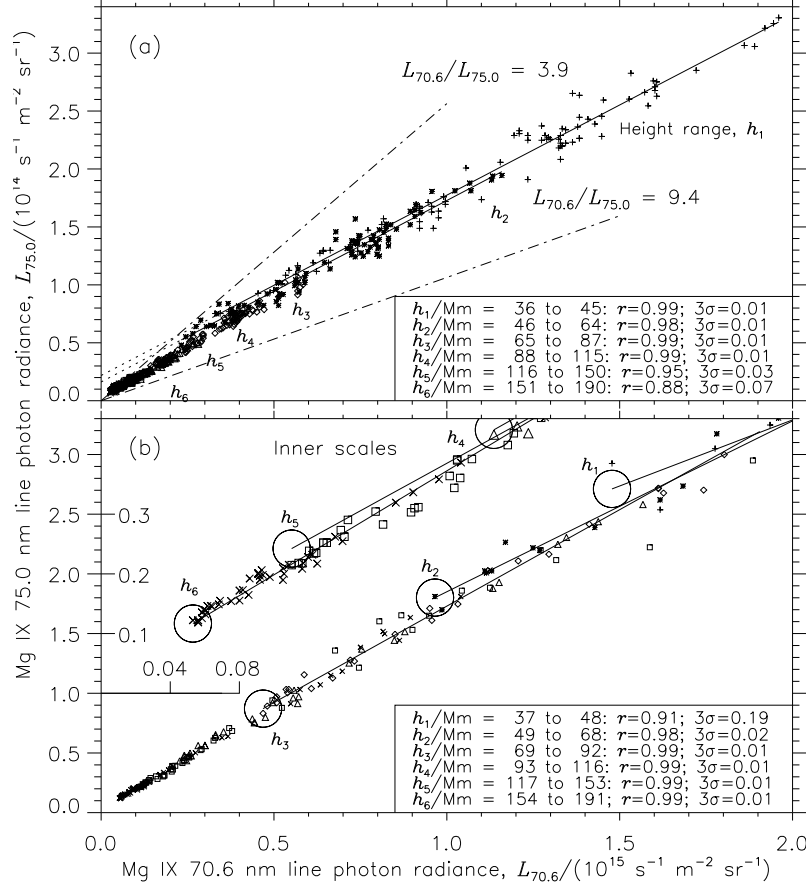
Figure 21: Radiance of the Mg IX 75.0 nm line as a function of the 70.6 nm radiance on 29 March 2006. The observations have been simultaneously obtained with the Si VIII data in Fig. 16, and are arranged in tangential heights in panel (a) and concentric ones in (b). The correlation results are given in the inset. The broken lines labelled $L_{70.6}/L_{75.0} = 9.4$ and 3.9 correspond to $T_e \approx 0.5$ MK and 2 MK, respectively. The lowest radiance values are encircled and taken as the best estimates for IPR conditions. The low-radiance portion is repeated in panel (b) enlarged by a factor of five with larger symbols and a shifted scale of the ordinate.

Mg IX ratios in plumes and IPRs in the various height ranges with a method in analogy to the density determination. However, the small variation of the slopes as a function of the relevant temperatures from 0.5 MK to 2 MK leads to relatively large uncertainties. The Mg IX data were recorded by SUMER in March 2006 simultaneously with the Si VIII observations in Fig. 16. The conversion of the measured ratios into temperatures requires atomic physics data. They were taken from Zhang et al. (1990) for the O^{5+} ion and from Keenan et al. (1984) for Mg^{8+}.

Recently, a re-calculation for the Be-like Mg^{8+} ion has been performed by Del Zanna et al. (2008) according to which the plume temperatures from the Mg IX ratio would increase by approximately 0.1 MK and the IPR values by ≈ 0.4 MK. From the table, in particular, if the revised Mg^{8+} data would be taken into account, it is clear that the electron temperature in plumes is lower than in IPRs except at very low heights near the base of a plume. These findings are in excellent agreement with theoretical considerations (cf., Wang 1994; see Sect. 8). They are also consistent with the so-called freeze-in temperatures determined from charge-state measurements of SW ions, namely 1.5 MK $\leq T_e \leq$ 1.6 MK in the height range 0.3 $R_\odot \leq h \leq$ 0.5 $R_\odot$ (Ko et al. 1997; cf., Fig. 18).

The results of later campaigns in 2007 and 2008 have not yet been analysed in detail, but judged from first assessments they are in agreement with the 2006 and also with the 2005 results. Some preliminary values for 2007 are included in Table 4. The LOS Si VIII and Mg IX ratios have been used to determine the electron densities and temperatures in Fig. 22 during the Hinode campaign in April 2007. The diagram clearly shows low temperatures along the plume projections and higher ones in IPRs.

Fig. 23 gives a sample Al_poly image, recorded by XRT on 1 July 2008 in the time interval from 20:54 to 21:11 UTC. Similar images have been obtained in the Al_mesh channel, allowing us to build maps of the Al_poly-over-Al_mesh radiance ratios in the FOV. They can be converted into temperature maps with the help of a calibration procedure (Golub et al. 2007). Dashed lines are drawn to guide the eye in the plume identification (the red lines indicate jets as explained in Sect. 6.3). A comparison between plumes seen both in the TRACE 17.1 nm bandpass and the ratio maps of XRT yields a one-to-one correspondence — at least for the best visible, high contrast, structures. This is not surprising, because the temperature response of this TRACE channel peaks at a temperature just below 1 MK and the XRT maps show plumes to be at a temperature close to (but probably lower than) 1 MK. The IPR plasma is slightly hotter than that of plumes, at least in the low corona. These results are consistent with those obtained with different instrumentation and methods given in Table 4. We conclude from this preliminary analysis that Hinode appears to offer valuable data to advance our knowledge on plume and IPR plasmas, and the association between plumes and jets (cf., Sect. 6.3).
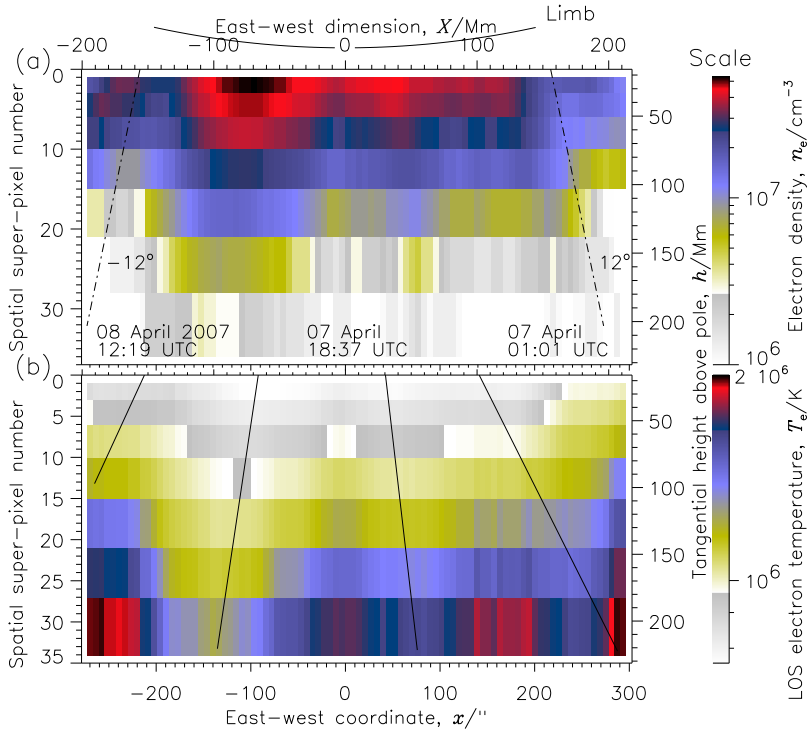

Figure 22: (a) Electron density map of the southern CH in April 2007 obtained from the Si VIII line ratios. (b) Electron temperatures simultaneously measured in the same FOV with the Mg IX line-ratio method. The weak line at 75.9 nm required combining detector pixels to super-pixels and averaging over relatively large height ranges. Some plume projections are indicated that could be identified in Fig. 25, where additional data are displayed at higher spatial resolution (from Wilhelm et al. 2010).

5.2.2 Line profiles and effective ion temperatures

First observations of broadenings of the Mg x 60.9 nm, 62.5 nm lines corresponding to velocities of $V_{1/e} = 45$ km s^{-1} at the base of the corona to ≈ 55 km s^{-1} at $h = 0.2\ R_\odot$ have been reported by Hassler et al. (1990) from a sounding rocket flight on 17 March 1988. The quantity $V_{1/e}$ is the speed at which the Doppler effect decreases the spectral radiance of a line profile to $1/e$ of the peak — it can be considered as the most-probable speed. The spectrometers on SOHO and Hinode can now measure the spectral profiles of many emission lines in the VUV wavelength range on the solar disk and in the corona out to several solar radii. The speed, $V_{1/e}$, called Doppler velocity here, is related to the Doppler width, $\Delta\lambda_\mathrm{D}$, and the effective temperature, T_eff, by

$$\Delta\lambda_\mathrm{D} = \frac{\lambda_0}{c_0}\, V_{1/e} \tag{5}$$

and

$$V_{1/e} = \sqrt{\frac{2\,k_\mathrm{B}\,T_\mathrm{eff}}{m_\mathrm{i}}} \quad, \tag{6}$$

where m_i is the ion mass, c_0 the speed of light in vacuum and λ_0 the rest wavelength of the spectral line. The Doppler widths[9] are of particular interest as they indicate temporally unresolved LOS motions of the emitters (atoms or ions; see the next section for more details).

As can be seen from the Table 5 and Fig. 24, the line widths are, in general, smaller in plumes than in IPRs. The relative decrease is $\approx 10\ \%$ to $20\ \%$ in many observations, but more pronounced variations also occurred. The scatter of the data points is rather large, but the trends confirm wider profiles in IPRs than in plumes. In accord with this result, the radiance of many emission lines were anti-correlated with the line widths during the SOHO roll manœuvre on 3 September 1997 between $h = 0.05\ R_\odot$ and $0.10\ R_\odot$ (Wilhelm and Bodmer 1998). The widths increase with height both in plumes and IPRs. Below $h = 0.1\ R_\odot$, it is

---

[9] For a Gaussian distribution, it is $\Delta\lambda_\mathrm{D} = \sigma\,\sqrt{2} = \Delta\lambda_\mathrm{FWHM}/(2\,\sqrt{\ln 2})$, where σ is the standard deviation.

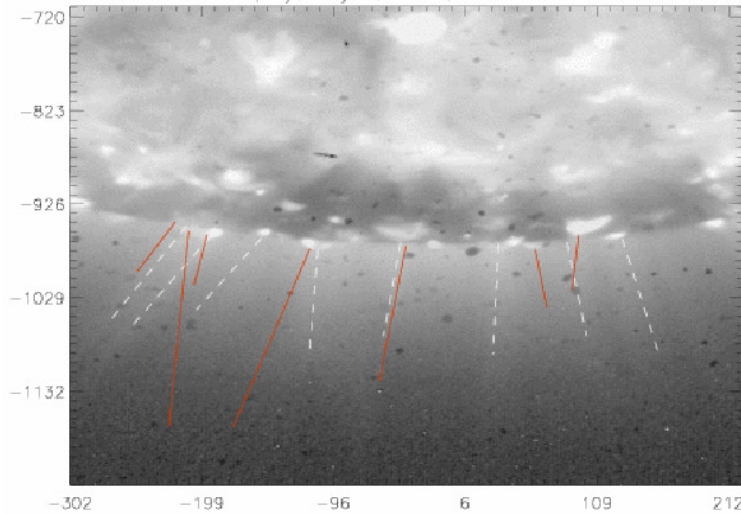Figure 23: XRT image with Al_poly filter on 1 July 2008. The white dashed lines are drawn to guide the eye in plume identification. Seven jets observed over a 3 h time interval are drawn as solid red lines. The scales are in seconds of arc from the centre of the solar disk. An association is apparent between plumes and jets.

Table 5: Widths of spectral lines in CHs, plumes and IPRs as LOS Doppler velocities, $V_{1/e}$

Height[a] $h/R_\odot$	Velocity, $V_{1/e}/(\mathrm{km\,s^{-1}})$ CH	PL	IPR	Method	Date, Period	Reference
0.50		120±4	150±8	O VI 103.2 nm	6 Apr 1996	Antonucci
1.00		220	270	line width		et al.
1.30		240	300			1997
0.02	42			Mg X	20 Jul 1996	Marsch
0.11	50			62.5 nm		et al.
0.16	57			line width[b]		1997
0.05		44±2	48±2	O VI 103.2 nm	22 May 1996	Hassler et al. 1997
0.50	90			O VI	3 Jun 1996	Kohl
1.00	250±25			line width		et al. 1998
0.03			36	Si VIII 144.6 nm	4 Nov 1996	Banerjee
0.12			46	line width[c]		et al.1998
0.06		48	56	O VI 103.8 nm	13 Mar 1996	Wilhelm 1998
0.05	39±3			Si VIII 144.6 nm	5 Nov 1996	Tu
0.18	63^{+4}_{-5}			line width[d]	3 Oct 1996	et al. 1998
0.03		56 (41)	53 (41)	Mg IX,	24 Jan 1997	Wilhelm
0.08		59(44)	50(45)	(Si VIII)		et al. 1998
0.17		60(47)	62(50)	line widths		
0.34		60±5	180±25	O VI 103.2 nm	Sep 1997	Kohl
0.94		60±10	380±30	line width		et al. 1999
0.35	186±22(104±6)			H I Ly α, (Mg X)	Aug/Sep	Esser
1.00	207±25(200±20)			line widths[e]	1997	et al. 1999
0.5	89(190)			O VI 103.2 nm,	Nov 1996/	Cranmer
1.0	310(220)			(H I Ly α)	Apr 1997	et al. 1999
1.5	420(240)			line widths		
0.72		167±10	182±15	O VI 103.2 nm line width[e]	6 Apr 1996	Giordano et al. 2000b
0.06		54±1	56±1	O VI 103.2 nm	3 Jun 1996	Banerjee
0.20		62±1	67±2	line width		et al. 2000a
0.28		69±1	75±2			
0.60	110			O VI 103.2 nm	Feb 2001	Miralles
1.40	340			line width		et al. 2001
1.85	429					
0.06		54	56	O VI 103.2 nm	3 Jun 1996	Teriaca
0.50		80	90	line width		et al. 2003
1.00		270±30	300±30			
1.50		360	400			
0.50		160±10	170±10	H I Ly α		
1.00		190±15	200±15	line width		

Continued on next page

---

[a] above the photosphere
[b] tendency of wider profiles in IPR
[c] $V_{1/e}$ calculated from non-thermal motion $\xi^{\mathrm{IPR}} = (27, 39)\ \mathrm{km\,s^{-1}}$ at h_1 and h_2 with $T_i = 1$ MK
[d] widths of other emission lines measured as well
[e] $V_{1/e}$ calculated from T_{eff}

Height[a]	Velocity, $V_{1/e}/(\mathrm{km\,s^{-1}})$			Method	Date,	Reference
$h/R_\odot$	CH	PL	IPR		Period	
0.05		≈ 35	59	Mg IX 70.6 nm	24 May 2005	Wilhelm 2006
0.08			66	line widths[f]		
0.13			69(48)	(Si VIII 144.6 nm)		
0.0		45	45	Empirical model[g]	1996	Raouafi et al. 2007b
0.5		50	125	O IV		
1.0		65	200			
1.5		110	220			
0.01		31 (33)	38 (37)	Fe XII 19.5 nm	10 Oct 2007	Banerjee et al. 2009a
0.03		33 (38)	39 (38)	(Fe XIII 20.2 nm)		
0.15		45 (45)	47 (49)	line widths[h]		

[f] results of a comparison of observations with a forward model calculation
[g] the model yields $V_{1/e}^{\mathrm{PL}} \approx V_{1/e}^{\mathrm{IPR}}$ for $h > 3\ R_\odot$
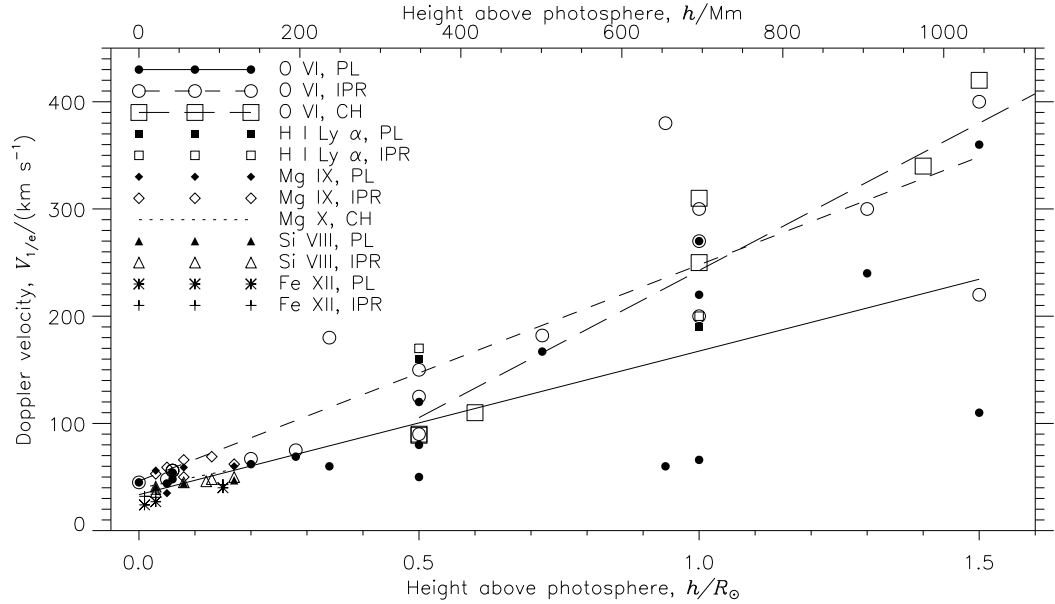[h] $V_{1/e}$ calculated from non-thermal motions with $T_\mathrm{i} = T_\mathrm{F}$

Figure 24: Doppler velocities of prominent coronal emission lines in plumes, IPRs and CHs in general. Linear regression lines are given for four groups of data points (O VI: PL, IPR, CH; Mg X: CH). At low altitudes, $V_{1/e}$ is relatively constant near 50 km s^{-1}, but with a positive slope.

sometimes difficult to find pure lane conditions as contamination by plume material might occur. When only CH data are available, they seem to reflect the IPR widths. High-spatial-resolution observations of the UV emission of a CH from $R = 1.45\ R_\odot$ to $2.05\ R_\odot$ at solar

minimum were performed with UVCS over an interval of 72 h. In the O VI 103.2 nm radiance map reconstructed from spectral data, four plumes can be identified as bright features (Fig. 1 of Giordano et al. 2000b). The line width in these plumes were narrower than in the IPRs.

A detailed study of coronal emission line profiles using UVCS observations indicated some deviations from a Gaussian shape near the peak of many coronal lines (Kohl et al. 1999). The H I Ly α line, however, can be approximated rather well by a Gaussian profile at all heights, whereas the O VI profiles are more complex: at low altitudes (below $h \approx 0.35~R_\odot$) they are nearly Gaussians, but more pronounced deviations occur at greater heights. The O VI profiles can be represented there by narrow and broad components. The latter appears to be associated with low-density IPRs, and the former with denser plumes along the LOS. They are mainly observed at the centre of the line close to the rest wavelength, so that no significant Doppler shifts are observed for these plume contributions. The width of the narrow component hardly changes with height. Beyond $R = 2.5~R_\odot$, the line profiles are formed only by the broad component, and the narrow component is no longer observed.

For SUMER observations from low altitudes, the separation of a narrow plume line profile from a somewhat wider IPR contribution is not easy. In a forward calculation, the observed line widths in Mg IX 70.6 nm could be reproduced under the assumption of a constant $V_{1/e} = 35$ km s^{-1} over a height range from 0.05 $R_\odot$ to 0.13 $R_\odot$ and the IPR widths nearly twice as wide (see Table 5). This result would explain the observations by Doschek et al. (2001) indicating line-width increases with height for Si VIII 144.6 nm on 3 May 1996 and no effect for several ions on 3 November 1996, if the SUMER slit was aligned with an IPR in May and with a plume in November. It should be mentioned here that Banerjee et al. (2000a) and Xia et al. (2004) found wider O VI line widths in plumes (or near their footpoints) than in darker regions on the disk. We also have to note that the $V_{1/e}$ speeds of O^{5+} ions are much higher than those of Si^{7+} in IPR (Banerjee et al. 2000a), and that magnesium ions have higher speeds than hydrogen (Esser et al. 1999) or Si^{7+} (Wilhelm et al. 1998; Wilhelm 2006). Finally, O^{5+} exhibits about twice the difference in $V_{1/e}$ between plumes and IPR than hydrogen at $h \approx 0.5~R_\odot$ to 1 $R_\odot$ (Giordano et al. 1997).

5.2.3 Ion temperatures and non-thermal motions

The Doppler width, $\Delta\lambda_D$, of an emission line is caused by the thermal motions along the LOS of the atom or ion under study and the non-thermal contributions, which are either turbulence or temporally unresolved waves. We can thus write

$$\Delta\lambda_\mathrm{D} = \frac{\lambda_0}{c_0} \sqrt{\frac{2\,k_\mathrm{B}\,T_\mathrm{i}}{m_\mathrm{i}} + \xi^2} \quad , \tag{7}$$

where T_i is the ion temperature and ξ the non-thermal speed (cf., Mariska 1992).

Under the assumption of $T_\mathrm{i} = 1$ MK for Si^{7+} ions, Banerjee et al. (1998) derived non-thermal motions of 27 km s^{-1} at 0.03 $R_\odot$ above the limb in PCHs and 46 km s^{-1} at 0.26 $R_\odot$. Both values were obtained in IPR. An ion temperature of 2 MK did not lead to a consistent result. Hassler et al. (1997) and Banerjee et al. (2000a) put forward the hypothesis that the ion temperatures in plumes and IPRs are not very different, but that higher non-thermal motions are present in IPRs.

The non-thermal speed is related to the wave amplitude by $\xi^2 = \langle \delta v^2 \rangle / \zeta$ (with $\zeta \approx 2$ depending on the polarization and LOS), if waves are responsible for this contribution (cf., e.g., Hassler et al. 1990). Variations of ξ as function of height above the limb have been calculated from EIS observations in the lines Fe XII 19.5 nm and Fe XIII 20.2 nm (Banerjee et al. 2009a). Since the separation of $V_{1/e}$ into T_i and ξ is not a straightforward procedure — as discussed in detail by Dolla and Solomon (2008) — we include in Table 5 only LOS Doppler velocities directly derived from line-width measurements or calculated from ξ and T_i data in the literature.

5.3 Elemental abundances and first ionization potentials

The composition of the solar photosphere can, with the exception of the noble gases, be directly determined from spectroscopic observations (cf., Grevesse and Sauval 1998). In the corona, attempts to measure the helium abundance have been made by Gabriel et al. (1986) and Laming and Feldman (2001); for argon and neon abundances see Phillips et al. (2003) and Landi et al. (2007). Methods of measuring the solar and coronal abundances of an element X have been reviewed by von Steiger et al. (2001). In the corona, the abundance of elements is varying and the so-called FIP effect seems to play a dominant rôle. Elements with a FIP of $I_X < 10$ eV are defined as low-FIP elements and those with FIP of $I_X > 10$ eV as high-FIP elements, separated by the photon energy $h\nu = 10$ eV of the H I Ly α line. The low-FIP elements are — with respect to photospheric values — overabundant in the (equatorial) corona by a factor of about four to five relative to the high-FIP elements (cf., Widing et al. 2005). The magnesium/neon abundance ratio in plumes is enhanced relative to IPRs by a factor of 1.5 (Young et al. 1999) to 1.7 at $h = 0.05$ $R_\odot$ and 3.5 at 0.1 $R_\odot$ (Wilhelm and Bodmer 1998). These abundance determinations depend on the electron temperatures employed, and might have to be re-evaluated should better temperature data become available. According to Feldman et al. (1998), there was no significant FIP effect observed at $h = 0.03$ $R_\odot$ above the northern solar limb on 3 November 1996; these data were taken by SUMER in an IPR of a CH (cf., Landi 2008). If the IPRs are indeed the source regions of the fast SW, no composition changes would be expected in the high-speed streams in accordance with observations, except probably for helium with its long first ionization time (FIT) (Geiss et al. 1995).

Observations of the Ne VIII 77.0 nm and Mg VIII 77.2 nm lines in April 2007 during the most recent solar minimum showed a very clear plume/IPR structure in a map of the radiance ratio $L_{77.0}/L_{77.2}$ (Curdt et al. 2008), which is repeated in Fig. 25(a). Any doubt that this effect is caused by the high-temperature tail of the lithium-like Ne VIII contribution function (see Fig. 19) can be dispelled by inspecting Fig. 25(b) and (d) showing radiance ratios of the Ne VIII line with the Mg IX and Na IX 69.4 nm (0.85 MK) lines.[10] Although these lines have different contribution functions compared to Mg VIII, the plume/IPR patterns are basically the same. In particular, as the contribution function of Na IX is always larger than that of Ne VIII above 0.8 MK, it must be concluded that a FIP effect in plumes operates with an enhancement of the magnesium abundance by a factor of 1.5 to 2 relative to neon, and that the relative abundance of the low-FIP element sodium is enhanced as well. A verification that there are higher electron temperatures in IPRs than in plumes follows from Fig. 25(e) displaying the $L(\text{Si VIII})/L(\text{Si IX})$ radiance ratio.

---

[10]Temperature effects, however, cause the high Ne VIII/Mg IX and Ne VIII/Na IX ratios at low altitudes in panels (b) and (d), and the increase of the Ne VIII/Mg VIII ratio in panel (a) above 120 Mm in the hot IPRs.
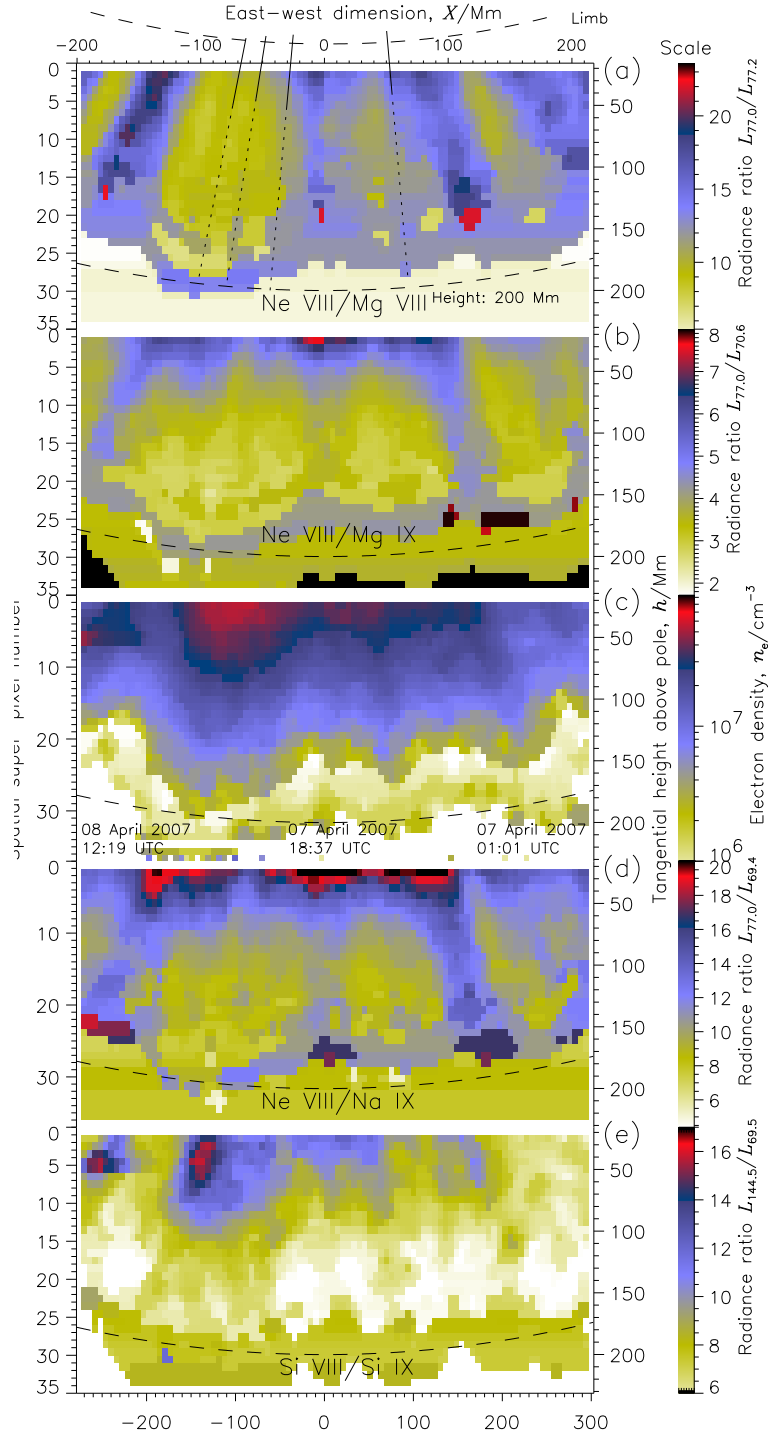
Figure 25: Ratios of photon radiances for several spectral lines as indicated in the panels (a), (b), (d) and (e). The maps obtained in one raster scan of 96 steps from right to left with SUMER show the same region of the southern CH in April 2007. From the limb on top of the figure, some projections of plume reconstructions from EUVI stereoscopic observations are indicated continuing into panel (a) (cf., Curdt et al. 2008). The electron densities in panel (c) are converted from the LOS Si VIII 144.6 nm, 144.0 nm ratios. Beyond $\approx$ 150 Mm altitude, the maps are unreliable, because of noise contributions from the weaker lines of the pairs.

Widing and Feldman (2001) found in active regions (AR) that the confinement time of a plasma is a decisive parameter for abundance variations. A FIP bias of nearly ten was reached after ≈ 6 d. If these findings can be applied to plumes, we would expect confinement times of a day or so — not too different from plume and BP lifetimes.

6 Relations of plumes to other solar phenomena

Coronal plumes are rooted in the lower layers of the solar atmosphere. It is essential to identify the relationship with features in these regions: – What is the association of plumes with the magnetic network of the Sun? – What is the relationship between plumes and coronal BP? – Are magnetic field configurations, called "rosettes", around plumes necessary for their formation and/or existence? – Is there any signature of plumes expected in the Heliosphere?

6.1 Chromospheric network

The reconnection processes in the complex magnetic network that are thought to be required for the generation and acceleration of the SW have been described as microflares by Axford and McKenzie (1992). The fine structure of the network is of particular importance for the physics of CH. Based on imaging results and the element composition of TR plasmas, Feldman et al. (2001) concluded that it is likely that this plasma is confined in magnetic structures and has no direct interface with the chromosphere.

High-frequency Alfvén waves produced in the network have been discussed by Marsch and Tu (1997) in a SW acceleration and coronal heating model. In addition to a steady coronal-funnel flow, solutions have been found with a standing shock at a height of $h \approx 8$ Mm. High densities and low outflow speeds are characteristic for the plasma above the shock and might indicate plume conditions. Such a process could operate at some stage of plume formation, however, the higher electron and proton temperatures relative to the unshocked case are in agreement with observations only, if an inversion occurs at greater heights (cf., Sect. 5.2.1). Shock formation of slow magnetosonic waves in plumes is discussed by Cuntz and Suess (2001), who showed that it is expected to take place below $h = 0.3\ R_\odot$. Numerical simulations show that the shock formation can be suppressed, or can occur considerably higher when realistic compressive viscosity is taken into account for slow magnetosonic waves with observed amplitudes and periods (Ofman et al. 1999).

The relation of the chromospheric network to plumes has already been mentioned in Sects. 3 and 4. Here we want to call attention to some compressional wave observations in the lower solar atmosphere with dominant periods of 25 min and an occasional downward direction in inter-network regions, whereas only upward propagations prevailed within the network (Gupta et al. 2009). Evidence of downward propagating waves in the TR had earlier been reported by Judge et al. (1998).

In Sect. 3, it has been outlined that coronal plumes arise from footpoints 2 Mm to 4 Mm wide in the network and expand rapidly with height to diameters of 30 Mm (see Fig. 4). Plumes are associated with magnetic flux concentrations in the super-granular network boundaries. Note in this context that the typical size of a super-granule agrees with the typical diameter of *beam* plumes at the base of the corona. However, not all of the flux concentrations give rise

to coronal plumes. The plume footpoints are, in general, magnetically rather complex — often related to BPs (see next section) and rosettes (cf., Sect. 3.1). Plumes are thought to result from heating processes taking place when unipolar magnetic flux concentrations reconnect with oppositely directed fields of ephemeral emergent loops (cf., e.g., Wang 1994; Wang and Sheeley 1995). This scenario finds support in the high temperatures observed at the footpoints of plumes yielding high-pressure plasma that can diffuse along the magnetic field lines (van de Hulst 1950b).

6.2 Bright points

The association of coronal BP with plumes is particularly intriguing, because all possible combinations have been found: plumes with BPs at their base, plumes without BPs and BPs without plumes. Following a suggestion of Del Zanna et al. (2003), we will assume that BPs are typical features near plume footpoints only in the early phases of plume formation. At that stage, high temperatures have been observed at the base of plumes (see Sect. 5.2.1), whereas in a later phase — without BP — temperatures of less than 1 MK prevail at all heights. BPs without plume, on the other hand, have probably to be considered as precursors of plume formation. Doppler velocity observations of BPs also gave complex results: blue and red shifts of several kilometers per second or no shift are reported (Wilhelm et al. 2000; Madjarska et al. 2003; Popescu et al. 2004). The different findings might not only be related to the stages of evolution of the BPs, but also to differences in the formation temperatures of the emission lines used in the studies.

As another observational fact it should be mentioned that compact 17 GHz radio enhancements have been found with the Nobeyama Radioheliograph at the footpoint of a plume with BP (characterized by Fe XII emission), but not in the plume structure above the base (Moran et al. 2001).

6.3 Spicules, macrospicules and jets

The mass supply to the corona and the SW — estimated to be 1 % of the spicular mass flux by Pneuman and Kopp (1978) — poses a problem, because all TR studies (e.g., Doschek et al. 1976; Dere et al. 1989; Brekke et al. 1997; Chae et al. 1998) demonstrated strong red shifts of spectral lines and thus downflows of material, whereas the spectroscopic signatures of outflows in spicules were only present in blue wings of spectral lines, for instance, of N V 124.3 nm, indicating maximum LOS velocities of 150 km s^{-1} without significant shift of the main profile (Wilhelm 2000). Such profiles have also been observed with SUMER in other spectral lines (De Pontieu et al. 2009), and near footpoints of AR loops with EIS in Fe XIV 27.4 nm (Hara et al. 2008). Spicules seen in VUV emission lines with formation temperatures between $T_F = 30\,000$ K and 0.6 MK have larger diameters at higher temperatures — interpreted as a signature of evaporation (Budnik et al. 1998). A direct relationship between spicule activity and plumes could not be established (see also Fig. 20).

The relation between jets and plumes is not clear at this stage. From the rapid density decrease with height, van de Hulst (1950b) concluded that ejected plasma could not produce polar rays (as he called plumes). A fast jet with a speed of 400 km s^{-1} in a plume assembly displayed distinctly different characteristics from the surrounding plumes (Moses et al. 1997).
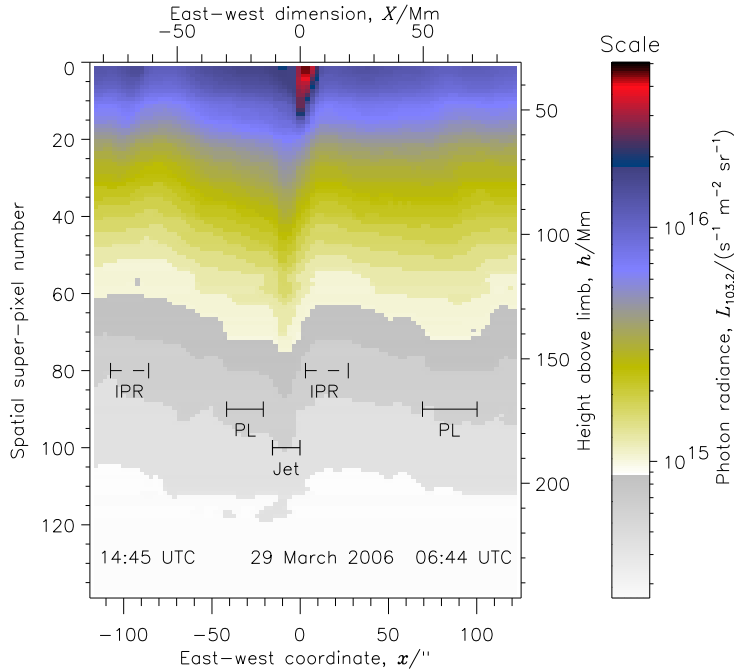
Figure 26: A jet seen in the southern CH on 29 March 2006 during the total eclipse campaign embedded in plume and IPR structures. The jet was recorded in O VI line at 103.2 nm and 103.8 nm (not shown) between 10:26 and 11:23 UTC. The ratio $L(103.2 \text{ nm})/L(103.8 \text{ nm})$ was 2.3 in the centre of the jet at 70 Mm height, just left of it in plume plasma the value was 2.35 and 2.4 to the right in an IPR. The same event is shown in Fig 2 as green rectangle. A super-pixel is equivalent to two detector pixels for this strong line.

Similar observations of a jet related, in addition, to a macrospicule obtained during a multi-spacecraft campaign in November 2007 are reported by Kamio et al. (2010). Lites et al. (1999) described a narrow jet embedded in a wider plume from WL and EUV observations during the 1998 eclipse. The outward propagation speed was $\approx 200 \text{ km s}^{-1}$. The acceleration of material is favoured over a wave perturbation scenario in this case. The acceleration could possibly be caused by explosive reconnection events (cf., Dere et al. 1991; Innes et al. 1997). Explosive events observed in chromospheric and TR lines did not show any detectable signature in the coronal Mg X 62.5 nm line (Teriaca et al. 2002; Doyle et al. 2004). However, the latter authors report their detection in the TRACE 17.1 nm channel. Thus a direct generation of the coronal plasma by the explosive event can be excluded; however, an indirect process must operate in order to heat the plasma.

Correlated observations of EUV and WL jets with EIT and LASCO near the limb and at several solar radii showed that the bulk of the material travelled with a speed of $\approx 250 \text{ km s}^{-1}$ much lower than the injection speeds (Wang et al. 1998). The jets originated near BPs and, in many cases, in the vicinity of plumes. Detailed studies of six polar jets observed in H I Ly α and O VI by UVCS (some of them also seen by LASCO and EIT) indicated a relative decrease in line width during the jet brightenings comparable to the plume/IPR ratio (Dobrzycka et al. 2002). A pronounced plume-like brightening was observed in the northern CH during the total eclipse on 29 March 2006 from five different sites (Pasachoff et al. 2008). It was therefore possible to determine an outward propagation speed of $\approx 65 \text{ km s}^{-1}$ in the height range from $h = 0.07 \ R_\odot$ to $0.27 \ R_\odot$. Based on the available data, the authors could not decide whether the brightening was of a wave-like nature or a material jet. More or less simultaneously, a jet was observed in the southern CH by SUMER in the O VI 103.2 nm, 103.8 nm lines. It is shown in Fig. 26 together with plumes in the neighbourhood of the jet,

which has a significantly different structure.

From XRT and EUVI observations in April 2007, Raouafi et al. (2008) found evidence that jets are precursors of coronal plume formation. An example of a jet observed by EUVI aboard STEREO A is recorded in Fig. 27 over a time period of 20 min showing in four images the transformation of a bright jet into plume haze interpreted as material on newly opened field lines. The base-heating model for plumes (Wang 1994) was applied to short-lived burst to generate the jets in this model. The association of plumes and jets is confirmed by the preliminary results of the Hinode campaign in summer 2008, where we found seven jets over a time interval of ≈ 3 h. They lasted from 4 min to 17 min, and most of them were seen in regions with prominent plumes. Fig. 23 shows the seven jets indicated as solid red lines in the XRT Al_poly image of a CH (see Sect. 5.2.1).

Twelve jets where detected during the 66 h LASCO-C2 observations in the right panel of Fig. 11. These features correspond to those jets-like structures seen by St Cyr et al. (1997) above the polar regions and analysed by Wang et al. (1998). The conclusion was that the WL polar jets last for ≈ 2 h in the C2 FOV, their occurrence frequency is three to four per day with an angular width (measured with respect to their non-radial axis) of 2º to 4º; in agreement with the parameters deduced from the TID in Fig. 9. The super-radial expansion factor of ≈ 2.2 reduces the angular width to 1º at the base of the corona (see DeForest et al. 2001b). Recurrent WL polar jets reported by Wang et al. (1998) look like transient events distinct from the quiescent emission of WL polar plumes. The main argument is the specific angular width and lifetime of these events. Some authors (e.g., Raouafi et al. 2008) found evidence that jets are precursors of coronal plume formation. An TID analysis showed that jets observed by LASCO-C2 in WL agree in duration, width and occurrence frequency with those seen in the VUV by EIT and UVCS (Llebaria et al. 2002b). Nearly all of the jets in WL appear to be associated with bright plumes (at least in the projection plane of view).

6.4 Fast solar wind and the Heliosphere

The source region of the fast SW streams has to be sought in CHs (see Sect. 3.1). It is also firmly established that funnel-type magnetic structures in the low corona exist, in which the acceleration of the SW must occur. It appears as if such structures are the building blocks for both IPRs and plumes. In the context of this section, the main questions are where the fast SW is produced and what signatures of the generation process might be found in the Heliosphere. The discussion in Sect. 4.3 points to IPRs as the main source region of the fast SW streams considering that the outflow speeds of IPRs are approximately a factor of two higher than in plumes at a height of $h \approx 1 \ R_\odot$. The higher densities in plumes might well be more than compensated by the low filling factor of plumes in CHs (cf., Sects. 3.1 and 5.1).

The strongest plume structures could be traced in the outer corona beyond 0.1 ua (see Sect. 3.1). If we were able to identify plumes in the interplanetary medium, the problem might unambiguously be solved whether or not they are relevant as contributors to the fast SW. Hence, can we look at in situ data to ascertain that plumes maintain their identity far out in the SW? Fine structures in He^{2+}/H^+ density ratios and flow speeds were observed in fast SW streams between 0.3 ua and 1.0 ua on Helios (Thieme et al. 1990), suggesting that the "ray-like structures" seen in CHs expand while retaining an overall pressure balance with the background. These structures — characterized by an anticorrelation between
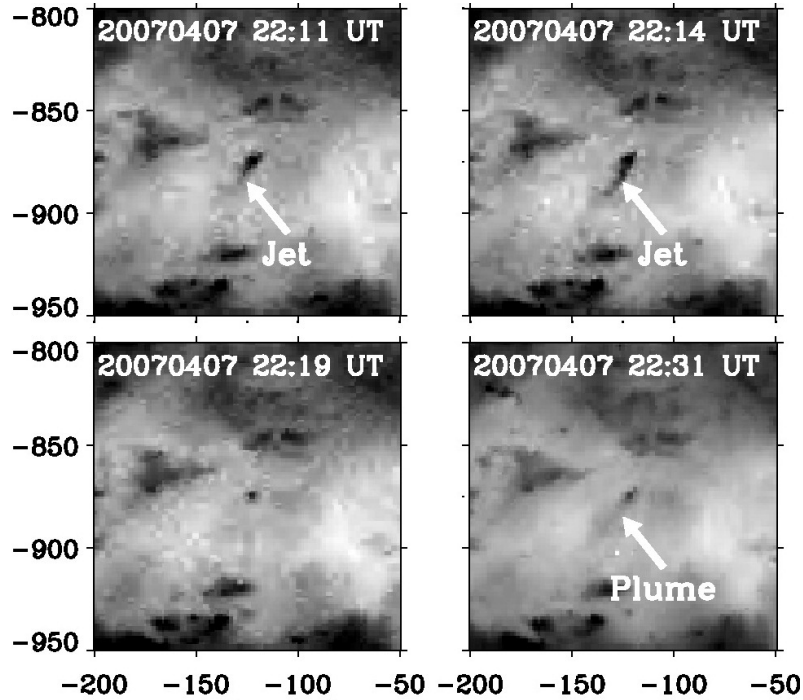
Figure 27: Observations made by EUVI on STEREO A in the 17.1 nm passband on 7 April 2007 illustrating a jet seen in the negative prints. Its evolution into a coronal plume occurred within 15 min. The x and y coordinate scales are in seconds of arc from the centre of the solar disk (from Raouafi et al. 2008).

gas and magnetic pressure — could possibly correspond to the interplanetary manifestation of plumes. The flow tubes were traceable at different heliocentric distances, because the two Helios probes were radially aligned at that time, and the same plasma parcel could be recognized in the data from both spacecraft. The flow tubes were becoming more and more difficult to identify, as larger heliocentric distances were reached. Stream interactions might have eliminated the speed signatures inside 1 ua in the ecliptic plane. At high latitudes this effect could happen at larger distances, and SWOOPS might be able to detect such signals. These structures have come to be known as PBSs. In their modeling attempts, Velli et al. (1994) pursued the idea that plumes expand into the SW under the assumption that they are hotter and more dense. However, as demonstrated in Sects. 5.1 and 5.2, these assumptions could not be verified by observations. Following the Helios result a series of papers dealt with the problem of plume identification in the distant SW, but controversial results have been obtained, for instance, by Yamauchi et al. (2002, 2004) on the basis of Ulysses magnetometer data.

A different approach was taken by Reisenfeld et al. (1999) who examined the correlations between the variations and magnitudes of plasma β and the α-to-p ratio within PBSs in Ulysses high-latitude data. Since the element composition (cf., Sect. 5.3) is a robust plasma parameter during the SW expansion, the authors concluded that at least the fraction of PBSs with relatively high β were indeed of solar origin, and tentatively related them to coronal plumes. The conceptual process foresees an expansion of the high-pressure plume structures at an altitude where the low-β regime ends. Based on a high α-to-p ratio in plumes, a positive correlation between this ratio and β is then expected in, agreement with the observations. However, the assumption of such a high ratio is, in all likelihood, not justified. The most

distinct plume/IPR signature is the low neon-to-magnesium ratio in plumes (see Sect. 5.3). The FIP of helium is even higher than that of neon and, consequently, a very low helium abundance relative to low-FIP elements must be expected in plumes (cf., also Wang 1996). Although the physics of helium and its ions in the solar atmosphere is not fully understood, it should be pointed out that helium is indeed less abundant than neon relative to low-FIP elements in the SW (Geiss et al. 1995).

In order to explain the Ulysses observations, only a slight modification of the assumptions is required: plume plasma, although on open field lines, will not become part of the SW, at least not in great quantities. Plume flux tubes would then be more or less void of plasma at large distances from the Sun. Therefore, the IPRs, the regions with higher plasma pressure, will expand when β increases, and have, of course, a higher He^{2+} abundance relative to H^0. In Fig. 5 of Reisenfeld and co-workers, the plume and IPR assignments just have to be reversed, and the lower portions of the newly defined plumes filled with dense plasma. Figs. 1 and 2 of Thieme et al. (1990) contain some examples of PBSs measured near 0.63 ua at times (42.0, 43.4, 44.0) d with relatively low β, α-to-p density ratio and proton temperature as well as relatively high magnetic fields that might qualify for remnants of a plume structures.

PBS have not been the only structures considered as possible candidates of plume remnants. Microstreams — small features identified in Ulysses data by a typical velocity profile — have been analysed by Neugebauer et al. (1995), who concluded that these were not to be identified with plumes. The same result was reached by von Steiger et al. (1999), because no significant depletion of the Ne/Mg abundance and charge-state deviation in these structures could be detected with respect to the surrounding fast SW.

Altogether, we may summarize that there is no clear indication for the presence of plume plasma in the SW (see, e.g., Poletto et al. 1996; DeForest et al. 2001a). Its disappearance beyond 30 $R_\odot$ must be ascribed to some interactions with the plasma in the IPRs. It has been suggested, for instance, that the differential flow speed between plumes and IPRs will lead to a Kelvin–Helmholtz instability that mixes the plume with IPR plasmas, removing the speed difference beyond ≈ 10 $R_\odot$ (Hardee and Clark 1995; Parhi et al. 1999). Alternatively, the shear could have been reduced below these heights, as implied by the decreasing density contrast illustrated in Fig. 17, due to some other interaction (Suess 2000). Plume signatures in temperature, composition and ionization state may still exist unless there is an actual mixing of plasma and magnetic field lines — something otherwise not expected to occur in the fast SW.

Before concluding this section, a possible link between plumes and the heliospheric current sheet should be mentioned as envisaged by Veselovsky and Panassenko (2000). With an analytical model of the global magnetic configuration in the heliosphere, and by superimposing a multi-polar geometry onto an equatorial current sheet, they argue that the shape and physical conditions of plumes are dictated not only by local conditions, but also by the global solar and heliospheric scenario.

6.5 Density and magnetic-field fluctuations

In situ data revealed the presence of interplanetary density and magnetic-field fluctuations whose power spectra have, over some restricted range of frequencies, a $1/f$ shape (see, e.g.,

Matthaeus and Goldstein 1986). This had long been known; however, photospheric high-latitude magnetic field spectra from MDI have recently been shown to display the same feature (see Matthaeus et al. 2007). Bemporad et al. (2008) have analysed coronal Ly α radiance fluctuations (that might be considered as a proxy for density fluctuations) in UVCS data taken above a PCH at about 2 $R_\odot$ and came to the conclusion that coronal high-latitude power spectra show the $1/f$ shape over about the same frequency interval where it was detected in interplanetary data. These results appear to imply that the 1/f noise persists throughout the solar atmosphere. The origin of this phenomenon and its interpretation are not clear yet, but a possible explanation invokes a cascade of scale-invariant reconnection processes, originating somewhere in the solar atmosphere, which transfer energy from smaller to larger scales and eventually show up in the $1/f$ spectrum. Since plumes can be identified by UVCS in the Ly α line (see, e.g., Kohl et al. 1997), it might be possible to check whether the $1/f$ spectrum is ubiquitous over the CH by analysing Ly α fluctuations in plumes, and disentangle the plume from the IPR spectrum, possibly showing they are different. Should plumes be the source of SW, or should the SW originate from both plumes and IPRs, we might expect the spectrum of plume density fluctuations to be similar to the in situ spectra.

There are problems in implementing such a project, because we need to follow a plume for a long enough time to be able to build up its spectrum, but the LOS contribution from the IPR may mask any effect. On the other hand, should we find different spectra, we might confirm the different nature of the plume versus IPR plasmas. This could provide a further means of checking the persistence of plume structures in the interplanetary medium, if in situ spectra at different heliocentric distances would become available, thus adding a further feature to those adopted so far in this investigation (see Sect. 6.4).

On the other hand, if the plumes and observations do not cooperate in giving enough exposure time to get very low-frequency spectra, it might be feasible to look at intermediate wave numbers and frequencies to form a kind of k-ω-diagram (i.e., wave-number-frequency relation) over a modest range of scales and periods. This could help distinguish whether the space-time structure of plumes is more like wave with linear propagation, or some kind of non-linear effect, such as turbulence or cascades.

7 Classification

Taking all the existing observations into account, it should be possible to agree on a plume nomenclature and answer the questions: – Is there more than one type of plume? – How are polar rays and jets related to plumes? – Are polar plumes in PCHs comparable to coronal plumes in non-polar CHs?

The terminology related to our phenomenon has changed over the years: "polar rays" and "brush-like plumes" (van de Hulst 1950b); "Polarstrahlen" (Waldmeier 1955); "polar rays" (Saito 1965a); "coronal polar plumes" (Newkirk and Harvey 1968); "polar plumes" (Ahmad and Withbroe 1977; Wang 1994) and "polar rays" (Koutchmy 1994). There can be little doubt that all names are related to the same phenomenon: field-aligned plasma density enhancements in the low and extended solar corona. These enhancements can either be detected via Thomson scattering of WL by electrons or via VUV emission lines from atoms and ions. In the range from $R = 1\ R_\odot$ to $R = 8\ R_\odot$ mainly considered in this report, the density enhancements deduced with the help of both observational methods yield comparable

results (see Table 3 and Fig. 17). We call them "polar coronal plumes". "Coronal plumes" have a wider meaning and include plumes from non-polar CHs. In VUV spectroheliograms polar coronal plumes appear as short spikes near the polar limb. DeForest et al. (2001a) have claimed that individual high-altitude WL structures can be traced to root structures in PCHs.

Although often difficult to detect outside the polar regions because of the presence of bright foreground and background material, plumes have been observed in low-latitude CHs (Wang and Muglach 2008). These low-latitude plumes appear to be completely analogous to their polar counterparts, overlying regions of mixed polarity within the predominantly unipolar CH and having characteristic lifetimes on the order of a day.

Diffuse, plume-like structures are also seen above small active regions that happen to emerge inside CHs. On even larger spatial scales, WL streamers that separate CHs of the same polarity might be regarded as giant plumes; such "pseudostreamers" overlie double arcades rooted in photospheric flux of the opposite polarity and extend outwards into the heliosphere in the form of plasma sheets without polarity reversals (Wang et al. 2007a, b). When the axis of the double arcade is oriented perpendicular to the solar limb, the pseudostreamer plasma sheet is seen edge-on and appears as a bright, narrow stalk; when the axis is parallel to the limb, a fan-like structure is observed. In contrast, ordinary coronal plumes more often have a cylindrical geometry, since the underlying minority-polarity flux is generally concentrated within a very small area. Examples of the different kinds of plume-like structures are displayed in Fig. 28.

According to Gabriel et al. (2009), there are at least two different structures masquerading to give a similar 2D appearance. The first is a beam plume; a quasi cylindrical structure overlaying a photospheric bipolar loop or group of loops (cf., Sect. 3.2). The second structure has been called network plume. These represent a very faint enhancement in the corona (in volume luminosity) overlaying the network boundaries. Its brightness becomes comparable to beam plumes only due to a large LOS integration. It is likely that the network plumes are in reality made up of many beam plumes, on a *much* smaller scale below the resolution limit of the imagers. An individual microplume (cf., Sect. 3) appears fainter due to the dilution by the normal coronal medium within a pixel of the detector.

8 Plume models and generation processes

The most important topic is, of course, how coronal or, in the restricted sense, polar plumes are generated and maintained in the corona: – Plumes are ubiquitous in CHs, but not in quiet-Sun areas. Can suitable constraints be defined and an agreement on the plume generation process be reached? – Can forward modeling create plume structures in CHs?

8.1 Plume formation and decay

The elevated densities in plumes can be explained if a strong heating source is present near their bases (Wang 1994). As plumes are found to overlie areas of mixed magnetic polarity within the predominantly unipolar CHs, this extra heating can be attributed to reconnection between the small bipoles that continually emerge at the photosphere and the neighbouring
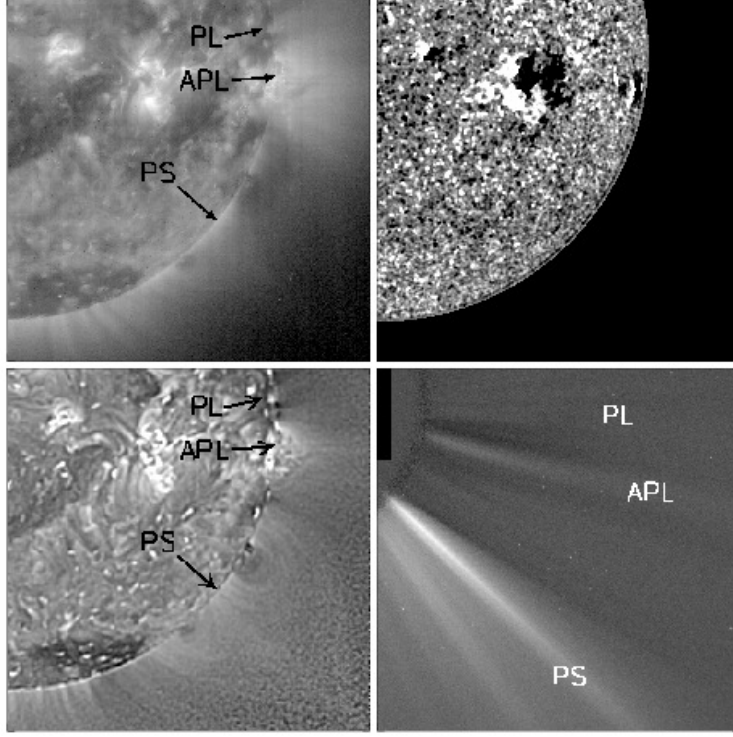
Figure 28: Three kinds of plume-like structures observed at the southwest limb on 6 February 2004: a low-latitude coronal plume (PL), an active region plume (APL) and a pseudostreamer (PS). Top left: EIT Fe IX/X 17.1 nm image at 19:00 UTC. Bottom left: EIT Fe XII 19.5 nm image at 19.13. Top right: MDI magnetogram at 19:15. Bottom right: LASCO-C2 image showing the overlying WL corona beyond $R \approx 2\ R_\odot$ at 19:31. Coronal plumes in the southern PCH can also be seen in the left panels.

unipolar flux concentrations (Wang 1998; Xia et al. 2003; Gabriel et al. 2009). Plumes decay after the underlying minority-polarity flux is cancelled on the ≈ 1 d time scale of the super-granular convection (Wang 1998; DeForest et al. 2001b; Wang and Muglach 2008).

The effect of two coronal heating sources, one spread over a distance on the order of 1 $R_\odot$, the other concentrated very near the coronal base, is illustrated by the SW solutions in Fig. 29 (from Wang 1994). Here, the single-fluid equations of mass, momentum and energy conservation were solved, subject to the boundary condition that the downward heat flux at the coronal base be balanced by the total radiation and enthalpy losses from the TR. The heating function was taken to be of the form

$$
\begin{aligned}
F_{\mathrm{PL}} &= F_{\mathrm{global}} + F_{\mathrm{base}} \\
&= \frac{B}{B_0}\left[F_{\mathrm{g0}} \exp\left(\frac{R_\odot - R}{H_{\mathrm{g}}}\right) + F_{\mathrm{b0}} \exp\left(\frac{R_\odot - R}{H_{\mathrm{b}}}\right)\right] \quad ,
\end{aligned}
\tag{8}
$$

with $F_{\mathrm{g0}} = F_{\mathrm{b0}} = 400\ \mathrm{J\,m^{-2}\,s^{-1}}$ and (for simplicity) $B \propto (R_\odot/R)^2$. The three "plume" solutions in Fig. 29 were obtained by setting H_{b}, the damping length for the base heating, equal to (0.01, 0.02, 0.04) $R_\odot$, and $H_{\mathrm{g}} \approx 1\ R_\odot$, for the global heating, i.e., $H_{\mathrm{b}} << H_{\mathrm{g}}$. An IPR solution is also plotted for comparison, where the base heating is set to zero. Not surprisingly, the strong low-level heating acts to steepen the temperature gradient near the coronal base, giving rise to a local temperature maximum and a large increase in the downward heat flux. As H_{b} is reduced, the temperature "kink" moves inwards and becomes more sharply localized near the footpoint; at the same time, however, the plume temperature decreases.
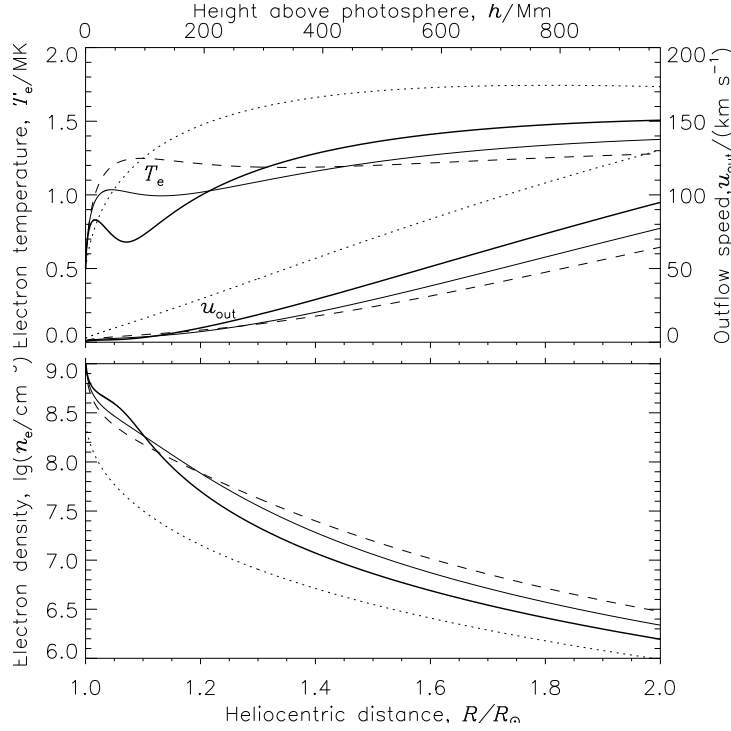
Figure 29: Three different "plume" SW solutions, in which additional energy $F_{b0} = 400$ J m^{-2} s^{-1} is deposited near the coronal base over a damping length $H_b \ll 1 \, R_\odot$. Thick solid lines: $H_b = 0.01 \, R_\odot$. Thin solid lines: $H_b = 0.02 \, R_\odot$. Dashed lines: $H_b = 0.04 \, R_\odot$. For comparison, dotted lines represent the IPR case where $F_{b0} = 0$. The top panel shows the variation of the flow speed, u_{out}, and the electron temperature, T_e, with heliocentric distance, R, while the bottom panel shows the corresponding density variation, $n_e(R)$ (after Wang 1994). At larger distances, the plume streams are only slightly slower than the IPRs ones.

Compared with the IPR solution, the plume models have higher footpoint temperatures but lower temperatures at greater heights, as indeed suggested by the observations plotted in Fig. 18; they are also characterized by substantially smaller flow velocities in the low corona, in general agreement with the Doppler measurements of Fig. 14. The base heating has the desired effect of increasing the plume densities by a factor of ≈ 4 over the IPR solution. Even though the velocities are very low near the plume base, the densities are determined by the mass continuity equation, not by the hydrostatic equilibrium condition; thus there is no contradiction between the high densities and low temperatures of the plume plasma. It may be noted that the calculated densities in Fig. 29 fall off more slowly with height than the observed densities in Fig. 17; this discrepancy is easily removed by adopting a more rapid (and realistic) falloff rate for the magnetic field.

Fig. 7 of Pinto et al. (2009), shows how a plume forms as the base heating rate F_{b0} is suddenly raised from 0 to 400 J m^{-2} s^{-1}. The change in the heating rate generates a wavefront that propagates upward along the flux tube at the local sound speed. The velocities increase during the first several hours, but subsequently fall below the initial (IPR) values as the densities continue to rise and the plasma above the coronal base cools. The cooling is due to increased radiative losses and to the reduction in the energy available per particle as the density increases. The reverse process, in which the base heating is suddenly switched off, is shown in Fig. 8 of Pinto and co-workers. The velocities initially decrease, even becoming slightly negative ($u_0 \approx -1$ km s^{-1}) near the coronal base; the equilibrium profile, in which the speeds are everywhere higher than the plume values, is attained only after ≈ 1 d. We note that it takes as long as ≈ 5 h for the densities to drop by a factor of two, a result

that is consistent with the observed tendency for EUV "plume haze" to linger well after the underlying bright point has faded.

8.2 Beam and network plumes

Both beam plumes and the individual filaments of network plumes (cf., Sect. 3.2) might have similar densities and temperatures; and extend to 1.5 $R_\odot$ to 2.0 $R_\odot$ in VUV images (Gabriel et al. 2009). They are both due to the interaction and reconnection of emerging flux loops (with very different scales) with a monopolar ambient field. Network plumes appear for a maximum of 2 d, due to solar rotation and the evolution time of the network. The individual filaments of network plumes might have a much shorter lifetime. Jets are characterized by a basic monopole-bipole topology similar to that of plumes, but the energy release is far more impulsive, perhaps because the reconnection is driven by the rapid emergence of small bipoles rather than by their slower decay and dispersal in the supergranular flow field.

8.3 Forward modeling

The "forward modeling" approach has been used for many years. The purpose is to obtain simulated images from controlled parameters with the same statistical characteristics (or at least the same visual impression) as images of solar coronal plumes. Wang and Sheeley (1995) simulated plumes and their base areas in PCHs, observed in the Mg IX 38.4 nm line with the slitless spectrograph S082A on Skylab. They demonstrated that bright plumes always show intense network features within their base areas, but the converse does not hold. They also considered how the appearance of UV plumes might depend on their orientation relative to the LOS. From theoretical consideration about the formation of a coronal plume, they deduced a typical time scale $\tau_p = 14$ h for the energy transfer from the network to the plume.

The purpose of simulations in WL is to reproduce their fluffy aspect in TID, i.e., to mimic in space and time the visual behaviour of plumes, as, for instance, shown in Fig. 30. Two different methods were used by Llebaria et al. (2004) to simulate the image sequences and, from it, the TID. The first one is based on a fractal affine model and the second on an evolutive multi-scale model. These models required both the fractal dimension of 2.9 for the 2D electron density distribution over the polar cap. More recently, Boursier and Llebaria (2008) introduced a parametric model based jointly on the "hidden Markov trees" and on the 2D wavelet transform, in order to control both the localization of the electrons and the fractal dimension. Simulations of VUV plumes by Barbey et al. (2008) reproduced the intermittent behaviour of plumes using a dynamic model.

The modeling activities have been successful in the sense that they produce images with realistic plumes and TID structures and their temporal evolution, although a convincing statistical comparison between simulation and reality remains to be done.

9 Conclusions

In line with the definition of work in the introduction, ideally answers should be given here to all questions asked in the proposal phase of this study and discussed in the various sections.
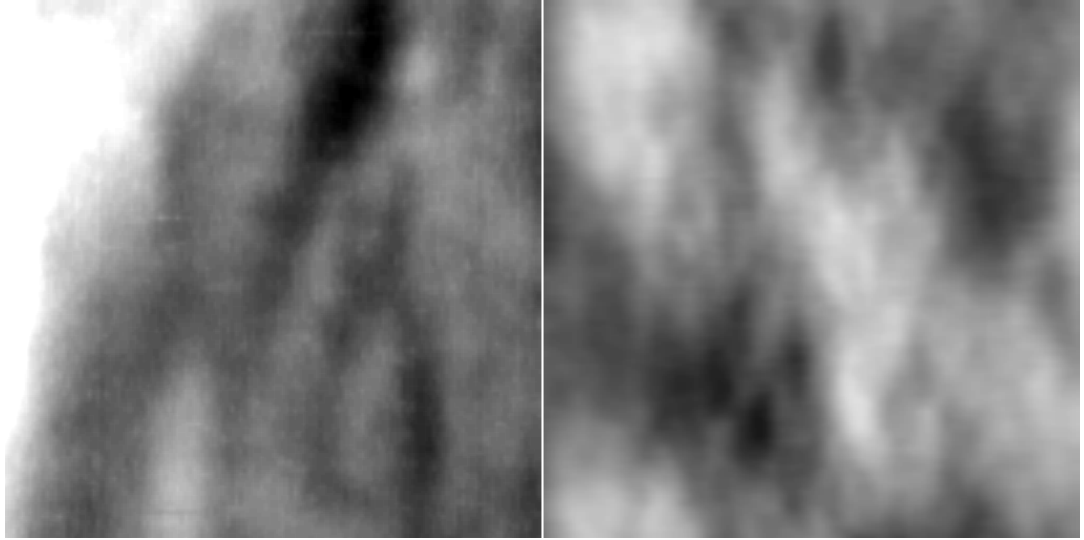
Figure 30: Comparison between a zone of a real TID (128×128 pixels wide) and a TID obtained by simulation: (Left panel) enlarged detail of a real TID; (right panel) enlarged detail of a TID generated from a fractal distribution ($D = 2.9$) of electrons over the polar cap. The simulation includes 3D geometry, Thompson scattering and projection onto the plane of view.

However, the situation is not ideal: not all problems could be solved and, in some cases, not all team members agreed on a proposed solution. Consequently, three categories will have to be listed — accepted results, controversial topics and open questions — before a concluding statement can be made at the end of this section.

1. Agreed results:
   – The fore- and background problem of polar coronal plume observations can be avoided during solar minimum periods, taking into account the N-S asymmetry caused by the 7.25° angle between the solar equator and the ecliptic. Careful consideration of the actual PCH configuration is required as well. The observations of non-polar plumes need special conditions and precautions.
   – Polar plumes delineate magnetic field lines of the minimum corona in PCHs. Plumes expand super-radially — very fast below 30 Mm above the photosphere and more slowly at greater altitudes. IPR funnels basically show the same behaviour in the low β-regime of the corona.
   – Plumes observed in WL and VUV results from plasma density enhancements in CHs.
   – Sinogram analyses established a direct relationship between plumes observed in different wavelength ranges.
   – The electron density ratio between plumes and IPRs is between three and seven in the low corona and decreases at greater heights.
   – The electron temperature in plumes is $T_{\mathrm{e}} \leq 1$ MK. In IPRs it is higher by ≈ 0.2 MK with a tendency of even higher values at greater heights. This is compatible with freeze-in temperatures derived from in situ SW observations.
   – The effective ion temperatures in plumes and IPRs are much higher than the electron

57

temperatures.

– Effective ion temperatures in plumes are lower than in IPRs.

– With stereoscopic observations, 3D reconstructions of more or less cylindrical plumes — called here beam plumes — could be achieved.

– Beam plumes are, in many cases, related to coronal BPs during the beginning of their lifetime that last up to 2 d. They have a recurrence tendency over much longer time scales.

– Plumes show some evolution during their lifetime.

– Compressional waves are frequently observed in plumes, but these slow magnetosonic waves do not seem to carry large energy fluxes.

– Non-compressional Alfvénic waves are thought to be of importance, at least, in IPRs, but are difficult to detect.

– Footpoints of beam plumes lie near magnetic flux concentrations interacting with small magnetic dipoles. The reconnection activity generates heat near the base of a plume and leads to jets that probably provide some of the plume plasma.

– The SW outflow velocity is higher in IPRs than in plumes above a height of $h \approx 0.6\,R_\odot$. The filling factor of plumes in CHs is ≤ 0.1. The IPR contribution to the SW is thus more important than that of plumes.

– Plumes and IPRs have a distinctly different abundance composition, in the sense that the ratio of low-FIP/high-FIP elements is much larger in plumes than in IPRs.

– Coronal plumes observed in low-latitude CHs have very similar properties to plumes in PCHs.

– Rosettes in the chromospheric network could be of importance for the plume formation.

– The ensemble of plumes appears to rotate rigidly within the CH boundaries. The lifetime of a plume is too short for a definite answer.

2. Controversial topics:

– Based on EIT observations, a second class of plumes appears to exist. In contrast to beam plumes, they are composed of small structures — microplumes — with footpoints along network lanes. They are therefore called network plumes and only visible when the LOS is directed in their long dimension.

– It is not excluded that beam plumes are also composed of microplumes in a more compact fashion.

– The indication that plumes can be described as fractals support the microplume concept.

– The outflow speed of the SW at low altitudes is slower in IPRs than in plumes in some studies. Most of the results give, however, higher speeds in IPRs at all heights.

– Plume/IPR signatures in the fast SW at large distances from the Sun based on compositional and magnetic variations appear to be present, but are not sufficiently pronounced for an unambiguous identification.

3. Open questions:

– There are indications of temperature anisotropies of heavy ions both in IPRs and in plumes, but the degree of anisotropy in both regions needs further investigations.

– Although models of plumes and their formation are available, an exact description of the physical processes operating at the base and inside of plumes as well as their interaction with the SW is still outstanding.

    – Is there any contribution of plume plasma to the fast SW streams at all?

    – What produces the clear FIP effect signature between plumes and IPRs?

It is suggested that most of the plumes considered, as well as the more transitory jets, arise from a similar mechanism. This is the emergence of new bipolar loops at the base, interacting by reconnection with an existing ambient, mainly monopolar field. The different spatial and temporal scales observed could then be explained by the differing parameters and reconnection rates. Many indications hint at a fine structure of plumes that cannot be adequately resolved with present-day instrumentation.

References

[1] Abbo L, Zangrilli L, Antonucci E, Fineschi S, Kohl J, Giordano S, Massone G, Capobianco G, Calcidese P, Porcu F (2008) Investigation of the solar wind outflows and joint observations during the total solar eclipse of March 29, 2006. 37th COSPAR Scientific Assembly. Montréal, 13–20 July 2008, Paper: D24-0038-08

[2] Ahmad IA, Withbroe GL (1977) EUV analysis of polar plumes. Solar Phys 53:397–408

[3] Antonucci E, Noci G, Kohl JL, Tondello G, Huber MCE, Giordano S, Benna C, Ciaravella A, Fineschi S, Gardner LD, Martin R, Michels J, Naletto G, Nicolosi P, Panasyuk A, Raymond CJ, Romoli M, Spadaro D, Strachan L, van Ballegooijen A (1997) First results from UVCS: Dynamics of the extended corona. ASP Conf Ser 118:273–277

[4] Antonucci E, Dodero MA, Giordano S (2000) Fast solar wind velocity in a polar coronal hole during solar minimum. Solar Phys 197:115–134

[5] Antonucci E, Dodero MA, Giordano S, Krishnakumar V, Noci G (2004) Spectroscopic measurement of the plasma electron density and outflow velocity in a polar coronal hole. A & A 416:749–758

[6] Axford WI, McKenzie JF (1992) The origin of high speed solar wind streams. In: E Marsch E, Schwenn R (eds) Solar Wind Seven, Pergamon Press, Oxford New York Seoul Tokyo, pp 1–5

[7] Axford WI, McKenzie JF (1996) Implications of observations of the solar wind and corona for solar wind models. Astrophys Space Sci 243:1–3

[8] Balogh A, Beek TJ, Forsyth RJ, Hedgecock PC, Marquedant RJ, Smith EJ, Southwood DJ, Tsurutani BT (1992) The magnetic field investigation on the Ulysses mission — instrumentation and preliminary scientific results. A & ASS 92:221–236

[9] Bame SJ, Asbridge JR, Feldman WC, Gosling JT (1977) Evidence for a structure-free state at high solar wind speeds. J Geophys Res 82:1487–1492

[10] Bame SJ, McComas DJ, Barraclough BL, Phillips JL, Sofaly KJ, Chavez JC, Goldstein BE, Sakurai RK (1992) The Ulysses solar wind plasma experiment. A & ASS 92:237–265

[11] Banaszkiewicz M, Axford WI, McKenzie JF (1998) An analytic solar magnetic field model. A & A 337:940–944

[12] Banerjee D, Teriaca L, Doyle JG, Wilhelm K (1998) Broadening of Si VIII lines observed in the solar polar coronal holes. A & A 339:208–214

[13] Banerjee D, Teriaca L, Doyle JG, Lemaire P (2000a) Polar plumes and inter-plume regions as observed by SUMER on SOHO. Solar Phys 194:43–58

[14] Banerjee D, O'Shea E, Doyle JG (2000b) Long-period oscillations in polar plumes as observed by CDS on SOHO. Solar Phys 196:63–78

[15] Banerjee D, Pérez-Suárez D, Doyle JG (2009a) Signatures of Alfvén waves in the polar coronal holes as seen by EIS/Hinode. A & A 501:L15–L18

[16] Banerjee D, Teriaca L, Gupta GR, Imada S, Stenborg G, Solanki SK (2009b) Propagating waves in polar coronal holes as seen by SUMER & EIS. A & A 499:L29–L32

[17] Barbey N, Auchère F, Rodet T, Vial J-C (2008) A time-evolving 3D method dedicated to the reconstruction of solar plumes and results using extreme ultraviolet data. Solar Phys 248:409–423

[18] Beckers JM (1963) Study of the undisturbed chromosphere from H α disk filtergrams, with particular reference to the identification of spicules. ApJ 138:648–663

[19] Bemporad A, Matthaeus WH, Poletto G (2008) Low-frequency Ly α power spectra observed by UVCS in a polar coronal hole. ApJ 677:L137–L140

[20] Bohlin JD (1977) Extreme-ultraviolet observations of coronal holes. I – Locations, sizes and evolution of coronal holes, June 1973–January 1974. Solar Phys 51:377–398

[21] Bohlin JD, Sheeley NR Jr (1978) Extreme ultraviolet observations of coronal holes. II – Association of holes with solar magnetic fields and a model for their formation during the solar cycle. Solar Phys 56:125–151

[22] Boursier Y, Llebaria A (2005) Etude, modelisation et simulation des plumes polaires. Rapport de DEA, Université de Provence

[23] Boursier Y, Llebaria A (2008) 3D dynamic forward modeling of polar plumes using hidden Markov trees. St Met 5:328–339

[24] Brekke P, Hassler DM, Wilhelm K (1997) Doppler shifts in the quiet-Sun transition region and corona observed with SUMER on SOHO. Solar Phys 175:349–374

[25] Budnik F, Schröder K-P, Wilhelm K, Glassmeier K-H (1998) Observational evidence for coronal mass injection by "evaporation" of spicular plasma. A & A 334:L77–L80

[26] Casalbuoni S, Del Zanna L, Habbal SR, Velli M (1999) Coronal plumes and the expansion of pressure-balanced structures in the fast solar wind. J Geophys Res 104:9947–9961

[27] Chae J, Yun HS, Poland AI (1998) Temperature dependence of ultraviolet line average Doppler shifts in the quiet Sun. ApJSS 114:151–164

[28] Corti G, Poletto G, Romoli M, Michels J, Kohl J, Noci G (1997) Physical parameters in plume and interplume regions from UVCS observations. ESA SP-404:289–294

[29] Cranmer SR (2009) Coronal Holes. LRSP 6:3–63

[30] Cranmer SR, Kohl JL, Noci G, Antonucci E, Tondello G, Huber MCE, Strachan L, Panasyuk AV, Gardner LD, Romoli M, Fineschi S, Dobrzycka D, Raymond JC, Nicolosi P, Siegmund OHW, Spadaro D, Benna C, Ciaravella A, Giordano S, Habbal SR, Karovska M, Li X, Martin R, Michels JC, Modigliani A, Naletto G, O'Neal RH, Pernechele C, Poletto G, Smith PL, Suleiman RM (1999) An empirical model of a polar coronal hole at solar minimum. ApJ 511:481-501

[31] Cranmer SR, van Ballegooijen AA, Edgar RJ (2007) Self-consistent coronal heating and solar wind acceleration from anisotropic magnetohydrodynamic turbulence. ApJSS 171:520–551

[32] Crooker NU, Gosling JT, Kahler SW (2002) Reducing heliospheric magnetic flux from coronal mass ejections without disconnection. J Geophys Res 107:SSH3-1–5, DOI 10.1029/2001JA000236

[33] Culhane JL, Harra LK, James AM, Al-Janabi K, Bradley LJ, Chaudry RA, Rees K, Tandy JA, Thomas P, Whillock MCR, Winter B, Doschek GA, Korendyke CM, Brown CM, Myers S, Mariska J, Seely J, Lang J, Kent BJ, Shaughnessy BM, Young PR, Simnett GM, Castelli CM, Mahmoud S, Mapson-Menard H, Probyn BJ, Thomas RJ, Davila J, Dere K, Windt D, Shea J, Hagood R, Moye R, Hara H, Watanabe T, Matsuzaki K, Kosugi T, Hansteen V, Wikstøl Ø (2007) The EUV Imaging Spectrometer for Hinode. Solar Phys 243:19–61

[34] Cuntz M, Suess ST (2001) Shock formation of slow magnetosonic waves in coronal plumes. ApJ 549:L143–L146

[35] Curdt W, Wilhelm K, Feng L, Kamio S (2008) Multi-spacecraft observations of polar coronal plumes. A & A 481:L61–L64

[36] David C, Gabriel AH, Bely-Dubau F, Fludra A, Lemaire P, Wilhelm K (1998) Measurement of the electron temperature gradient in a solar coronal hole. A & A 336:L90–L94

[37] DeForest CE (2007) On the size of structures in the solar corona. ApJ 661:532–542

[38] DeForest CE, Gurman JB (1998) Observation of quasi-periodic compressive waves in solar polar plumes. ApJ 501:L217–L220

[39] DeForest CE, Hoeksema JT, Gurman JB, Thompson BJ, Plunkett SP, Howard R, Harrison RC, Hassler DM (1997) Polar plume anatomy: Results of a coordinated observation. Solar Phys 175:393–410

[40] DeForest CE, Plunkett SP, Andrews MD (2001a) Observation of polar plumes at high solar altitudes. ApJ 546:569–575

[41] DeForest CE, Lamy PL, Llebaria A (2001b) Solar polar plume lifetime and coronal hole expansion: Determination from long-term observations. ApJ 560:490–498

[42] Del Zanna G, Bromage BJI (1999) The elepfant's trunk: Spectroscopic diagnostics applied to SOHO/CDS observations of the August 1996 equatorial coronal hole. J Geophys Res 104:9753–9766

[43] Del Zanna G, Bromage BJI, Mason HE (2003) Spectroscopic characteristics of polar plumes. A & A 398:743–761

[44] Del Zanna G, Rozum I, Badnell NR (2008) Electron-impact excitation of Be-like Mg. A & A 487:1203–1208

[45] Del Zanna L, Hood AW, Longbottom AW (1997) An MHD model for solar coronal plumes. A & A 318:963–969

[46] De Pontieu B, McIntosh SW, Hansteen VH, Schrijver CJ (2009) Observing the roots of solar coronal heating in the chromosphere. ApJ 701:L1–L6

[47] Dere KP, Bartoe J-DF, Brueckner GE, Recely F (1989) Explosive events and magnetic reconnection in the solar atmosphere. ApJ 345:L95–L97

[48] Dere KP, Bartoe J-DF, Brueckner GE, Ewing J, Lund P (1991) Explosive events and magnetic reconnection in the solar atmosphere. J Geophys Res 96:9399–9407

[49] Dmitruk P, Matthaeus WH (2009) Waves and turbulence in magnetohydrodynamic direct numerical simulations. Phys Plasmas 16:062304-1–9

[50] Dmitruk P, Matthaeus WH, Milano LJ, Oughton S (2001) Conditions for sustainment of magnetohydrodynamic turbulence driven by Alfvén waves. Phys Plasmas 8:2377–2384

[51] Dmitruk P, Matthaeus WH, Milano LJ, Oughton S, Zank GP, Mullan DJ (2002) Coronal heating distribution due to low frequency wave driven turbulence. ApJ 575:571–577

[52] Dobrzycka D, Cranmer SR, Raymond JC, Biesecker DA, Gurman JB (2002) Polar coronal jets at solar minimum. ApJ 565:621–629

[53] Dolla L, Solomon J (2008) Solar off-limb line widths: Alfvén waves, ion-cyclotron waves, and preferential heating. A & A 483:271–283

[54] Domingo V, Fleck B, Poland AI (1995) The SOHO Mission: An overview. Solar Phys 162:1–37

[55] Doschek GA, Feldman U, Bohlin JD (1976) Doppler wavelength shifts of transition zone lines measured in SKYLAB solar spectra. ApJ 205:L177–L180

[56] Doschek GA, Warren HP, Laming JM, Mariska JT, Wilhelm K, Lemaire P, Schühle U, Moran TG (1997) Electron densities in the solar polar coronal holes from density-sensitive line ratios of Si VIII and S X. ApJ 482:L109–L112

[57] Doschek GA, Laming JM, Feldman U, Wilhelm K, Lemaire P, Schühle U, Hassler DM (1998) The Si/Ne abundance ratio in polar coronal hole and quiet-Sun coronal regions. ApJ 504:573–587

[58] Doschek GA, Feldman U, Laming JM, Schühle U, Wilhelm K (2001) Properties of solar polar coronal hole plasmas observed above the limb. ApJ 546:559–568

[59] Dowdy JF, Rabin D, Moore RL (1986) On the magnetic structure of the quiet transition region. Solar Phys 105:35–45

[60] Doyle JG, Teriaca L, Banerjee D (1999) Coronal hole diagnostics out to 8 $R_\odot$. A & A 349:956–960

[61] Doyle JG, Madjarska MS, Dzifčáková E, Dammasch IE (2004) Coronal response of bi-directional jets. Solar Phys 221:51–64

[62] Dwivedi BN, Mohan A, Wilhelm K (2000) On the electron temperatures, densities and hot ions in coronal hole plasma observed by SUMER on SOHO. Adv Space Res 25:1751–1756

[63] Esser R, Fineschi S, Dobrzycka D, Habbal SR, Edgar RJ, Raymond JC, Kohl JL, Guhathakurta M (1999) Plasma properties in coronal holes derived from measurements of minor ion spectral lines and polarized white light intensity. ApJ 510:L63–L67

[64] Feldman U, Schühle U, Widing KG, Laming JM (1998) Coronal composition above the solar equator and the north pole as determined from spectra acquired by the SUMER instrument on SOHO. ApJ 505:999–1006

[65] Feldman U, Dammasch IE, Wilhelm K (2001) On the unresolved fine structures of the solar upper atmosphere. IV. The interface with the chromosphere. ApJ 558:423–427

[66] Feldman U, Dammasch IE, Wilhelm K, Lemaire P, Hassler DM (2003) Images of the solar upper atmosphere from SUMER on SOHO. ESA SP-1274:1–30 (A1–A208)

[67] Feng L, Inhester B, Solanki SK, Wilhelm K, Wiegelmann T, Podlipnik B, Howard RA, Plunkett SP, Wuelser JP, Gan WQ (2009) Stereoscopic polar plume reconstructions from STEREO/SECCHI images. ApJ 700:292–301

[68] Fisher R, Guhathakurta M (1995) Physical properties of polar coronal rays and holes as observed with the Spartan 201-01 coronagraph. ApJ 447:L139–L142

[69] Flower DR, Nussbaumer H (1975) On the extreme ultraviolet solar emission of B-like ions: O IV. A & A 45:145–150

[70] Fludra A, Del Zanna G, Alexander D, Bromage BJI (1999) Electron density and temperature of the lower solar corona. J Geophys Res 104:9709–9720

[71] Frazin RA (2000) Tomography of the solar corona. ApJ 530:1026–1035

[72] Gabriel AH (1976) A magnetic model of the solar transition region. Phil Trans R Soc Lond A 281:339–352

[73] Gabriel AH, Jordan C (1973) The temperature dependence of line ratios of helium-like ions. ApJ 186:327–334

[74] Gabriel AH, Patchett BE, Lang J, Culhane JL, Norman K (1986) Early results from the CHASE experiment flown on Spacelab 2. Brit Interplanet Soc J 39:207–210

[75] Gabriel AH, Bely-Dubau F, Lemaire P (2003) The contribution of polar plumes to the fast solar wind. ApJ 589:623–634

[76] Gabriel AH, Abbo L, Bely-Dubau F, Llebaria A, Antonucci E (2005) Solar wind outflow in polar plumes from 1.05 to 2.4 R_S. ApJ 635:L185–L188

[77] Gabriel A, Bely-Dubau F, Tison E, Wilhelm K (2009) The structure and origin of solar plumes: Network plumes. ApJ 700:551–558

[78] Geiss J, Gloeckler G, von Steiger R (1995) Origin of the solar wind from composition data. Space Sci Rev 72:49-60

[79] Giordano S, Antonucci E, Benna C, Romoli M, Noci G, Kohl JL, Fineschi S, Michels J, Naletto G (1997) Plume and inter-plume regions and solar wind acceleration in polar coronal holes between 1.5 and 3.5 $R_\odot$. ESA SP-404:413–416

[80] Giordano S, Antonucci E, Dodero MA (2000a) Oxygen outflow velocities in a polar coronal hole. Adv Space Res 25:1927–1930

[81] Giordano S, Antonucci E, Noci G, Romoli M, Kohl JL (2000b) Identification of the coronal sources of the fast solar wind. ApJ 531:L79–L82

[82] Gloeckler G, Geiss J, Balsiger H, Bedini P, Cain JC, Fisher J, Fisk LA, Galvin AB, Gliem F, Hamilton DC (1992) The Solar Wind Ion Composition Spectrometer. A & ASS 92:267–289

[83] Goldstein BE, Neugebauer M, Phillips JL, Bame S, Gosling JT, McComas D, Wang Y-M, Sheeley NR, Suess ST (1996) Ulysses plasma parameters: latitudinal, radial, and temporal variations. A & A 316:296–303

[84] Golub L, Deluca E, Austin G, Bookbinder J, Caldwell D, Cheimets P, Cirtain J, Cosmo M, Reid P, Sette A, Weber M, Sakao T, Kano R, Shibasaki K, Hara H, Tsuneta S, Kumagai K, Tamura T, Shimojo M, McCracken J, Carpenter J, Haight H, Siler R, Wright E, Tucker J, Rutledge H, Barbera M, Peres G, Varisco S (2007) The X-Ray Telescope (XRT) for the Hinode mission. Solar Phys 243:63–86

[85] Grevesse N, Sauval AJ (1998) Standard solar composition. Space Sci Rev 85:161–174

[86] Guhathakurta M, Fisher R (1995) Coronal streamers and fine scale structures of the low latitude corona as detected with Spartan 201-01 white light coronagraph. Geophys Res Lett 22:1841–1844

[87] Gupta GR, O'Shea E, Banerjee D, Popescu M, Doyle JG (2009) On the statistical detection of propagating waves in polar coronal holes. A & A 493:251–257

[88] Gupta GR, Banerjee D, Teriaca L, Imada S, Solanki S (2010) Accelerating waves in polar coronal holes as seen by EIS and SUMER. ApJ 718:11–22

[89] Habbal SR, Esser R, Arndt MB (1993) How reliable are coronal hole temperatures deduced from observations? ApJ 413:435–444

[90] Habbal SR, Esser R, Guhathakurta M, Fisher RR (1995) Flow properties of the solar wind derived from a two-fluid model with constraints from white light and in situ interplanetary observations. Geophys Res Lett 22:1465–1468

[91] Handy BN, Acton LW, Kankelborg CC, Wolfson CJ, Akin DJ, Bruner ME, Caravalho R, Catura RC, Chevalier R, Duncan DW, Edwards CG, Feinstein CN, Freeland SL, Friedlaender FM, Hoffmann CH, Hurlburt NE, Jurcevich BK, Katz NL, Kelly GA, Lemen JR, Levay M, Lindgren RW, Mathur DP, Meyer SB, Morrison SJ, Morrison MD, Nightingale RW, Pope TP, Rehse RA, Schrijver CJ, Shine RA, Shing L, Strong KT, Tarbell TD, Title AM, Torgerson DD, Golub L, Bookbinder JA, Caldwell D, Cheimets PN, Davis WN, Deluca EE, McMullen RA, Warren HP, Amato D, Fisher R, Maldonado H, Parkinson C (1999) The Transition Region and Coronal Explorer. Solar Phys 187:229–260

[92] Hara H, Watanabe T, Harra LK, Culhane JL, Young PR, Mariska JT, Doschek GA (2008) Coronal plasma motions near footpoints of active region loops revealed from spectroscopic observations with Hinode EIS. ApJ 678:L67–L71

[93] Hardee PE, Clarke DA (1995) Destabilization of strongly magnetized jets. ApJ 449:119–133

[94] Hassler DM, Rottman GJ, Shoub EC, Holzer TE (1990) Line broadening of Mg x 609 and 625 Å coronal emission lines observed above the solar limb. ApJ 348:L77–L80

[95] Hassler DM, Wilhelm K, Lemaire P, Schühle U (1997) Observations of polar plumes with the SUMER instrument on SOHO. Solar Phys 175:375–391

[96] Hassler DM, Dammasch IE, Lemaire P, Brekke P, Curdt W, Mason HE, Vial J-C, Wilhelm K (1999) Solar wind outflow and the chromospheric magnetic network. Science 283:810–813

[97] Hiei E, Takahashi N, the Eclipse Group of Meisei University (2000) Ground-based and SOHO observations of polar plumes during eclipse. Adv Space Res 25:1887–1891

[98] Howard RA, Moses JD, Vourlidas A, Newmark JS, Socker DG, Plunkett SP, Korendyke CM, Cook JW, Hurley A, Davila JM, Thompson WT, St Cyr OC, Mentzell E, Mehalick K, Lemen JR, Wuelser JP, Duncan DW, Tarbell TD, Wolfson CJ, Moore A, Harrison RA, Waltham NR, Lang J, Davis CJ, Eyles CJ, Mapson-Menard H, Simnett GM, Halain JP, Defise JM, Mazy E, Rochus P, Mercier R, Ravet MF, Delmotte F, Auchère F, Delaboudinière JP, Bothmer V, Deutsch W, Wang D, Rich N, Cooper S, Stephens V, Maahs G, Baugh R, McMullin D, Carter T (2008) Sun Earth Connection Coronal and Heliospheric Investigation (SECCHI). Space Sci Rev 136:67–115

[99] Huber MCE, Foukal PV, Noyes RW, Reeves EM, Schmahl EJ, Timothy JG, Vernazza JE, Withbroe GL (1974) Extreme-ultraviolet observations of coronal holes — initial results from SKYLAB. ApJ 194:L115–L118

[100] Imada S, Hara H, Watanabe T (2009) Ion temperature and non-thermal velocity in a solar active region: Using emission lines of different atomic species. ApJ 705: L208-L212

[101] Innes DE, Inhester B, Axford WI, Wilhelm K (1997) Bi-directional plasma jets produced by magnetic reconnection on the Sun. Nature 386:811–813

[102] Ito H, Tsuneta S, Shiota D, Tokumaru M, Fujiki K (2010) Is the polar region different from the quiet region of the Sun? ApJ 719:131–142

[103] Jess DB, Mathioudakis M, Erdélyi R, Crockett PJ, Keenan FP, Christian DJ (2009) Alfvén waves in the lower solar atmosphere. Science 323:1582–1585

[104] Judge PG, Hansteen V, Wikstøl Ø, Wilhelm K, Schühle U, Moran T (1998) Evidence in support of the "nanoflare" picture of coronal heating from SUMER data. ApJ 502:981–996

[105] Kamio S, Curdt W, Teriaca L, Inhester B, Solanki SK (2010) Observations of a rotating macrospicule associated with an X-ray jet. A & A 510:L1–L4

[106] Keenan FP, Kingston AE, Dufton PL, Doyle JG, Widing KG (1984) Mg IX and Si XI line ratios in the Sun. Solar Phys 94:91–98

[107] Keller CU, Harvey JW, the SOLIS Team (2003) The SOLIS vector-spectro-magnetograph. ASP Conf Ser 307:13–22

[108] Ko Y-K, Fisk LA, Geiss J, Gloeckler G, Guhathakurta M (1997) An empirical study of the electron temperature and heavy ion velocities in the south polar coronal hole. Solar Phys 171:345-361

[109] Kohl JL, Withbroe GL (1982) EUV spectroscopic plasma diagnostics for the solar wind acceleration region. ApJ 256:263–270

[110] Kohl JL, Gardner LD, Strachan L, Fisher R, Guhathakurta M (1995) Spartan 201 coronal spectroscopy during the polar passes of Ulysses. Space Sci Rev 72:29–38

[111] Kohl JL, Noci G, Antonucci E, Tondello G, Huber MCE, Gardner LD, Nicolosi P, Strachan L, Fineschi S, Raymond JC, Romoli M, Spadaro D, Panasyuk A, Siegmund OHW, Benna C, Ciaravella A, Cranmer SR, Giordano S, Karovska M, Martin R, Michels J, Modigliani A, Naletto G, Pernechele C, Poletto G, Smith PL (1997) First results from the SOHO Ultraviolet Coronagraph Spectrometer. Solar Phys 175:613–644

[112] Kohl JL, Esser R, Cranmer SR, Fineschi S, Gardner LD, Panasyuk AV, Strachan L, Suleiman RM, Frazin RA, Noci G (1999) EUV spectral line profiles in polar coronal holes from 1.3 to 3.0 $R_\odot$. ApJ 510:L59–L62

[113] Kohl JL, Noci G, Cranmer SR, Raymond JC (2006) Ultraviolet spectroscopy of the extended solar corona. A & ARev 13:31–157

[114] Kopp RA, Holzer TE (1976) Dynamics of coronal hole regions. I - Steady polytropic flows with multiple critical points. Solar Phys 49:43–56

[115] Kosugi T, Matsuzaki K, Sakao T, Shimizu T, Sone Y, Tachikawa S, Hashimoto T, Minesugi K, Ohnishi A, Yamada T, Tsuneta S, Hara H, Ichimoto K, Suematsu Y, Shimojo M, Watanabe T, Shimada S, Davis JM, Hill LD, Owens JK, Title AM, Culhane JL, Harra LK, Doschek GA, Golub L (2007) The Hinode (Solar-B) mission: An overview. Solar Phys 243:3–17

[116] Koutchmy S (1977) Study of the June 30, 1973 trans-polar coronal hole. Solar Phys 51:399-407

[117] Koutchmy S (1994) Coronal physics from eclipse observations. Adv Space Res 14:(4)29–39

[118] Koutchmy S, Bocchialini K (1998) White-light polar plumes from solar eclipses. ESA SP-421:51–62

[119] Koutchmy S, Daniel J-Y, Mouette J, Vilinga J, Noëns J-C, Damé L, Faurobert M, Dara H, Hady A, Semeida M, Sabry M, Domenech, A, Munier J-M, Jimenez R, Legault Th, Viladrich Ch, Kuzin S, Pertsov A, the O.A. Team (2006) Preliminary results from the March 29, 2006 total eclipse observations in Egypt. Proc Annual Meeting Soc Francaise Astron Astrophys, 547–548

[120] Krieger AS, Timothy AF, Roelof EC (1973) A coronal hole and its identification as the source of a high velocity solar wind stream. Solar Phys 29:505–525

[121] Laming JM, Feldman U (2001) The solar helium abundance in the outer corona determined from observations with SUMER/SOHO. ApJ 546:552–559

[122] Laming JM, Feldman U, Schühle U, Lemaire P, Curdt W, Wilhelm K (1997) Electron density diagnostics for the solar upper atmosphere from spectra obtained by SUMER/SOHO. ApJ 485:911–919

[123] Lamy P, Llebaria A, Koutchmy S, Reynet P, Molodensky M, Howard R, Schwenn R, Simnett G (1997) Characterization of polar plumes from LASCO-C2 images in early 1996. ESA SP-404:487–490

[124] Landi E (2008) The off-disk thermal structure of a polar coronal hole. ApJ 685:1270–1276

[125] Landi E, Feldman U, Doschek GA (2007) Neon and oxygen absolute abundances in the solar corona. ApJ 659:743–749

[126] Lites BW, Card G, Elmore DF, Holzer T, Lecinski A, Streander KV, Tomczyk S, Gurman JB (1999) Dynamics of polar plumes observed at the 1998 February 26 eclipse. Solar Phys 190:185–206

[127] Llebaria A, Lamy P, DeForest CE, Koutchmy S (1998) Time domain analysis of polar plumes observed with LASCO-C2 and EIT. ESA SP-421:87–92

[128] Llebaria A, Thernisien A, Lamy P (2001) Projective transform techniques to reconstruct the 3-D structure and the temporal evolution of solar polar plumes. ASP Conf Ser 238:377–380

[129] Llebaria A, Saez F, Lamy P (2002a) The fractal nature of the polar plumes. ESA SP-508:391–394

[130] Llebaria A, Thernisien A, Lamy P (2002b) Characterization of the polar plumes from high cadence LASCO-C2 observations. Adv Space Res 29:343–348

[131] Llebaria A, Boulanger J, Boursier Y (2004) Time domain analysis of polar plumes observed with the LASCO/SOHO coronagraph. Proc ADA-III, Astron Data Analysis Conf, eWIC Conf (http://www.bcs.org/server.php?show=conWebDoc.3885)

[132] Llebaria A, Loirat J, Lamy P (2010) Restitution of multiple overlaid components on extremely long series of solar corona images. SPIE Proc 7533:0Y-1–8

[133] Madjarska MS, Doyle JG, Teriaca L, Banerjee D (2003) An EUV bright point as seen by SUMER, CDS, MDI and EIT on-board SOHO. A & A 398:775–784

[134] Mariska JT (1992) The solar transition region. Cambridge University Press, Cambridge

[135] Marsch E, Tu C-Y (1997) Solar wind and chromospheric network. Solar Phys 176:87–106.

[136] Marsch E, Tu C-Y, Wilhelm K, Curdt W, Schühle U, Dammasch IE (1997) Bright plumes and dark lanes as observed in Mg x 625 Å and N v 1239 Å in the solar polar corona. ESA SP-404:555–560

[137] Mason HE, Young PR, Pike CD, Harrison RA, Fludra A, Bromage BJI, Del Zanna G (1997) Application of spectroscopic diagnostics to early observations with the SOHO Coronal Diagnostic Spectrometer. Solar Phys 170:143–161

[138] Matthaeus WH, Goldstein ML (1986) Low-frequency 1/f noise in the interplanetary magnetic field. Phys Rev Lett 57:495–498

[139] Matthaeus WH, Zank GP, Oughton S, Mullan DJ, Dmitruk P (1999) Coronal heating by magnetohydrodynamic turbulence driven by reflected low-frequency waves. ApJ 523:L93–L96

[140] Matthaeus WH, Breech B, Dmitruk P, Bemporad A, Poletto G, Velli M, Romoli M (2007) Density and magnetic field signatures of interplanetary 1/f noise. ApJ 657:L121–L124

[141] Mazzotta P, Mazzitelli G, Colafrancesco S, Vittorio N (1998) Ionization balance for optically thin plasmas: Rate coefficients for all atoms and ions of the elements H to Ni. A & ASS 133:403–409

[142] McKenzie JF, Banaszkiewicz M, Axford WI (1995) Acceleration of the high speed solar wind. A & A 303:L45–L48

[143] Miralles MP, Cranmer SR, Kohl JL (2001) Ultraviolet Coronagraph Spectrometer observations of a high-latitude coronal hole with high oxygen temperatures and the next solar cycle polarity. ApJ 560:L193–L196

[144] Moran T, Gopalswamy N, Dammasch IE, Wilhelm K (2001) A multi-wavelength study of solar coronal-hole regions showing radio enhancements. A & A 378:1037–1045

[145] Moses D, Clette F, Delaboudinière J-P, Artzner GE, Bougnet M, Brunaud J, Carabetian C, Gabriel AH, Hochedez JF, Millier F, Song XY, Au B, Dere KP, Howard RA, Kreplin R, Michels DJ, Defise JM, Jamar C, Rochus P, Chauvineau JP, Marioge JP, Catura RC, Lemen JR, Shing L, Stern RA, Gurman JB, Neupert WM, Newmark J, Thompson B, Maucherat A, Portier-Fozzani F, Berghmans D, Cugnon P, van Dessel EL, Gabryl JR (1997) EIT observations of the extreme ultraviolet Sun. Solar Phys 175:571–599

[146] Munro RH, Jackson BV (1977) Physical properties of a coronal hole from 2 to 5 $R_\odot$. ApJ 213:874–886

[147] Neugebauer M, Goldstein BE, McComas DJ, Suess ST, Balogh A (1995) Ulysses observations of microstreams in the solar wind from coronal holes. J Geophys Res 100:23 389–23 395

[148] Newkirk G Jr, Harvey J (1968) Coronal polar plumes. Solar Phys 3:321–343

[149] Noci G, Kohl JL, Withbroe GL (1987) Solar wind diagnostics from Doppler-enhanced scattering. ApJ 315:706–715.

[150] November LJ, Koutchmy S (1996) White-light coronal dark threads and density fine structure. ApJ 466:512–528

[151] Ofman L (2005) MHD waves and heating in coronal holes. Space Sci Rev 120:67–94

[152] Ofman L, Davila JM (1995) Alfvén wave heating of coronal holes and the relation to the high-speed solar wind. J Geophys Res 100:23 413–23 425

[153] Ofman L, Romoli M, Poletto G, Noci G, Kohl JL (1997) Ultraviolet Coronagraph Spectrometer observations of density fluctuations in the solar wind. ApJ 491:L111–L114

[154] Ofman L, Nakariakov VM, DeForest CE (1999) Slow magnetosonic waves in coronal plumes. ApJ 514:441–447

[155] Ofman L, Romoli M, Poletto G, Noci G, Kohl JL (2000a) UVCS WLC observations of compressional waves in the south polar coronal hole. ApJ 529:592–598

[156] Ofman L, Nakariakov VM, Sehgal N (2000b) Dissipation of slow magnetosonic waves in coronal plumes. ApJ 533:1071–1083

[157] Parhi S, Suess ST, Sulkanen M (1999) Can Kelvin–Helmholtz instabilities of jet-like structures and plumes cause solar wind fluctuations at 1 AU? J Geophys Res 104:14 781–14 787

[158] Parker EN (1988) Nanoflares and the solar X-ray corona. ApJ 330:474–479

[159] Pasachoff JM, Rušin V, Druckmüller M, Druckmüllerová, H, Bělík M, Saniga M, Minarovjech M, Marková E, Babcock BA, Souza SP, Levitt JS (2008) Polar plume brightening during the 2006 March 29 total eclipse. ApJ 682:638–643

[160] Pasachoff JM, Rušin V, Druckmüller M, Aniol P, Saniga M, Minarovjech M (2009) The 2008 August 1 eclipse solar-minimum corona unraveled. ApJ 702:1297–1308

[161] Patsourakos S, Vial J-C (2000) Outflow velocity of interplume regions at the base of polar coronal holes. A & A 359:L1–L4

[162] Phillips KJH, Sylwester J, Sylwester B, Landi E (2003) Solar flare abundances of potassium, argon, and sulphur. ApJ 589:L113–L116

[163] Pinto R, Grappin R, Wang Y-M, Léorat J (2009) Time-dependent hydrodynamical simulations of slow solar wind, coronal inflows, and polar plumes. A & A 497:537–543

[164] Pinto R, Grappin R, Léorat J(2010) Coronal inflows and giant polar plumes. AIP Conf Proc 1216:80–83

[165] Pneuman GW, Kopp RA (1978) Downflow in the supergranulation network and its implications for transition region models. Solar Phys 57:49-64

[166] Poletto G, Parenti S, Noci G, Livi S, Suess ST, Balogh A, McComas DJ (1996) Searching for coronal plumes in Ulysses observations of the far solar wind. A & A 316:374–383

[167] Popescu MD, Doyle JG, Xia L-D (2004) Network boundary origins of fast solar wind seen in the low transition region? A & A 421:339–348

[168] Popescu MD, Banerjee D, O'Shea E, Doyle JG, Xia L-D (2005) Very long period activity at the base of solar wind streams. A & A 442:1087–1090

[169] Pottasch SR (1963) The lower solar corona: Interpretation of the ultraviolet spectrum. ApJ 137:945–966

[170] Raouafi N-E, Harvey JW, Henney CJ (2007a) Latitude distribution of polar magnetic flux in the chromosphere near solar minimum. ApJ 669:636–641

[171] Raouafi N-E, Harvey JW, Solanki SK (2007b) Properties of solar polar coronal plumes constrained by Ultraviolet Coronagraph Spectrometer data. ApJ 658:643–656

[172] Raouafi N-E, Petrie GJD, Norton AA, Henney CJ, Solanki SK (2008) Evidence for polar jets as precursors of polar plume formation. ApJ 682:L137–L140

[173] Raymond JC, Doyle JG (1981) Emissivities of strong ultraviolet lines. ApJ 245:1141–1144

[174] Reisenfeld DB, Mc Comas DJ, Steinberg JT (1999) Evidence of a solar origin for pressure balance structures in the high-latitude solar wind. Geophys Res Lett 26:1805–1808

[175] Rompolt B (1967) The Hα radiation field in the solar corona for moving prominences. Acta Astron 17:329–340

[176] Saito K (1965a) Polar rays of the solar corona observed at the 1965 May 30 eclipse in the South Pacific. PASJ 17:421–426

[177] Saito K (1965b) Polar rays of the solar corona, II. PASJ 17:1–26

[178] Seely JF, Feldman U, Schühle U, Wilhelm K, Curdt W, Lemaire P (1997) Turbulent velocities and ion temperatures in the solar corona obtained from SUMER line widths. ApJ 484:L87–L90

[179] Sheeley NR Jr, Wang Y-M, Hawley SH, Brueckner GE, Dere KP, Howard RA, Koomen MJ, Korendyke CM, Michels DJ, Paswaters SE, Socker DG, St Cyr OC, Wang D, Lamy PL, Llebaria A, Schwenn R, Simnett GM, Plunkett S, Biesecker DA (1997) Measurements of flow speeds in the corona between 2 and 30 $R_\odot$. ApJ 484:472–478

[180] St Cyr O C, Howard RA, Simnett GM, Gurman JB, Plunkett SP, Sheeley NR, Schwenn R, Koomen MJ, Brueckner GE, Michels DJ, Andrews M, Biesecker DA, Cook J, Dere KP, Duffin R, Einfalt E, Korendyke CM, Lamy PL, Lewis D, Llebaria A, Lyons M, Moses JD, Moulton NE, Newmark J, Paswaters SE, Podlipnik B, Rich N, Schenk KM, Socker DG, Stezelberger ST, Tappin SJ, Thompson B, Wang D (1997) White-light coronal mass ejections: A new perspective from LASCO. ESA SP-415:103–110

[181] Suematsu Y, Tsuneta S, Ichimoto K, Shimizu T, Otsubo M, Katsukawa Y, Nakagiri M, Noguchi M, Tamura T, Kato Y, Hara H, Kubo M, Mikami I, Saito H, Matsushita T, Kawaguchi N, Nakaoji T, Nagae K, Shimada S, Takeyama N, Yamamuro T (2008) The Solar Optical Telescope of Solar-B (Hinode): The Optical Telescope Assembly. Solar Phys 249:197–220

[182] Suess ST (1998) Models of plumes: Their flow, their geometric spreading, and their mixing with interplume flow. ESA SP-421:223–230

[183] Suess ST (2000) The Sun and the solar wind close to the Sun. Adv Space Res 26:761–770

[184] Suess ST, Poletto G, Wang A-H, Wu ST, Cuseri I (1998) The geometric spreading of coronal plumes and coronal holes. Solar Phys 180:231–246

[185] Teriaca L, Madjarska MS, Doyle JG (2002) Transition region explosive events: Do they have a coronal counterpart? A & A 392:309–317

[186] Teriaca L, Poletto G, Romoli M, Biesecker DA (2003) The nascent solar wind: Origin and acceleration. ApJ 588:566–577

[187] Thieme KM, Marsch E, Schwenn R (1990) Spatial structures in high-speed streams as signatures of fine structures in coronal holes. Ann Geophys 8:713–723

[188] Tian H, Marsch E, Tu C-Y, Xia L-D, He J-S (2008) Sizes of transition-region structures in coronal holes and in the quiet Sun. A & A 482:267–272

[189] Tian H, Tu C-Y, Marsch E, He J, Kamio S (2010) The nascent fast solar wind observed by the EUV Imaging Spectrometer on board Hinode. ApJ 709:L88–L93

[190] Timothy AF, Krieger AS, Vaiana GS (1975) The structure and evolution of coronal holes. Solar Phys 42:135–156

[191] Tsuneta S, Ichimoto K, Katsukawa Y, Nagata S, Otsubo M, Shimizu T, Suematsu Y, Nakagiri M, Noguchi M, Tarbell T, Title A, Shine R, Rosenberg W, Hoffmann C, Jurcevich B, Kushner G, Levay M, Lites B, Elmore D, Matsushita T, Kawaguchi N, Saito H, Mikami I, Hill LD, Owens JK (2008a) The Solar Optical Telescope for the Hinode mission: An overview. Solar Phys 249:167–196

[192] Tsuneta S, Ichimoto K, Katsukawa Y, Lites BW, Matsuzaki K, Nagata S, Orozco Suárez D, Shimizu T, Shimojo M, Shine RA, Suematsu Y, Suzuki TK, Tarbell TD, Title AM (2008b) The magnetic landscape of the Sun's polar region. ApJ 688:1374–1381

[193] Tu C-Y, Marsch E, Wilhelm K, Curdt W (1998) Ion temperatures in a solar polar coronal hole observed by SUMER on SOHO. ApJ 503:475–482

[194] Tu C-Y, Zhou C, Marsch E, Xia L-D, Zhao L, Wang J-X, Wilhelm K (2005) Solar wind origin in coronal funnels. Science 308:519–523

[195] van de Hulst HC (1950a) The electron density of the solar corona. Bull Astron Inst Netherlands 11:135–150

[196] van de Hulst HC (1950b) On the polar rays of the corona. Bull Astron Inst Netherlands 11:150–159

[197] Velli M (1993) On the propagation of ideal, linear Alfvén waves in radially stratified stellar atmospheres and winds. A & A 270:304–314

[198] Velli M, Habbal SR, Esser R (1994) Coronal plumes and fine strucure in high speed solar wind streams. Space Sci Rev 70:391–396

[199] Verdini A, Velli M, Matthaeus WH, Oughton S, Dmitruk P (2010) A turbulence-driven model for heating and acceleration of the fast wind in coronal holes. ApJ 708:L116–L120

[200] Veselovsky IS, Panassenko OA (2000) Magnetic coupling between polar plumes and the heliospheric current. Adv Space Res 26:819–822

[201] von Steiger R, Fisk LA, Gloeckler G, Schwadron NA, Zurbuchen TH (1999) Composition variations in fast solar wind streams. AIP Conf Proc 471:143–146

[202] von Steiger R, Vial J-C, Bochsler P, Chaussidon M, Cohen CMS, Fleck B, Heber VS, Holweger H, Issautier K, Lazarus AJ, Ogilvie KW, Paquette JA, Reisenfeld DB, Teriaca L, Wilhelm K, Yusainee S, Laming JM, Wiens RC (2001) Measuring solar abundances. AIP Conf Proc 598:13–22

[203] Waldmeier M (1951) Die Sonnenkorona I. Birkhäuser, Basel

[204] Waldmeier M (1955) Die Minimumsstruktur der Sonnenkorona. Z Astrophys 37:233–260

[205] Waldmeier M (1957) Die Sonnenkorona II. Birkhäuser, Basel

[206] Wang Y-M (1994) Polar plumes and the solar wind. ApJ 435:L153–L156

[207] Wang Y-M (1996) Element separation by upward proton drag in the chromosphere. ApJ 464:L91–L94

[208] Wang Y-M (1998) Network activity and the evaporative formation of polar plumes. ApJ 501:L145–L150

[209] Wang Y-M (2009) Coronal holes and open magnetic flux. Space Sci Rev 144:383–399

[210] Wang Y-M, Sheeley NR Jr (1990) Solar wind speed and coronal flux-tube expansion. ApJ 355:726–732

[211] Wang Y-M, Sheeley NR Jr (1995) Coronal plumes and their relationship to network activity. ApJ 452:457–461

[212] Wang Y-M, Sheeley NR Jr (2004) Footpoint switching and the evolution of coronal holes. ApJ 612:1196–1205

[213] Wang Y-M, Muglach K (2008) Observations of low-latitude coronal plumes. Solar Phys 249:17–35

[214] Wang Y-M, Hawley SH, Sheeley NR Jr (1996) The magnetic nature of coronal holes. Science 271:464–469

[215] Wang Y-M, Sheeley NR Jr, Dere KP, Duffin RT, Howard RA, Michels DJ, Moses JD, Harvey JW, Branston DD, Delaboudinière J-P, Artzner GE, Hochedez JF, Defise JM, Catura RC, Lemen JR, Gurman JB, Neupert WM, Newmark J, Thompson B, Maucherat A, Clette F (1997) Association of Extreme-ultraviolet Imaging Telescope (EIT) polar plumes with mixed-polarity magnetic network. ApJ 484:L75–L78

[216] Wang Y-M, Sheeley NR Jr, Socker DG, Howard RA, Brueckner GE, Michels DJ, Moses D, St Cyr OC, Llebaria A, Delaboudinière J-P (1998) Observations of correlated white-light and extreme-ultraviolet jets from polar coronal holes. ApJ 508:899–907

[217] Wang Y-M, Sheeley NR Jr, Rich NB (2007a) Coronal pseudostreamers. ApJ 658:1340–1348

[218] Wang Y-M, Biersteker JB, Sheeley NR Jr, Koutchmy S, Mouette J, Druckmüller M (2007b) The solar eclipse of 2006 and the origin of raylike features in the white-light corona. ApJ 660:882–892

[219] Warren HP, Hassler DM (1999) The density structure of a solar polar coronal hole. J Geophys Res 104:9781–9789

[220] Widing KG, Feldman U (2001) On the rate of abundance modifications versus time in active region plasmas. ApJ 555:426–434

[221] Widing KG, Landi E, Feldman U (2005) Coronal element comparison observed by SOHO SUMER in the quiet southeast and northwest limb regions at 1.04 $R_\odot$ above the solar disk. ApJ 622:1211–1215

[222] Wiegelmann T, Solanki SK (2004) Similarities and differences between coronal holes and the quiet Sun: Are loop statistics the key? Solar Phys 225:227–247

[223] Wiegelmann T, Xia L-D, Marsch E (2005) Links between magnetic fields and plasma flows in a coronal hole. A & A 432:L1–L4

[224] Wilhelm K (1998) Results from the SUMER telescope and spectrometer on SOHO. Proc 3rd SOLTIP Symp, 1996, Beijing, pp 75–80

[225] Wilhelm K (2000) Solar spicules and macrospicules observed by SUMER. A & A 360:351–362

[226] Wilhelm K (2006) Solar coronal-hole plasma densities and temperatures. A & A 455:697–708

[227] Wilhelm K, Bodmer R (1998) Solar EUV and UV emission line observations above a polar coronal hole. Space Sci Rev 85:371–378

[228] Wilhelm K, Marsch E, Dwivedi BN, Hassler DM, Lemaire P, Gabriel AH, Huber MCE (1998) The solar corona above polar coronal holes as seen by SUMER on SOHO. ApJ 500:1023–1038

[229] Wilhelm K, Dammasch IE, Marsch E, Hassler DM (2000) On the source regions of the fast solar wind in polar coronal holes. A & A 353:749–756

[230] Wilhelm K, Dammasch IE, Xia L-D (2002a) Observations of ultraviolet emission lines in solar coronal holes on the disk with SUMER on SOHO. Adv Space Res 30:517–522

[231] Wilhelm K, Inhester B, Newmark JS (2002b) The inner solar corona seen by SUMER, LASCO/C1, and EIT: Electron densities and temperatures during the rise of the new solar cycle. A & A 382:328–341

[232] Wilhelm K, Dwivedi BN, Marsch E, Feldman U (2004) Observations of the Sun at vacuum-ultraviolet wavelengths from space. Part I: Concepts and instrumentation. Space Sci Rev 111:415–480

[233] Wilhelm K, Marsch E, Dwivedi BN, Feldman U (2007) Observations of the Sun at vacuum-ultraviolet wavelengths from space. Part II: Results and interpretations. Space Sci Rev 133:103–179

[234] Wilhelm K, Dwivedi BN, Curdt W (2010) Spectroscopic diagnostics of polar coronal plumes. In: Hasan SS, Rutten RJ (eds), Astrophys Space Sci Proc, pp 454–458, Springer, Berlin Heidelberg

[235] Woo R (2007) Filamentary structures of coronal white-light images. Solar Phys 241:251–261

[236] Woo R, Habbal SR (2000) Connecting the Sun and the solar wind: Source regions of the fast wind observed in interplanetary space. J Geophys Res 105:12 667–12 674

[237] Wuelser J-P, Lemen JR, Tarbell TD, Wolfson CJ, Cannon JC, Carpenter BA, Duncan DW, Gradwohl GS, Meyer SB, Moore AS, Navarro RL, Pearson JD, Rossi GR, Springer LA, Howard RA, Moses JD, Newmark JS, Delaboudinière J-P, Artzner GE, Auchère F, Bougnet M, Bouyries P, Bridou F, Clotaire J-Y, Colas G, Delmotte F, Jerome A, Lamare M, Mercier R, Mullot M, Ravet M-F, Song X, Bothmer V, Deutsch W (2004) EUVI: the STEREO-SECCHI extreme ultraviolet imager. SPIE Proc 5171:111–122

[238] Xia L-D, Marsch E, Curdt W (2003) On the outflow in an equatorial coronal hole. A & A 399:L5–L9

[239] Xia L-D, Marsch E, Wilhelm K (2004) On the network structures in solar equatorial coronal holes. Observations of SUMER and MDI on SOHO. A & A 424:1025–1037

[240] Yamauchi Y, Suess ST, Sakurai T (2002) Relation between pressure balance structures and polar plumes from Ulysses high latitude observations. Geophys Res Lett 29:21-1–4

[241] Yamauchi Y, Suess ST, Steinberg JT, Sakurai T (2004) Differential velocity between solar wind protons and alpha particles in pressure balance structures. J Geophys Res 109:A03104-1–10

[242] Young PR, Klimchuk JA, Mason HE (1999) Temperature and density in a polar plume — measurements from CDS/SOHO. A & A 350:286–301

[243] Zangrilli L, Poletto G, Nicolosi P, Noci G, Romoli M (2002) Two-dimensional structure of a polar coronal hole at solar minimum: New semiempirical methodology for deriving plasma parameters. ApJ 574:477–494

[244] Zangrilli L, Fineschi S, Massone G, Capobianco G, Porcu F, Calcidese P (2006) EKPol: Liquid crystal polarimeter for eclipse observations of the K-corona. Proc Int Symp SPSE 2006, Waw an Namos, 27–29 March 2006, pp. 37–45

[245] Zhang HL, Sampson DH, Fontes CJ (1990) Relativistic distorted-wave collision strengths and oscillator strengths for the 33 Cu-like ions with $60 \leq Z \leq 92$. Atomic Nucl Data Tab 44:31–77

[246] Zhao XP, Hoeksema JT, Scherrer PH (1999) Changes of the boot-shaped coronal hole boundary during Whole Sun Month near sunspot minimum. J Geophys Res 104:9735–9752

[247] Zhukov AN, Veselovsky IS, Koutchmy S, Llebaria A (2001) Helical magnetic structure of white light polar plumes. IAU Symp 203:434–436